UNIVERSITEIT VAN PRETORIA
UNIVERSITY OF PRETORIA
YUNIBESITHI YA PRETORIA

MODELLING AND CONTROL OF AN ARTICULATED UNDERGROUND MINING VEHICLE

by

Rolf Reimar Kohlmeyer

Submitted in partial fulfilment of the requirements for the degree

Master of Engineering (Electronic Engineering)

in the

Faculty of Engineering, the Built Environment and Information Technology

Department of Electrical, Electronic and Computer Engineering

UNIVERSITY OF PRETORIA

November 2011

UNIVERSITEIT VAN PRETORIA
UNIVERSITY OF PRETORIA
YUNIBESITHI YA PRETORIA

SUMMARY

MODELLING AND CONTROL OF AN ARTICULATED UNDERGROUND MINING VEHICLE

by

Rolf Reimar Kohlmeyer

Supervisor:	Prof. I.K. Craig
Co-Supervisor:	Dr F.R. Camisani-Calzolari
Department:	Electrical, Electronic and Computer Engineering University of Pretoria
Degree:	Master of Engineering (Electronic Engineering)

Keywords: Underground mining, automation, articulated vehicles, localization, control, kinematic modelling, dynamic modelling, navigation, load-haul-dump truck.

The automation of the tramming or load, haul and dump (LHD) procedure, performed by a LHD vehicle, holds the potential to improve productivity, efficiency and safety in the mining environment. Productivity is mainly increased by longer working hours; efficiency is improved by repetitive, faultless and predictable work; and safety is improved by removing the human operator from the harsh environment. However, before the automation of the process can be addressed, a thorough understanding of the process and its duty in the overall mining method is required. Therefore, the current applicable mining methods and their areas of potential automation are given. Since the automation of the LHD vehicle is at the core of this project, its implementation in the tramming process is also justified. Also, the current underground navigation methods are given and their shortcomings are named. It is concluded that infrastructure-free navigation is the only viable solution in the ever-changing mining environment. With that in mind, the feasibility of various navigation sensors is discussed and conclusions are drawn.

Both kinematic and dynamic modelling of LHD vehicles are introduced. Various forms of kinematic models are given and their underlying modelling assumptions are named. The most prominent assumptions concern the vehicle's half-length and the inclusion of a wheel-slip factor. Dynamic modelling techniques, with a strong emphasis on tyre modelling, are also stated. In order to evaluate the modelling techniques, field tests are performed on the articulated vehicles, namely the Wright 365 LHD and the Bell 1706C loader. The test on the Wright 365 LHD gives a good impression of the harsh ergonomics under which the operator has to work. A more thorough test is performed on the Bell 1706C articulated loader. The test results are then compared to simulation results obtained from the kinematic models. Also, the above-named assumptions are tested, evaluated and discussed. A dynamic model is also simulated and discussed. Lastly, two localization and control methods are given and evaluated. The first method is an open-loop nonlinear optimal control strategy with periodic position resetting and the second method is a path-tracking controller.

UNIVERSITEIT VAN PRETORIA
UNIVERSITY OF PRETORIA
YUNIBESITHI YA PRETORIA

OPSOMMING

MODELLERING EN BEHEER VAN ’n GEKOPPELDE ONDERGRONDSE MYNVOERTUIG

deur

Rolf Reimar Kohlmeyer

Studieleier:	Prof. I.K. Craig
Mede-studieleier:	Dr. F.R. Camisani-Calzolari
Departement:	Elektriese, Elektroniese en Rekenaaringenieurswese
	Universiteit van Pretoria
Graad:	Magister (Elektroniese Ingenieurswese)

Sleutelwoorde: Ondergrondse mynbou, automatisasie, gekoppelde voertuie, lokalisering, beheer, kinematiese modellering, dinamiese modellering, navigasie, LVD.

Automatisering van die laai-, vervoer- en dompel- (LVD) prosedure het die potensiaal om die produktiwiteit, effektiwiteit en veiligheid van die mynbedryf te verbeter. Produktiwiteit word hoofsaaklik deur langer werksure verhoog, effektiwiteit word deur herhalende, foutlose en voorspelbare werk verbeter en veiligheid word verbeter omdat menslike operateurs uit die gevaarlike ondergrondse omgewing verwyder word. Voordat aandag aan die automatisering van die prosedure geskenk kan word, moet die prosedure en die algemene mynbedrywighede rakende die prosedure deeglik bestudeer en verstaan word. As gevolg hiervan word die huidige, toepaslike mynboumetodes hier gedokumenteer. Die implementering van ’n gekoppelde LVD-voertuig in die LVD-prosesword ook geregverdig. Verder word die huidige metodes van ondergrondse navigasie genoem en hulle tekortkominge aangedui. Die gevolgtrekking dat infrastruktuur-vrye navigasie die enigste lewensvatbare navigasiemetode in die immer veranderende ondergrondsemynbou-omgewing is, word ook gemaak. In die lig daarvan word ’n verskeidenheid sensors genoem en bespreek.

Kinematiese en dinamiese modellering van ŉ LVD-voertuig word bekendgestel. Verskeie kinematiese modelle en hulle onderliggende aannames word genoem. Die mees prominente aannames is die lengte van die gekoppelde voertuig se hoofdele en die insluiting van ŉ wielglipfaktor. Die tegnieke van dinamiese modellering, met die klem op bandmodellering, word ook gegee. Praktyktoetse op gekoppelde voertuie is ook gedoen om die verskillende modelle te evalueer. Die toets op die Wright 365-LVD bied goeie insig in die strawwe ergonomiese toestande waaronder die operateurs moet werk. ŉ Deeglike toets is op ŉ BELL 1706C- gekoppelde laaier, wat kinematies identies aan ŉ LVD-voertuig is, uitgevoer. Die bevindinge van die toets word met bogenoemde modelsimulasies vergelyk en gevolgtrekkings word gemaak. Laastens word lokalisiering en beheer van ŉ LVD-voertuig behandel. Twee beheermetodes, opelus- nie-lineêre optimale beheer met periodieke herstel en padvolgingbeheer word geëvalueer en bespreek.

TABLE OF CONTENT

CHAPTER 1

INTRODUCTION

1.1 MOTIVATION

The mining industry is under constant pressure to improve productivity, efficiency and safety. The automation of repetitive mining procedures holds the potential to address all these issues. A prime example of such a repetitive procedure is the tramming routine. According to [1], the tramming procedure refers to a 'load-haul-dump' (LHD) process, which is performed by a LHD truck, where fragmented rock is excavated, hauled to an assigned location and then dumped at a transport drift. The LHD vehicles are usually centre articulated, meaning that the vehicle is steered by applying a torque at the hinge that connects the front and rear of the vehicle. This vehicle is traditionally handled manually by an operator, who is therefore constantly exposed to the harsh underground environment. The hazardous nature of underground mining environments, driver safety and fatigue, labour costs, and the cyclic nature of this task are all obvious motivations to automate the tramming process.

The benefits of this automation are mentioned here:

- Improved safety for mine workers.

  Tele-operation or full automation of the tramming process can remove the operator from a hazardous environment. For mining operations in underground uranium, coal and asbestos mines, where radioactivity, toxic gas and fibre dust respectively are health concerns for miners, automation can be an ideal solution.
- Increased utility of personnel.

  Once a fleet of LHD vehicles have been automated, only one operator is required to handle a number of vehicles. Also, comparatively, it allows the operator to work productively for longer shifts.
- Reduced maintenance costs.

  Maintenance costs are reduced due to the predictable and controlled operation of the vehicle which eliminates any unruly or abusive driving by a human operator.

The operating lifetime of mechanical vehicle parts is therefore more predictable and implementing a preventative maintenance routine is possible.

- Increased productivity.
  The utility of the LHD and in effect the overall productivity is improved due to the decrease in unscheduled delays caused by human error and untimely shift changes.

However, automation also has its drawbacks, which include:

- Difficulties in economic justification.
  It is not easy to place economic value on safety, productivity, utilization and maintenance of equipment.
- Increase in complexity.
  Introducing an automation system complicates the mining process and a specialised workforce is required to operate and maintain this system.
- Acceptance of automation by unions and/or workers.
  Workers may not comprehend the benefits of the new automation technology and may feel threatened to be ostracized by its implementation.

1.2 BACKGROUND

For over 20 years the automation of LHDs has been studied [2]. In order to achieve successful autonomous navigation, four main tasks have to be performed by the LHD: Sensing its immediate environment, building and interpreting its own representation of the environment, locating itself within its environment and lastly planning and executing efficient routes in this environment [2]. Although some successful infrastructure-guided navigation systems, for example [3], [4] and [5], have been developed, the installation, maintenance and the overall cost of such systems are not favourable in the ever-changing mining environment. Therefore, recent research has focused on developing infrastructure-free navigation systems, as in [6], [7] and [8]. Due to the harsh underground mining environment, only a few infrastructure-free positioning and localization sensors can be considered, making accurate environment sensing a difficult task [9]; the Global Positioning System (GPS), most notably, does not have satellite reception in the underground environment and can hence not be implemented. This hindrance implies that

the predictive vehicle model needs to be accurate in order to compensate for the relatively imprecise available sensor systems [10]. Both kinematic ([11], [12], [7] and [13]) and dynamic ([14], [15] and [16]) LHD vehicle models have been developed with varying success.

1.3 CONTRIBUTION

As has been mentioned above, the accuracy of the LHD vehicle model is vital in the process of localization and navigation in an underground mining environment. [17] states that due to LHD's typical slow speed, study of the kinematics of motion is sufficient for navigation purposes and design of motion controllers, hence ignoring the involved dynamic forces. Kinematic models further assume that no motion parallel to the axles is present (no-slip condition), movement on a horizontal plane and often depict the LHD dual-unit with perfect half-length units meeting at the articulation joint. These assumptions are not always viable and are seldom substantiated and validated and should be further investigated.

The dynamic models, specifically those developed by [14] and [15] attempt to include all the relevant forces but fail to validate their findings. [14] does not include the effects of slip while [15] attempts to do so by including a 'tyre model'. A real-time on-line dynamic model has as yet not been successfully developed due to the high computational requirements, questioning the viability of a dynamic LHD model for autonomous navigation purposes. Also, accurate localization and control of the automated vehicle is of importance. Since infrastructure-free navigation is the most viable option, localization and control systems build around this underlying requirement will need to be developed and evaluated.

The proposed research output should act as a stepping stone for future development of LHD vehicle models and resulting in more accurate and efficient navigation.

1.4 DISSERTATION APPROACH

The following research approach was taken in fulfilling the objectives of the proposed research:

- A literature study was completed on the following topics in order to gain insight into the involved matter:
  - Current underground mining techniques especially in areas where automation is plausible.
  - The LHD vehicle, why and how automation is advantageous.
  - Current advances in mine automation specifically those involving the LHD.
  - Vehicle modelling concentrating on both kinematic modelling and dynamic modelling of articulated vehicles.
  - Localization and control in the underground environment.
- The existing models of the LHD vehicle were discussed and possible short-comings were found.
- Practical field tests on both a LHD and an articulated loader were performed to gather data. The data was used for various offline tests and simulations.
- Simulations of the involved models were done and, where applicable, were compared to the field test data. The simulation results were then evaluated and discussed.
- Localization and control methods were developed and evaluated.

1.5 DISSERTATION OVERVIEW

The rest of this dissertation is organized as follows: Chapter 2 gives a general overview of the mining industry, especially underground mining. Also, the LHD vehicle is introduced. In Chapter 3, the various navigation methods for the underground mining environment are mentioned and discussed. Also, the applicable sensor suits are mentioned and evaluated. Chapter 4 covers the current articulated vehicle modelling techniques, dealing with both kinematic and dynamic modelling. In Chapter 5 the results of the practical field tests on the articulated vehicles are given. Then, the simulations for the evaluation of the vehicle models are compared to the practical results. Chapter 6 implements a kinematic vehicle model in localization and control methods. Lastly, Chapter 7 draws conclusions on the obtained results and mentions opportunities for future work.

CHAPTER 2

MINING OVERVIEW

A general background of the modern mining industry is given in this chapter. Firstly, the current trackless underground mining methods are introduced where the purpose of the Load-Haul-Dump (LHD) vehicle is made clear. Next, the LHD vehicle is introduced and its application in the underground mining process is motivated. Lastly, the automation of the mining process is motivated and its advantages are mentioned.

2.1 UNDERGROUND MINING METHOD

Various mining methods have been developed to suit the specific type of ore body; these methods include [18]:

- room and pillar,
- cut and fill stoping,
- block caving,
- sublevel stoping and
- sublevel caving.

However, the LHD predominantly features in the two mining methods which make use of trackless equipment, namely the block caving and the sublevel caving methods.

Block caving, with reference to Figure 1, essentially consists of a main underground haulage level which leads to the draw point, through transfer raises. Above the draw point, the overlying rock, broken by gravity and blasting, flows through funnel-shaped tunnels toward the grizzly level. Here the ore is hauled, by means of a LHD, toward the haulage level where it is taken away for processing.

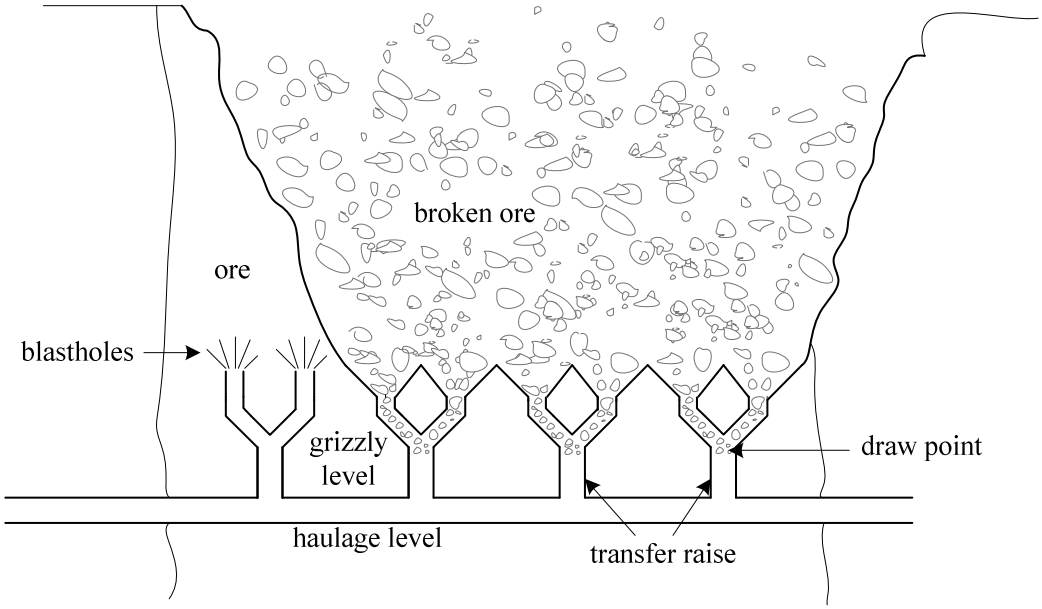

Figure 1. An illustration of the block caving method.

Figure 2 illustrates the steps involved in the sublevel caving mining method. In the first step, horizontal tunnels are drilled into the ore body. Then, in step 2 (production drilling), holes are drilled upwards into the ore body. The holes are then charged with explosives, as depicted in step 3. In step 4, a LHD loads the blasted ore and hauls it to the main haulage level (step 5). Lastly, in step 6, the ore is hoisted away for further processing.

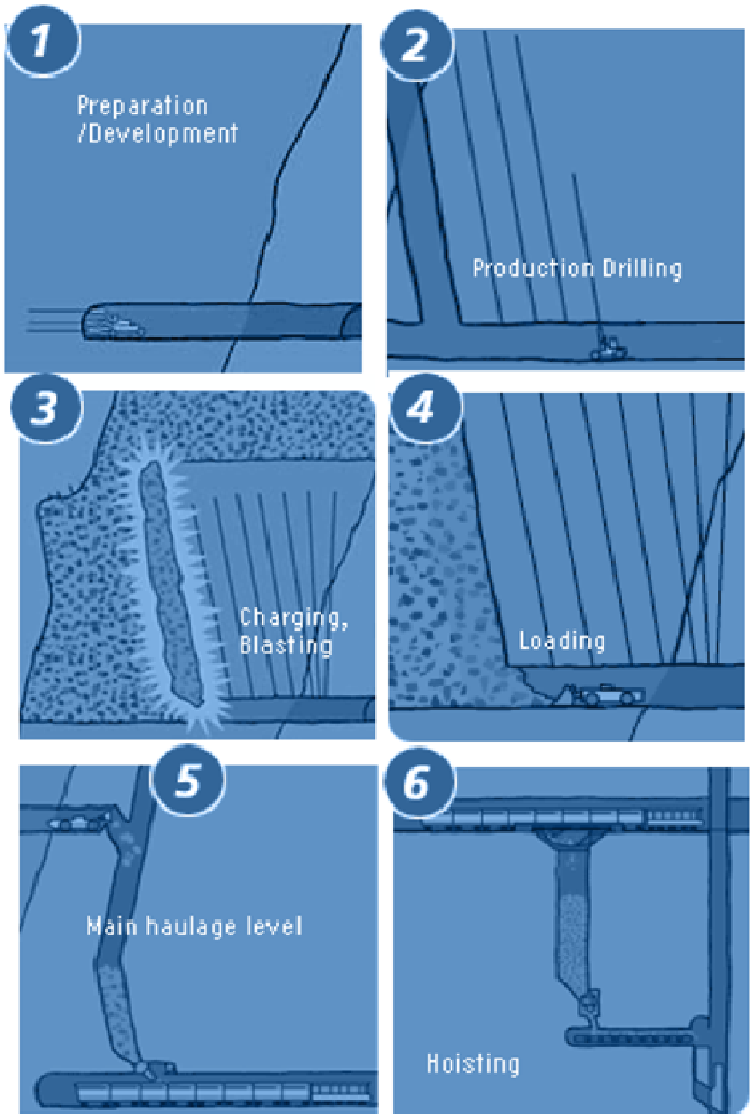

Figure 2. A step-wise indication of the sublevel caving mining method, from [19].

2.2 LOAD-HAUL-DUMP VEHICLE

By the mid-1960, load-haul-dump (LHD) vehicles were firmly established as a fundamental part of what has become known as the “trackless” mining concept, used in many mines and many countries around the world today. The mobility, flexibility, and versatility of these units have given the industry a useful tool and have added new dimensions to mine development and production.

They are four-wheeled vehicles consisting of two bodies interconnected by an articulation joint. Figure 3, taken from [20], is a drawing of a Wright 356 LHD vehicle with its

dimensions. This specific LHD is commonly used in South African underground mines. Steering is achieved by controlling the hydraulically driven hitch joint angle.

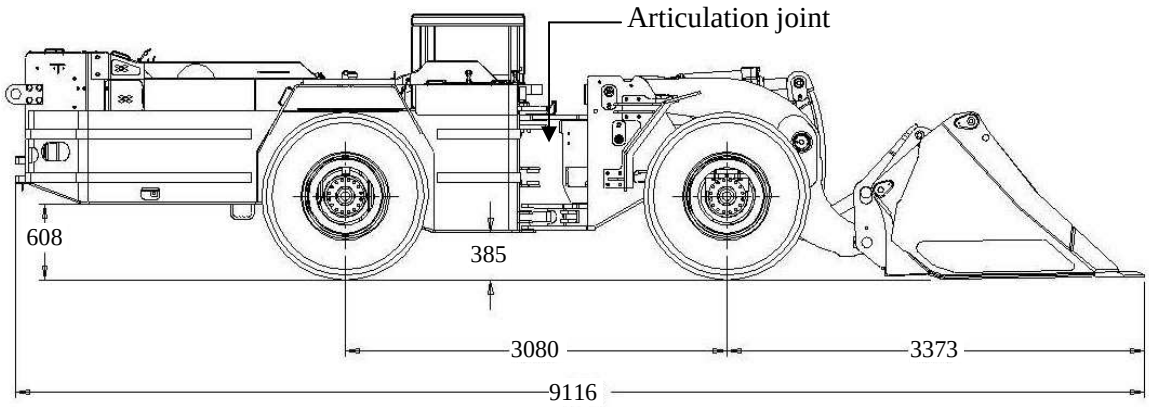

Figure 3. The dimensions (in mm) and the articulation joint of the Wright 356 LHD.

A picture of the articulation joint of the Wright LHD is shown in Figure 4.

Figure 4. The articulation joint of a Wright 356B LHD.

LHD vehicles combine certain characteristics of conventional front-end loaders and dump trucks, specifically designed for materials handling in underground mining and tunnelling. A typical production cycle of a LHD unit has the operator driving the vehicle forward, forcing the bucket into the muck at or near floor level, and using the tractive effort of the vehicle and the prying action of the bucket to roll out and tilt back the load. With the bucket rolled back into the carrying position on the boom and the boom resting on the main frame of the vehicle, the load is hauled (trammed) to the dump point, as is shown in Figure 5. At the dump point, the boom is returned to rest on the main frame, and the unit is driven back to the loading point for another load. Operation is cyclic with typically 14-18 trips per hour and round trip distances from 100 m to 600 m.

Figure 5. A LHD vehicle is shown during hauling [Anon].

The vehicle's manoeuvrability, which is one of the benefits of an articulated vehicle, is improved by the steering mechanism. The vehicle can alter its orientation by changing the steering angle alone and the width spanned by the vehicle while turning is lessened when compared to a car-like vehicle. Figure 6, taken from [20], shows the turning dimensions of a Wright 356 LHD during a minimum-radius turning manoeuvre.

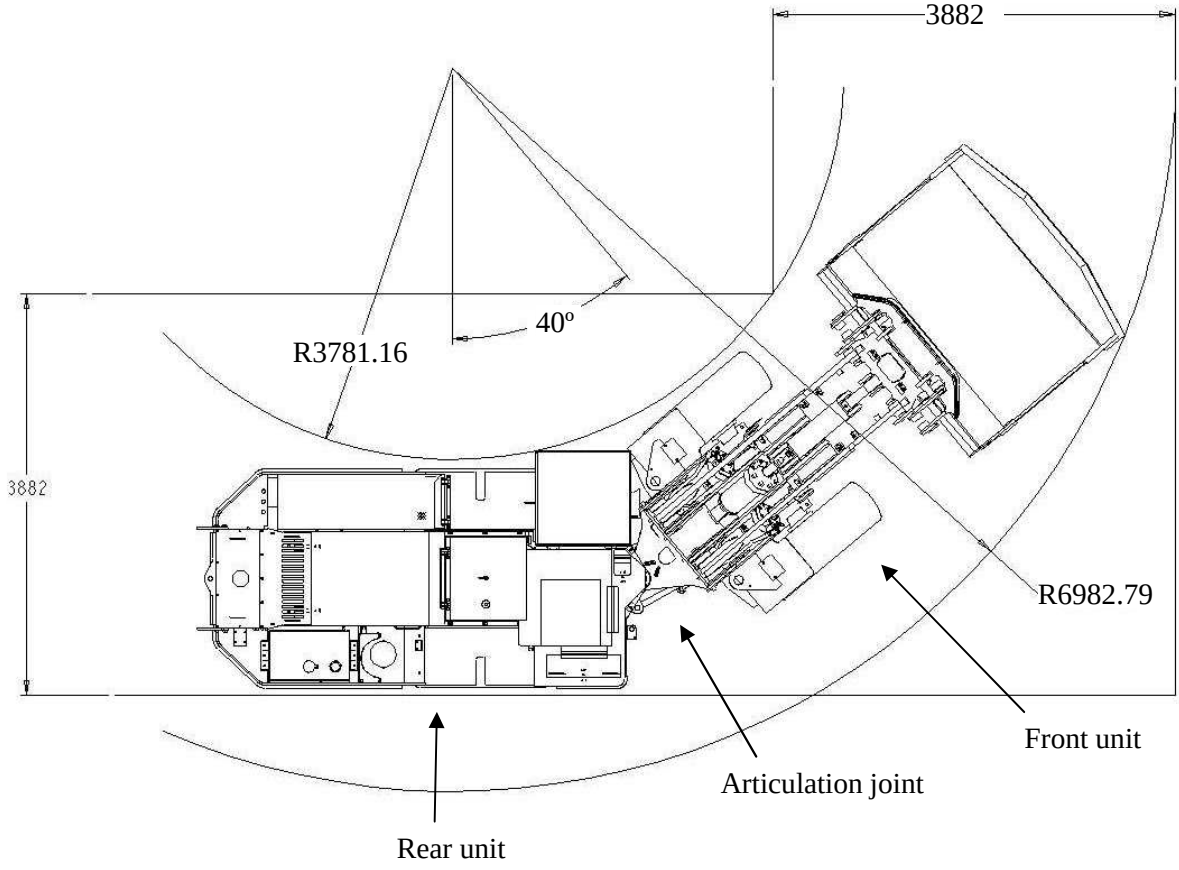

Figure 6. Turning manoeuvre of a Wright 356 LHD vehicle.

A multi-axle vehicle's manoeuvrability can be measured by the difference of the trajectories followed by the midpoints of their axles. The smaller the difference, the more manoeuvrable the vehicle is [21]. Figure 7 clearly indicates the difference in manoeuvrability between a car-like vehicle and an articulated vehicle.

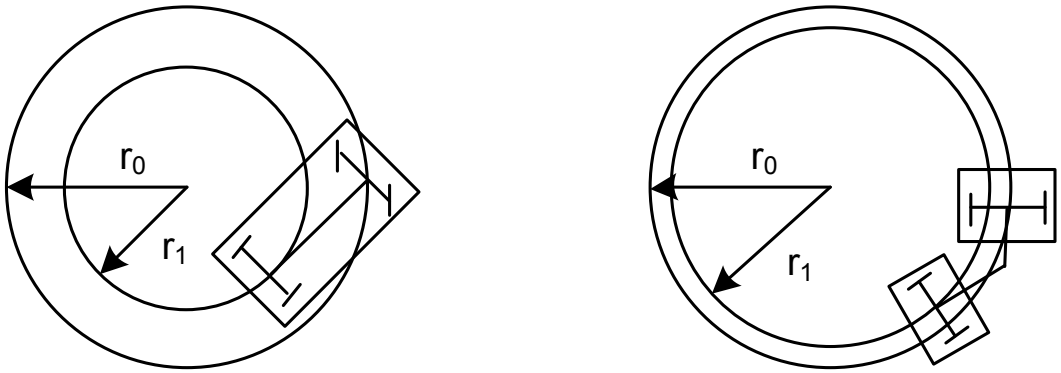

a) **b)**

Figure 7. This figure shows the comparison of off-tracking error of a car-like vehicle (a) and an articulated vehicle (b), adapted from [21].

The off-tracking error for a car-like vehicle is given by

$$r_0 - r_1 = L\frac{1-\cos\beta}{\sin\beta}, \tag{2.1}$$

where L is the length of the car-like vehicle and β is the steering angle of the front tyres.

For an articulated vehicle, the steady-state turning dimensions are shown in Figure 8.

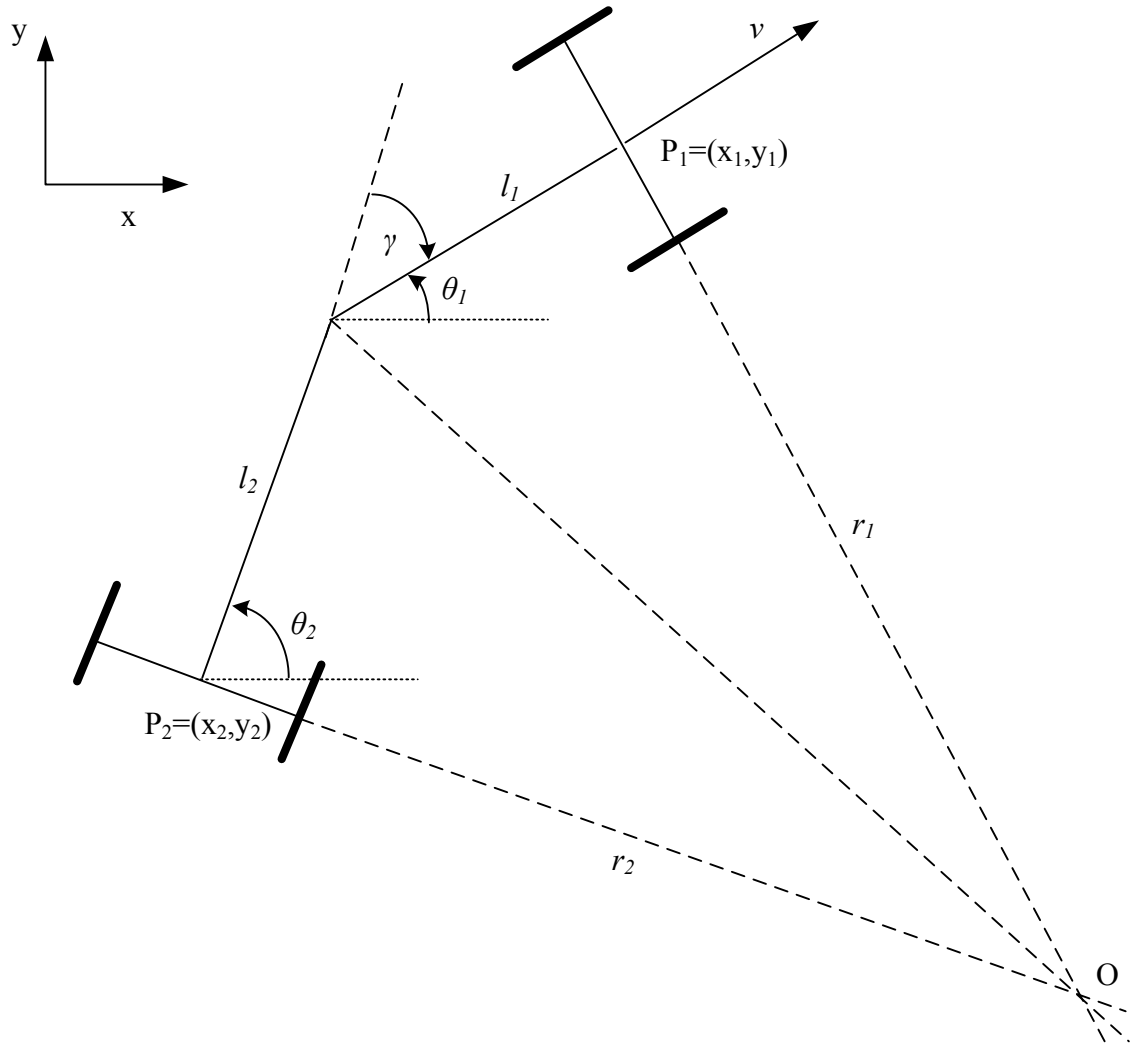

Figure 8. The steady-state turning dimensions of an articulated vehicle are shown.

The turning radius of the front unit is given by

$$r_0 = \frac{l_1 \cos\gamma + l_2}{\sin\gamma}, \tag{2.2}$$

whereas the turning radius of the rear unit is given by

$$r_1 = \frac{l_2 \cos\gamma + l_1}{\sin\gamma}, \tag{2.3}$$

where l_1 and l_2 are the lengths of the front and the rear units from the articulation joint to the centre of the axle, respectively. The articulation angle is given by γ. Hence, the off-tracking error is given by

$$r_0 - r_1 = \frac{(l_1 - l_2)\cos\gamma + (l_2 - l_1)}{\sin\gamma}. \tag{2.4}$$

The off-tracking error of an articulated vehicle is zero if $l_1 = l_2$. LHDs are therefore often designed with similar-sized front and rear units (refer to Figure 3). Having a negligible off-tracking error simplifies the path-tracking problem [21].

2.3 IMPROVEMENTS TO BE MADE BY AUTOMATION

2.3.1 Utilization

[22] estimates that the utilization of an LHD vehicle at a typical underground mine is only about 50%. The main reasons are given as follows (in order of significance):

- Tip availability,
- unscheduled delays and
- scheduled delays.

The tip availability refers to the availability of the ore pass or the transport drift. An optimized vehicle dispatch system, [23], may be implemented to improve the transport of the muck from the ore passes in order to increase their availability.

Unscheduled delays are mainly caused by the human driver's inefficiency and inability. The driver may take longer than planned to return to work after a scheduled tea or lunch break or may stop work prior to the end of a shift. Dust, on average, accounts for about 15 minutes of delay on a 9 hour shift [22]. Dust is caused by falling muck at the draw point or the ore pass and by the mobile mining vehicles travelling on the gravel surface. Reduced visibility and air breathability force the LHD driver to wait until the dust has settled.

Lastly, scheduled delays include rest periods for the drivers and planned maintenance on the LHD vehicles.

2.3.2 Safety

The underground mining environment is a harsh environment induced by high noise levels, polluted air, limited visibility and large mobile mining vehicles. Human safety, therefore, is always a concern in this unforgiving environment. The South African government's Minerals and Energy Department [24] sections the health and safety issues in the mining sector as follows:

- Accidents,
- Silicosis and
- noise-induced hearing loss.

2.3.2.1 Accidents

Accidents include falls of ground (rock) on workers, workers falling into gauges or deep excavations and machinery and transporting accidents. The classifications of accidents and accident area in South African underground mines are given in Table 1.

Table 1. The percentage classifications of accidents and accident area [24].

Accident area	Percentage (%)
Conveyor belts	15.7
Ore transport Tractor/Trailers	14.5
LHDs	10.3
Trucks	9.5
Shuttle cars at transport drift	9.1
Continuous miners	9.4

At 10.3% of all underground mining accidents, the LHDs account for about 20 deaths per year in South Africa alone. [24] allocated the LHD accidents into further categories, stating the cause of the accident. Table 2 shows the allocation of cause of the accident in the LHD category in the underground mining industry in South Africa.

Table 2. Percentage allocation of cause of accident in the LHD category. Adapted from [24].

Category	Percentage (%)
Failure to comply with standards	48.2
Lack of caution/alertness	16.1
Inadequate examination/inspection test	8.9
Failure to comply with instructions	1.8
Failure to comply with protective devices	1.8
Lack of suitable system/facilities	3.6
Lack of standards or procedures	1.8
Lack of illumination/visibility	5.4
Inadequate supervision	1.8
Use of unsuitable facilities	3.6
Lack of clearance (obstruction)	7.1
Lack of suitable training	0
Inadequate preventative maintenance	0

The dominant cause is identified as a failure to comply with good practice, standards and procedures. Also, the lack of driver caution and alertness accounts for a substantial number of accidents. Few accidents can be put down to machine failure [24]. An obvious conclusion, therefore, is that human error accounts for almost all of the accidents involving LHDs in the underground mining environment.

2.3.2.2 Silicosis

Next, bad air accounts for a high number of fatalities in underground mining. Silicosis is a lung disease caused by breathing silica quartz dust prevalent in gold mines. At least 18,000 South Africans have died from silicosis between 1997 and 2007, according to the South African Chamber of Commerce and Industry's 2007 Sustainability and Transformation Report, [25]. Furthermore, there is a link between workers contracting silicosis and tuberculosis, a disease to which those suffering HIV/Aids are susceptible. TB rates remain high in the South African mining sector despite the industry's best efforts to prevent this.

The rate runs as high as 4,200/100,000 workers/year, with the overwhelming majority of those in the gold sector. Limiting human exposure to silica quartz dust by automating the highly infected areas will by default reduce the number of Silicosis cases.

2.3.2.3 Noise Induced Hearing Loss

Noise induced hearing loss is also a serious concern for the underground mine workers. [26] estimates that 80% of United States miners go to work in an environment where the time-weighted average (TWA) noise power exceeds 85 dB and that 25% of these are exposed to a TWA noise level that exceeds 90 dB. Table 3 indicates the estimated noise exposure in different mining areas. According to United States law, the employer must provide hearing protection devices at a sound level of more than 80 dB. When the sound level is higher than 85 dB employees are indeed obliged to use these hearing protection devices. These places are to be clearly demarcated and marked. However, negligence and misuse of the protective devices can lead to permanent hearing loss.

Table 3. Estimates of noise exposure from plant and equipment.

Noise source	Range (dB)	Mid point (dB)
Pneumatic percussion tools	114-120	117
Continuous miners	97–103	100
Loader-dumper	97–102	100
Fans	90-110	100
Long-wall shearers	96-101	99
Chain conveyors	97–100	99
Loaders	95–100	98
Haulage truck	90–100	95
Locomotives (electrical)	85–95	90
Cutting machines	83–93	88

2.4 CHAPTER SUMMARY

This chapter served as an overview of the current mining methods and motivates the automation of some of the processes involved in these methods. Notably, the automation of the tramming process, performed with the LHD vehicle, is a key area in which the harsh working environment can be improved. Both productivity and safety can be improved by the automation of this repetitive hauling action. As an example, the partially automated Finsch mine is mentioned and its productivity and safety record speak for themselves.

CHAPTER 3

NAVIGATION IN AN UNDERGROUND MINING ENVIRONMENT

After two decades of research activity, reliable navigation in an underground mining environment still remains a challenging task. This challenge is due to the complexity of the partially known and unstructured environment. Pathway intersections, wall irregularities, ground unevenness, dust, humidity, water splashing, vibration and obstacles; the difficulties in communication due to limited bandwidth and delay; the absence of precise positions systems (such as the GPS) for absolute localization; and the stringent requirements on the information accuracy on the vehicle's heading and lateral positioning are the main difficulties faced by researchers [2], [6], [7], [11].

3.1 ABSOLUTE NAVIGATION

[13] states that absolute navigation refers to a navigation system where the position of a vehicle is always known with respect to a real-world fixed coordinate system. Within this coordinate system, the vehicle is controlled to follow a certain path as accurately as possible. [12] and [7] provide examples of path following control for a LHD. Onboard sensors are fused to give the approximate absolute position of the vehicle. Sensors include inertial measurement unit (IMU), odometry and heading data (see section 3.6). The estimated absolute position, however, needs to be updated (corrected) periodically by external sensor information. The information could be obtained from artificial beacons or from natural features in the environment. The sensor data is then most commonly fused using a Kalman filter [12]. The elemental flaw of absolute navigation is that the vehicle is unaware of its immediate surroundings; it relies on the fact that its absolute position and its pre-determined path are accurately known. Three types of map representation are common in literature: metric, topological and hybrid maps.

3.1.1 Metric maps

This approach builds a geometrical representation of the environment using a detailed metrical description of its surroundings from sensor data [1]. Although the relation to the real world is well defined, this method is vulnerable to inaccurate metrical devices and actuator movement. Generally, the approach is to represent the environment with a grid of a sufficiently high and fixed resolution. Each grid contains metric information of its real world counterpart and sensory data are used to determine the occupancy value, either ‘occupied’ or ‘not occupied’, of each grid cell. The vehicle’s position and orientation within its model can be determined by its position and orientation in the real world.

However, any approaches using purely metric maps are vulnerable to inaccuracies in both map-making and dead-reckoning abilities of the vehicle. Even by taking into account all relationships between features and the vehicle itself, in large environments the drift in the odometry causes difficulties for map maintenance and makes the global consistency of the map difficult to maintain. Landmark-based approaches, which rely on the topology of the environment, can better handle this problem, because they only have to maintain topological global consistency, not the metric one.

3.1.2 Topological maps

A topological map is a feature-based map that uses symbolic description to build a map to represent its environment [27], [28]. Whereas metric maps rely on quantitative information, topological maps rely on qualitative data and are less sensitive to sensor errors, less complex and permits more efficient planning. Relative positions between landmarks rather than distances are considered and used for path navigation.

An important aspect of an efficient topological map, therefore, is the presence of unambiguous and recognizable landmarks. Since sensory input depends strongly on the viewpoint of the robot, topological approaches may fail to recognize geometrically nearby places. The resolution of topological maps corresponds directly to the complexity of the environment and a fundamental problem in topological mapping is recognizing an already-visited place, i.e., closing the loop.

On the other hand, topological approaches usually do not require the exact determination of the geometric position of the robot, they often recover better from drift and slippage that must constantly be monitored and compensated in grid-based approaches.

3.1.3 Hybrid maps

This approach attempts to combine the advantages of both the metric and topological methods by embodying both representations [29]. In a hybrid map, the environment is described by a global topological map, so that it facilitates planning and re-planning within the whole environment to enable the vehicle finding a suitable route to its currently stated target; on the contrary, local metric maps can be used by the vehicle for safe navigation toward a given target, and the robot needs further localization precision.

3.2 REACTIVE NAVIGATION

In contrast to absolute navigation, reactive navigation allows the vehicle to sense its immediate surroundings and hence react in relation to these surroundings, as stated by [13]. The vehicle does not know where it is in terms of a global coordinate system; it only knows its position relative to local objects or navigation infrastructure by which it is guided. Examples of reactive navigation implementation in the underground mining environment are [3] and [30] where researchers evolve the simple line-following technique into a navigation system where a LHD follows a line of retro-reflective strips or lines of light. Following a line, however, restricts the vehicle's look-ahead and hence limits the speed at which the vehicle can travel. One solution to improve the look-ahead is to sense the walls in front of the vehicle, allowing the vehicle to predict the distance it can travel at high speed before any evasive manoeuvre has to be performed. Apart from line-following, wall following is a popular method of navigation in the mining environment. Sensors include ultrasonic sensors, laser rangers and radar. As has been mentioned, the major flaw of reactive navigation is the lack of look-ahead and the inability to place the vehicle's position within a global framework.

3.3 INFRASTRUCTURE-GUIDED NAVIGATION SYSTEMS

Some of the automating and localization methods developed by previous research involving the usage of infrastructure will briefly be stated in this section. Most of the research stated focuses on a highly structured indoor environment which is not always applicable to the unstructured and harsh environment posed by an underground mine.

[5], [4], [30], and [8] present optical guidance systems which were all trialled and abandoned mainly due to their operational costs, inconsistencies and infeasibility. Following an overhead optical guide, following a painted line on the back of the tunnel, keeping track of retro-reflective tape and following a line of lights along the mine tunnels are some of the failed attempts of optical guidance systems.

An accurate mechanical pantograph guidance system was successfully developed by [9]. As is commonly implemented in a railway system, the pantograph collects the electric current from overhead lines, powering the electrical vehicle. Information on its position and heading was obtained by the sensors attached to the pantograph. However, the high cost of the installation and maintenance of the system ($1500 per meter) deemed it infeasible.

The first method used in real production was an inductive wire-guided system, by [5]. This system was tested at the Kiruna mine in Sweden. Although this is a straightforward method, wire-guidance proved to be too inflexible since the routes may vary quite often. Furthermore, the technique limited the driving speed of the automated vehicle as compared to manual operation.

Using the roof instead of the floor of a tunnel to install artificial beacons decreases the amount of work, as illustrated by [31]. A light emitting rope on the tunnel roof is detected by cameras to guide the vehicle. Corresponding systems have been built using a retro reflective stripe on the roof.

Another system successfully tested at the Kiruna mine solved the speed limitation of the automated mining vehicles when compared to manual operated vehicles. Using the

manually installed guidance infrastructure to monitor the current transversal position error of the automated vehicle to correct the steering relative to this error leads easily to dynamic problems when driving at high speeds. This is due to the significant delay in the steering system of the LHD. [32] developed a system which has a priori knowledge of the route to be undertaken by the vehicle. The position controller was designed as predictive, enabling driving at full speed. The navigation system is based on a rotating laser positioning system and retro reflective tape on the walls.

3.4 INFRASTRUCTURE-FREE NAVIGATIONS METHODS

The high cost and the difficulty of maintaining infrastructures make infrastructure-guided navigation systems impractical for changing environments. These limitations motivate research on guideless navigation systems for underground mines. The most challenging aspect of infrastructure-free guidance is the design and implementation of a sensor system which accurately senses and recognises the immediate surroundings of the underground environment.

3.4.1 Path-learning

One of the leading autonomous tramming systems is based on the path-learning method [2]. The vehicle is taught a specific route along which it can autonomously drive at full speed. The navigation system is based on the fusion of dead reckoning and position measurement using the natural features of the walls of the tunnels. Dead reckoning is the procedure of estimating the vehicle’s current position based upon a previously know position. A subsequent position is then cumulatively calculated from vehicle speed and course measurement. All the navigation equipment is on board the LHD; no external infrastructure is required in the tunnel for navigation purposes.

The following sensors are implemented on the LHD:

- articulation angle sensor,
- odometer,
- gyroscope and

- two laser scanners.

The odometer, the articulation angle sensor and the gyro are used for obtaining the position and heading by implementing the dead reckoning technique. Because the dead reckoning technique calculates the new position only from previous position estimates, errors will accumulate. Therefore, two laser scanners are installed on board to compensate for the drift of the dead reckoning process.

Several methods exist for teaching the automated vehicle a predefined path. One could use basic path elements, such as a straight line, arc with constant turning radius, clothoid, etc. to construct a more complicated pathway. The vehicle can operate at optimal speed since any change in pose is predictive allowing any mechanical adjustments, to steering or acceleration, to be optimally timed. However, this method does not take the local conditions of the path into account. Influential conditions include rough surfaces and limited space in the tunnel.

A straightforward method is to define a new path by manually driving the vehicle along the specified route. An experienced driver may manually drive along the route while being on-board the vehicle or on a remote location via a tele-operated system. During the teaching, the navigation system records the driver input as well as its immediate surroundings. The biggest drawback of this procedure is that any change in this dynamic mining environment would require the vehicle to undergo another time-consuming round of teaching.

3.4.2 Wall-following

3.4.2.1 Potential field methods

The general principle behind the potential field method is to treat the vehicle as a particle that is attracted by a potential field radiating from its goal [33]. Similarly, the particle is repulsed by potential fields emitted by obstacles. In determining the next course of action, a sum of the potential fields is determined at its current position and hence the most promising direction is obtained. Real-time implementation of such a scheme is feasible since it is iterative in nature. However, in determining its next promising direction, it may

be caught in a local minima and hence be unable to reach its goal. An example of a potential field navigated robot can be found in [34]. Here, an automatic guided vehicle (AGV) was developed that used a potential field method to move around in a structured indoor environment. A scanning laser was implemented to detect walls aiding the robot to perform wall-following. [35] described a local path planner based on the potential field method similar in principle to the active contour methods commonly used in image processing and computer vision applications. The local path was created by applying the summed potential field to a straight line segment that began at the vehicle and pointed in the direction of the goal.

3.4.2.2 Neural network methods

Neural networks can also be applied to the wall-following problem. Its feasibility to real-time application is strongly supported by its speedy execution cycle. [36] presents a method in which a vehicle was taught to steer using a neural network. The vehicle could steer through previously unseen terrain. In this case, learning took place off-line. Using a trial-and-error method, [37] managed to achieve on-line learning using the neural network based navigation method. The autonomous ground vehicle was equipped with 24 ultrasonic range sensors and an odometer. A goal position was set by a human supervisor or by an external path planner.

3.4.2.3 Opportunistic localization

In [6] and [13] an experimental setup of a test track, a mine created by shade cloth, is described and used to evaluate a reactive guidance and navigation system of a LHD. The guidance system utilizes laser range scanners and dead reckoning, together with a nodal map representation of the test track. The 300m long test track consists of sharp corners, intersections, a hall, and a loop. No extra infrastructure to guide the vehicle is installed. The results of the experiments show that the combination laser range scanner and reactive guidance is a feasible way to perform mine navigation. The test vehicle successfully navigated through the test track for up to one hour at a time without human interaction. Regarding the important issue of speed, the experiments showed that the control system is able to run the vehicle at the same speed as an experienced human driver. With this particular LHD, the maximum velocity of 18 km/h was achieved at parts of the test track.

The only situation in which the control system did not manage to equal the human driver was encountered at sharp intersections, where the control system could not see around the corner. Neither can the human operator, but after a few test-runs the driver remembered what the tunnel looked like around the corner, and therefore could approach the corner more aggressively. This approach can obviously be implemented in the control system as well by adding driving hints to the map. Figure 13 shows a sample topological map where the intersections are labelled. Using this map, a driving hint can be associated with a specific intersection.

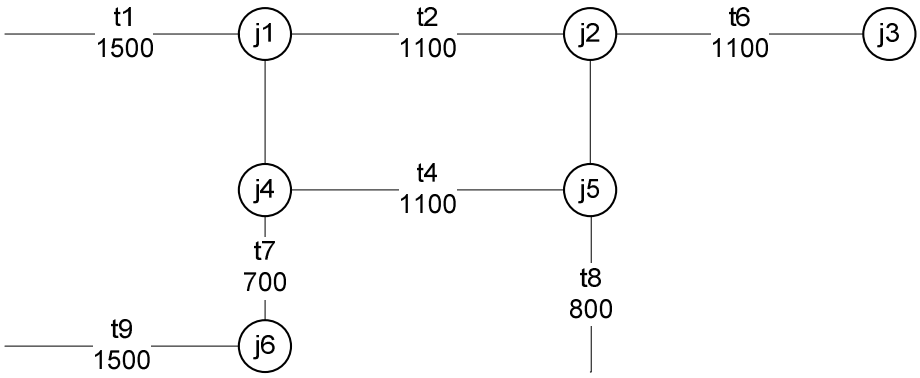

Figure 9. Fragment of a sample topological map for a mine.

The same vehicle used in the test track was also tested in a real mine environment. Again, the vehicle was able to operate at full speed through a typical production cycle without installed infrastructure or physical changes to the mine tunnel. The vehicle's ability to navigate in previously unseen tunnels was also shown by driving the LHD up the access decline (a 4 km long 1:7 slope), where a human gave high level instructions to guide the vehicle through intersections.

3.5 SIMULTANEOUS LOCALIZATION AND MAP BUILDING

The logical conclusion of the absolute navigation paradigm is Simultaneous Localization and Map Building (SLAM) or Concurrent Mapping and Localization (CML). Here, no a-priori map is required; the map is generated as the robot moves around the world for the first time.

SLAM refers to an online procedure which enables a mobile robot to build a consistent map of an unknown environment while simultaneously determining its relative location within this map. The SLAM procedure is now a well-matured research area with a number of seminal contributions by [38], [39], [40] and [41]. Nevertheless, the SLAM problem is known to be particularly difficult when the environment is a cyclic structure [39], [42] and [6]. The reason for this is that cycles pose difficult correspondence problems that arise due to the (relatively) large position error accrued by a vehicle when closing cycles (loops). Mines often contain a large number of cycles making the ability to handle cycles essential for successful approaches to mapping mines.

A number of approaches have addressed this difficulty, including [41], [42] and [43] but, because of not successfully solving the cyclic redundancy problem, none propose a viable solution to a mining environment. Today's most widely used online algorithms are based on the extended Kalman filter (EKF), whose application to SLAM problems was developed in a series of seminal papers [39]. The EKF calculates a Gaussian posterior over the locations of environmental features and the robot itself. However, the computational time required is $O(N^2)$, where N is the number of landmarks or environmental features. The number of landmarks in an underground mining environment is therefore too large for a real-time EKF SLAM algorithm implementation.

To address this problem, a different line of research has relied on particle filters for efficient mapping [44]. The FastSLAM algorithm, introduced by [45], marked a fundamental conceptual shift in the design of recursive probabilistic SLAM. Previous efforts focused on improving the performance of EKFSLAM, while retaining its essential linear Gaussian assumptions. [46] presents a recent effort to implement the FastSLAM algorithm in a mining environment. They have presented Rao-Blackwellized particle filters as an effective way of representing alternative hypotheses on robot paths and associated maps. [47] extended this idea to efficient landmark-based SLAM using Gaussian representations and were the first to successfully realize it on real robots.

However, as the name implies, landmark-based SLAM requires accurate information on the position of landmarks and their efficient re-identification. Since a typical mine is made

up of numerous long straight tunnels, few obvious natural topographical features (to act as landmarks) exist. [48] attempted to solve this problem by installing active beacons to act as reference point landmarks. Active beacons, as mentioned before, require manual installation, maintenance and are prone to be damaged by other mining vehicles.

The most successful mine-mapping methods to date, by [49] and [50], incorporate computer vision in an attempt to solve the data association problem. Computer vision is made possible by a laser range scanner (SICK laser for example). Many consecutive scans of the environment are fused together to form a single continuous image of the surroundings. This process is commonly known as the Iterative Closest Point (ICP) procedure [51]. [49] combined the ICP procedure with an EKF SLAM algorithm while [50] integrated ICP with FastSLAM. However, the results were inconsistent due to faulty data association. [52] attempted to improve the data association by replacing the EKF algorithm with Sparse Extended Information Filters (SEIF). However, the lack of recognizable landmarks hinders the algorithm to converge to a consistent global map.

As can be deduced from the above literature review, SLAM has, to date, not yet been successfully implemented in a harsh, unstructured and dynamic environment such as an underground mine.

3.6 SENSORS

In navigation, the vehicle model and the sensor model play equivalent roles in generating information and in reducing estimation uncertainty [10]. In principle, perfect (no uncertainty) sensing of all vehicle states would eliminate the need for any predictive vehicle model. Conversely, a perfect vehicle model (no uncertainty in consequent motion following a control input) would obviate the need for sensing of vehicle state. Clearly, neither of these two extremes is practical; it is not possible to purchase perfect sensors, nor to fully model the complexities of vehicle motion. However, this observation suggests that there is a trade-off between sensor suites and vehicle process models: as one becomes more accurate, the other can become less accurate while maintaining the same level of navigation system performance. To minimize the complexity and computational

requirements of the vehicle process model, researchers aim to optimize the sparse number of mining-environment applicable sensor suits.

The following position-estimation sensors can be considered in underground mining environment:

- Strap-down Inertial Measurement Unit (IMU),
- encoders,
- Guidance Control System (GCS) bearing only laser scanner,
- time-of-flight range and bearing laser scanners and
- ultrasonic sensors (Polaroid).

No satellite-dependent position sensors can be considered. The above sensors may be broken down into two broad categories, dead reckoning (internal) sensors, and external sensors. While dead reckoning sensors tend to be very robust, they accumulate error with time, so that in practice they must be periodically reset using information from the external sensors. The external sensors provide absolute information referenced to the environment, typically by making measurements of prominent known landmarks, whether they be natural or artificial. The external sensors, however, do not tend to be as reliable as dead reckoning sensors, so an advisable solution would be a navigation package of both types of sensors.

3.6.1 Encoder

Encoders are one of the most common sensors used to measure velocity or position of a rotating device. Encoders are used on both wheel rate estimation and steer angle estimation. These estimations are implemented in the particular vehicle's forward kinematic equations to obtain an approximation of position and orientation (dead reckoning). It has the advantage of being self-contained and always provides an estimate of the vehicle location. In a two dimensional planar space, provided that the starting location and all previous displacements are known, dead reckoning incrementally integrates the distance travelled and direction of travel relative to a known location. A disadvantage of encoder based dead reckoning is that the vehicle model is usually derived in two

dimensions, so the further the terrain is from a plane, the less accurate the solution. Furthermore, the current estimated vehicle position is dependent on the previous estimation cycle thus making it difficult to eliminate errors associated with the previous cycle or the current measurement (due to sensor inaccuracy).The consequence of this is that as the vehicle continues to travel, the errors accumulate and the vehicle location (position and especially the orientation) becomes less and less certain. Additionally, [41] mentions that the fact that the encoder cannot identify wheel slip adds to the overall location inaccuracy. Encoders remain, though, as the cheapest way of obtaining dead reckoning information, relatively reliably. In practice, however, [6] has shown that the errors of encoders calibrated to the distance travelled and measuring the drive shaft rotation and were less than 1% on a LHD mining vehicle.

3.6.2 Inertial Measurement Unit

The Inertial Measurement Unit (IMU) most commonly consists of a single tri-axial accelerometer and four gyroscopes [42]. The accelerometer provides three analogue outputs proportional to the acceleration on each of three orthogonal axes. Measurements made by the accelerometers are in fact a sum of effects due to linear acceleration, orientation of the platform with respect to the gravity vector and angular acceleration of the platform as it moves round a curve. The accelerometer information can also be used to determine the attitude of the vehicle while moving. This will be useful to correct dead reckoning information while operating in 3-D environments.

The most common application of inertial sensors is the use of a heading gyro. The integration of the gyro rate information provides the orientation of the vehicle. The tilt of a platform can be evaluated with two orthogonal accelerometers and knowing the gravity value in the region of operation, assuming vehicle accelerations are negligible compared to gravity. The orientation angles must be estimated very accurately as even a small fraction of gravitational acceleration attributed to true linear acceleration results in large errors. Non-linearities in the gyroscope result in errors in the measured rotations.

During operation, the inertial unit will accumulate errors with time since the need exists to integrate rate-data to yield position. An IMU with sufficient accuracy is relatively

expensive. A calibration filter needs to be implemented to reduce the platform attitude errors. This calibration filter makes use of external information to reset the gyroscope information. Furthermore, on-line calibration of these sensors is possible.

A major advantage of inertial sensors is that they are non-radiating, not prone to jamming and may be packaged and sealed from the environment. This makes them potentially robust in the harsh environmental conditions common in underground mining.

3.6.3 Guidance Control Systems laser

The Guidance Control Systems (GCS) laser is a commercially available sensor widely used to solve the positioning problem. The laser rotates horizontally at approximately 1 Hz, scanning 360 degrees in azimuth. The rotating head has an encoder mounted, so the angle to a known retro-reflective target is the returned value. This laser is typically mounted on top of the vehicle, clear of obstructions. In indoor applications, where the speed of the vehicle is small compared to the target update rate, triangulation may be used without much loss in precision. This approach presents problems, however, when the vehicle has moved substantially between updates. In this case, a data fusion algorithm such as the Kalman filter must be employed.

[43] found that this sensor is exceptionally reliable. However, this sensor is sensitive to vibrations. A target could be detected more than once since the vibration of the vehicle induces a slight net backwards motion in the sensor. If packaged properly, this sensor can be robust enough to withstand the harsh environment in underground mining.

3.6.4 Time-of-flight laser scanner

A time-of-flight laser scanner can be implemented to create a 3D representation of its surroundings by using a laser rangefinder. The distance to a surface is found by sending a pulse of light in the direction of the surface and timing the duration taken for the reflected pulse to return. The light pulse is generated by a laser.

It has been shown by [43] that a 3D profile of a tunnel wall can be constructed very efficiently, but the system was susceptible in very dusty environments. A 3-D model is

potentially useful when considering the collision avoidance problem and is an exceptionally good way of identifying tunnel features.

However, the sensor operates using a rotating mirror; long term exposure to vibration may cause untimely degradation in performance. In addition, the lifespan of laser diodes used in the laser sensor are known to reduce with exposure to elevated temperatures such as those found in underground mines.

3.6.5 Ultrasonic

Ultrasonic sensors are also time-of-flight devices used for a large variety of applications. These sensors come in many shapes and forms, only some of which are suitable for use in an underground environment. A very reliable ultrasonic sensor, the Polaroid family of ultrasonic transducers, suffers in a dusty environment due to the fact that the vibrating element is open to the environment. The MASA family of ceramic ultrasonic transducers, however, is a sealed unit and is more robust in harsh environments. The deficiency of ultrasonic sensors is its accuracy. As a navigation aid, the ultrasonic sensor can be used to detect gross changes in the features of underground tunnels, such as side tunnels and similar features. Map matching techniques can be used to improve the efficiency of the sensor.

3.6.6 Discussion

The selection of a particular sensor configuration is dependent on a number of factors including terrain conditions, the duration of the run, unmodelled vehicle parameters, wheel slippage, sensor noise and quantization effects, to name a few. Due to wheel slippage and fast cornering, the errors associated with the dead reckoning sensors accumulate over time and will need periodical resetting. Any navigation sensor suite thus will have to invariably contain both internal and external sensors. Common configurations are: a dead-reckoning and an external sensor, and an IMU and an external sensor. The former coupled system is dependent on the manoeuvres of the vehicle and the vehicle’s kinematic and dynamics while the latter is not so dependent on the kinematics and the manoeuvres but relies on the run-time of the application and enough information needs to be available for periodical resetting. The most popular external sensor is the laser rangefinder accurate imaging.

3.7 COMMERCIALLY AVAILABLE NAVIGATION SYSTEMS

The following three infrastructure-free navigation systems are used for the automation of LHD vehicles in mines today:

- AutoMine, developed by Sandvik together with Finnish universities,
- MINEGEM, developed by Caterpillar together with CSIRO and Australian universities and
- Scooptram automation system, developed by Atlas Copco.

3.7.1 AutoMine

The Sandvik AutoMine system is an infrastructure-free LHD and truck automation system, based on absolute navigation techniques, that allows the operator to sit in the comfort of a control room to monitor a fleet of automated mining vehicle [53]. The hauling and dumping procedure is fully automated whereas the loading action requires tele-operated input from a human operator.

AutoMine is a modular system that can be adapted to suit a variety of customer requirements:

- Production Control System (PCS) is used for planning, optimization of production execution and reconciliation of production inputs and outputs,
- Mission Control System (MCS) is a supervisory system to control and monitor the automated vehicles, acting as the remote operator's user interface,
- MineLAN is a broad band communication system to provide a high speed connection between the automated underground vehicles and their associated equipment,
- Onboard automation system is used for machine control, monitoring and navigation and
- Access Control System (ACS) aims to restrict access to the autonomous operating area, ensuring safety of personnel.

This system has been implemented at Inmet Mining's Pyhäsalmi base metal mine in Finland, Codelco's El Teniente copper mine in Chile, Williams Mine in Canada and at Finsch, a DeBeers-owned diamond mine in South Africa.

The Finsch mine has become a world-leader in mine automation and safety. They decided to implement a Sandvik AutoMine system in their fourth underground mining block in 2005. In two years, automation has been completed to the point where autonomous trucks navigate a haulage loop between the loading points at the block cave and the primary crusher located close to the main hoisting shaft underground. The benefits of this automation system include higher utilization of the dump trucks and LHDs. The automated trucks tram at far higher speeds than conventional trackless fleets, which allows the mine to produce more ore.

In terms of being economically feasible, the AutoMine system paid for itself in the first two years of full production. Also, fewer mining equipment needed to be purchased by virtue of the fact that efficiency, utilization and the cost of running the equipment is lower.

The manually operated LHDs travel from the draw point to the transfer point, where the automated dump trucks travel in continuous loop from the transfer points to a crusher. Guided by an infrastructure-free navigation system, the computer controlled trucks use laser scanners to negotiate their route. The trucks have two onboard cameras and a scanner on the front and another scanner and camera on the back. The scanners have to be cleaned at the end of each shift. The operational hours of the trucks are also increased; human fatigue is not an issue anymore. Legislation wise, trucks are only allowed to travel at a maximum speed of 16 km/h with operators onboard. The autonomous, operator-free trucks, however, are allowed to travel with speeds of up to 35 km/h, increasing the cycle time and the production of more tons per day.

3.7.2 MINEGEM

Similar to the AutoMine system, Caterpillar's MINEGEM semi-autonomous system provides automated hauling and dumping for LHD vehicles [54]. The system can be set to either auto- or co-pilot mode. In the co-pilot mode, an operator steers the vehicle from a control room, using a joystick to control the machine's direction. In the auto-pilot mode,

the LHD vehicle can be sent by the operator to a specific goal; it arrives there using a self guidance system. An operator is able to handle several machines simultaneously in the auto-pilot mode.

MINEGEM is based on reactive navigation and opportunistic localization, meaning that the system reacts to its immediate surroundings. LHD vehicles are equipped with laser range finders, cameras and on-board computers to navigate its way within a predefined mine map. According to [54], MINEGEM improves productivity, utilisation of equipment, safety and LHD operating lifetime.

3.7.3 Scooptram automation system

Atlas Copco's Scooptram system also allows automated hauling and dumping [55]. Initially, the desired path is driven manually in order to allow sensors to capture data to build a route profile. A Route Manager software verifies and approves the route. During automated driving, on-board sensors, including two laser towers, an inertial measurement unit, a hinge angle encoder and inductive odometry sensors determine the LHD's position and orientation within the taught path and the vehicle is navigated to the desired target. A WLAN system allows communication between the respective automation equipment. Furthermore, the system allows a smooth transition between automated to tele-operated modes.

Figure 10 shows an overview of the automation system.

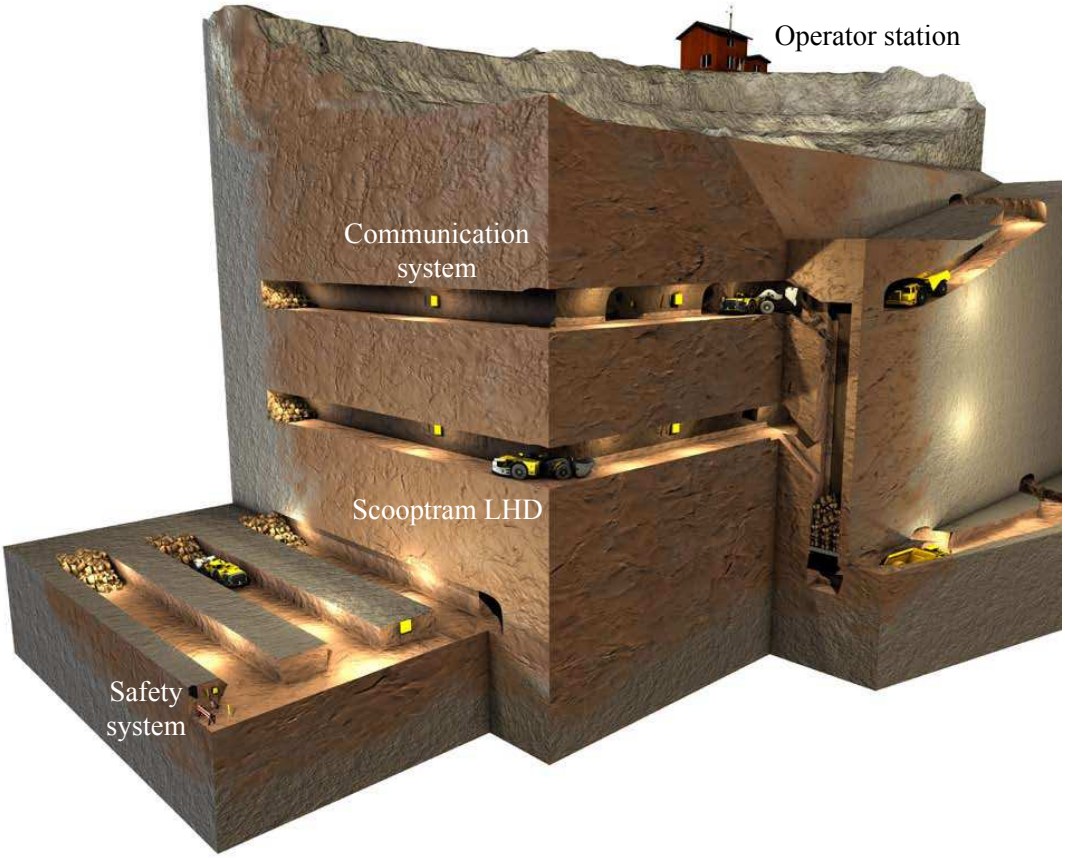

Figure 10. Overview of the Scooptram automation system, from [55].

3.8 CHAPTER SUMMARY

The two navigation schemes, absolute and reactive navigation, were discussed. Regardless of which navigation scheme is implemented, an infrastructure-free system is the only system that is plausible in an underground mining environment. The sensors required for this kind of system have been mentioned in this chapter while their performance has also been discussed.

CHAPTER 4

LHD VEHICLE MODELLING

The key to designing navigation systems for autonomous vehicles is the model which describes how the vehicle's position and other key vehicle parameters evolve through time. The model is essential to make good use of sensor data and for describing how unobserved vehicle parameters affect vehicle motion.

There are two ways to model the mobile robot: kinematically or dynamically. In a kinematic model, only the movement of the vehicle is considered. The model is derived using the nonholonomic constraints inherent in the vehicle. The kinematic model is fairly easy to derive and is simple in form. However, this model fails to account for acceleration and can differ greatly from actual movement when the vehicle's handling limits are approached. Because of its simplicity, many researchers use the kinematic model and place emphasis on designing robust controllers. Importantly, kinematic modelling allows for the decoupling of vehicle dynamics from its movement.

On the other hand, dynamic modelling accounts for the properties of the vehicle related to its acceleration such as mass and centre of gravity. This type of modelling is much more true to the actual behaviours of the vehicle, but the resulting system representation is much more complicated. It gives a more accurate depiction of the vehicle's behaviour.

First of all, the various types of kinematic models of the LHD are given. Then, the dynamic aspect of vehicle modelling, which heavily depends on an accurate tyre/road interaction model, is discussed.

4.1 KINEMATIC MODEL

Kinematic modelling refers to the study of the mathematics of motion without considering the forces that affect the motion. It deals with the geometric relationship that governs the system. Also, kinematic models deal with the relationship between control parameters and the behaviour of a system in state-space. A planar motion is normally assumed and, most importantly, when the speed is low the effects of the dynamics of the system can be neglected. Due to obvious safety reasons and the structured and harsh environment of the underground mine, the speed of underground mining vehicles are kept relatively low. It is for this reason that the kinematic model of the LHD is most often used in localization and control [51]. The variables defined in this section are, unless stated otherwise, time dependant. For simplicity, the time dependency notation has been omitted.

4.1.1 Basic kinematic model

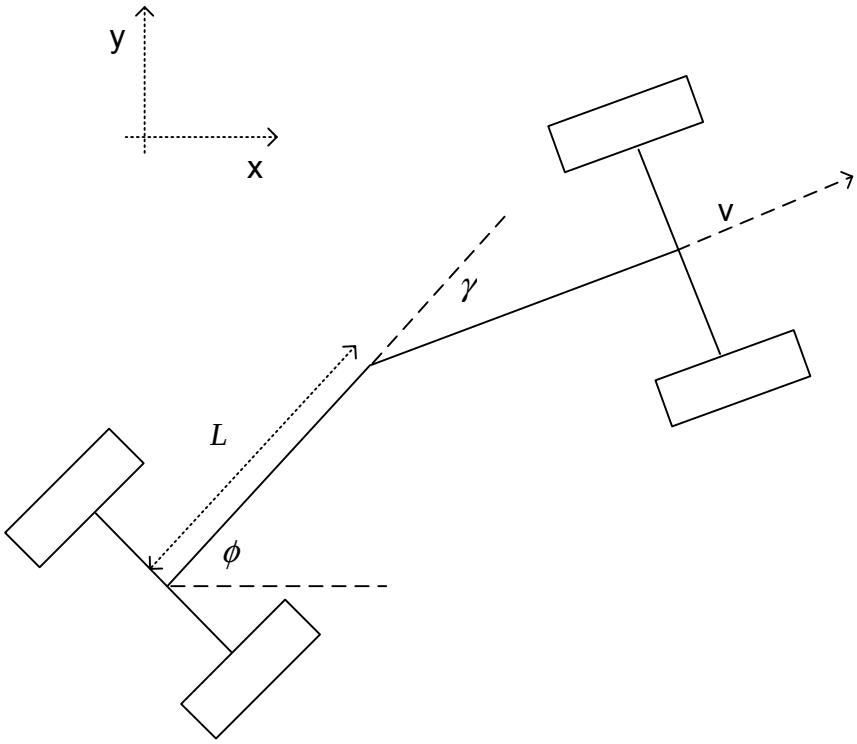

Figure 11. LHD kinematic geometry.

[56] derived a pure, no-slip kinematic model for a LHD from Figure 11. The model was derived from rigid body and rolling motion constraints and is given as follows:

$$\dot{x} = v\cos(\phi), \tag{4.1}$$

$$\dot{y} = v\sin(\phi), \tag{4.2}$$

$$\dot{\phi} = \frac{v\tan\left(\frac{\gamma}{2}\right)}{L}, \tag{4.3}$$

where x and y are the global coordinates, v is the velocity of the front body, ϕ is the yaw of the rear body with respect to the x axis, γ is the articulation angle and L is the vehicle's fixed half-length. [56] assumes that the articulation joint is equidistant from the front and the rear axle. The model is based on a steady-state cornering theory, meaning that $\dot{\gamma}$ is assumed to be zero. In practice, however, the articulation angle constantly changes rendering this simple approach inaccurate. Also, this model predicts that γ is always zero at zero velocity, but this is not observed in practice; articulating the vehicle while it is stationary, but with the brakes off, causes the front and the back parts of the vehicle to rotate. The effect of omitting slip in kinematic modelling is discussed in section 4.1.4.

4.1.2 Full kinematic model

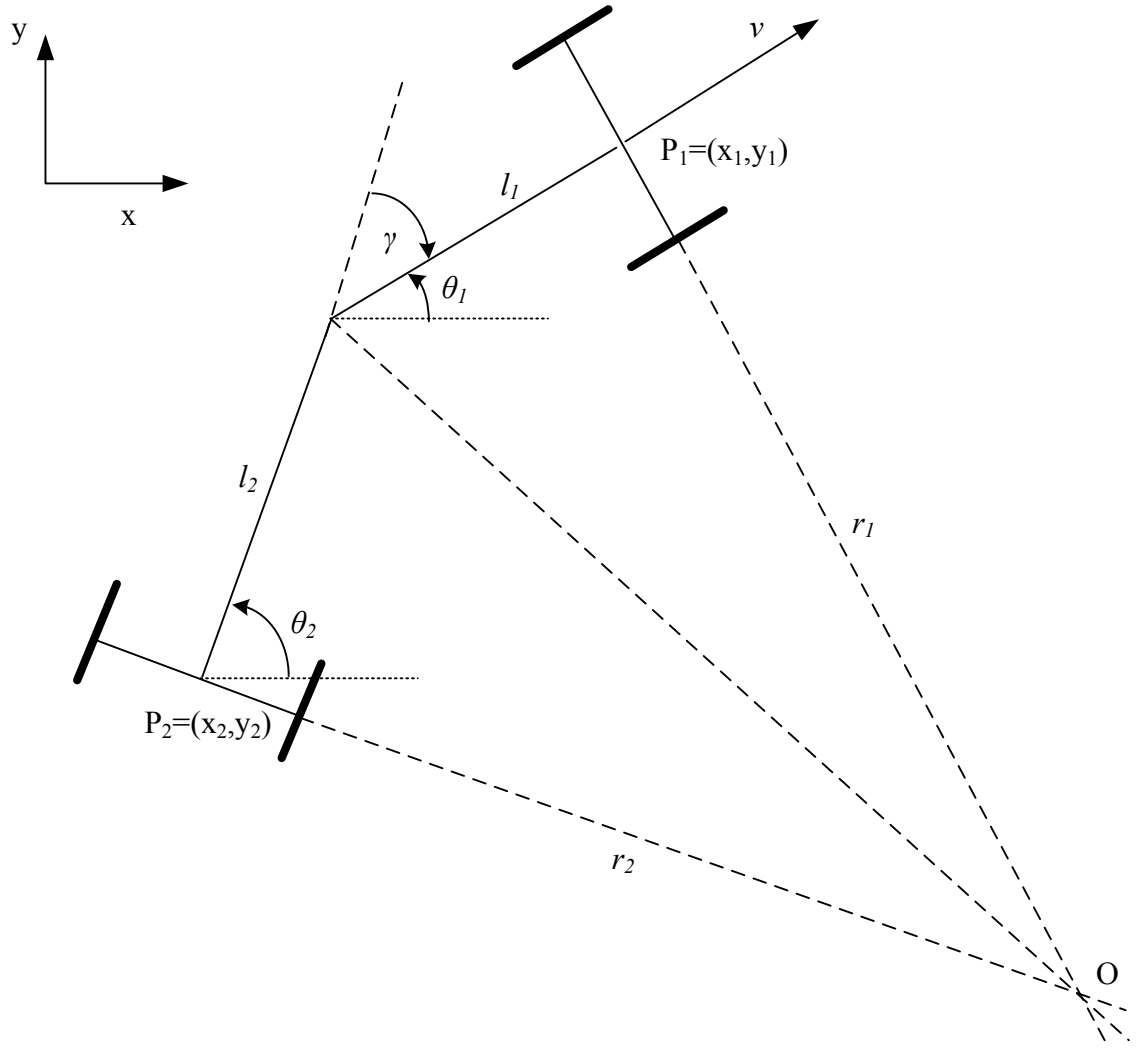

Figure 12. The kinematic behaviour of the articulated LHD vehicle, reprinted from Chapter 2.

The assumption of having the articulation joint exactly halfway between the front and the rear axles is not always applicable. With reference to Figure 12 and [56], one can write for the front unit

$$\dot{x}_1 = v\cos\theta_1, \tag{4.4}$$

$$\dot{y}_1 = v\sin\theta_1, \tag{4.5}$$

where v is the velocity of the vehicle, x_1 and y_1 are the global reference coordinates and θ_1 is the yaw of the front unit. P_1 and P_2 are the fixed centres of the front and the rear units, respectively. The relationship between P_1 and P_2 is given by

$$x_2 + l_2 \cos\theta_2 + l_1 \cos\theta_1 = x_1, \tag{4.6}$$

$$y_2 + l_2 \sin\theta_2 + l_1 \sin\theta_1 = y_1, \tag{4.7}$$

where l_1 and l_2 are the fixed lengths of the front and rear units, respectively, and θ_2 is the yaw of the rear unit. Also, the yaw of the front unit with respect to the x-axis is given by

$$\theta_1 = \theta_2 - \gamma. \tag{4.8}$$

The nonholonomic constraint on wheel rolling without slipping implies that no motion parallel to the axles is present. Therefore the following relations can be stated:

$$\dot{x}_2 \sin\theta_2 - \dot{y}_2 \cos\theta_2 = 0, \tag{4.9}$$

$$\dot{x}_1 \sin\theta_1 - \dot{y}_1 \cos\theta_1 = 0. \tag{4.10}$$

In order to find the yaw rate of the front unit, θ_1, equations (4.6) and (4.7) were differentiated, substituted in (4.4), (4.5), (4.9) and (4.10), and then simplified to get

$$\dot{\theta}_1 = \frac{-v\sin\gamma - l_2\dot{\gamma}}{l_1\cos\gamma + l_2}. \tag{4.11}$$

4.1.3 Kinematic model with slip

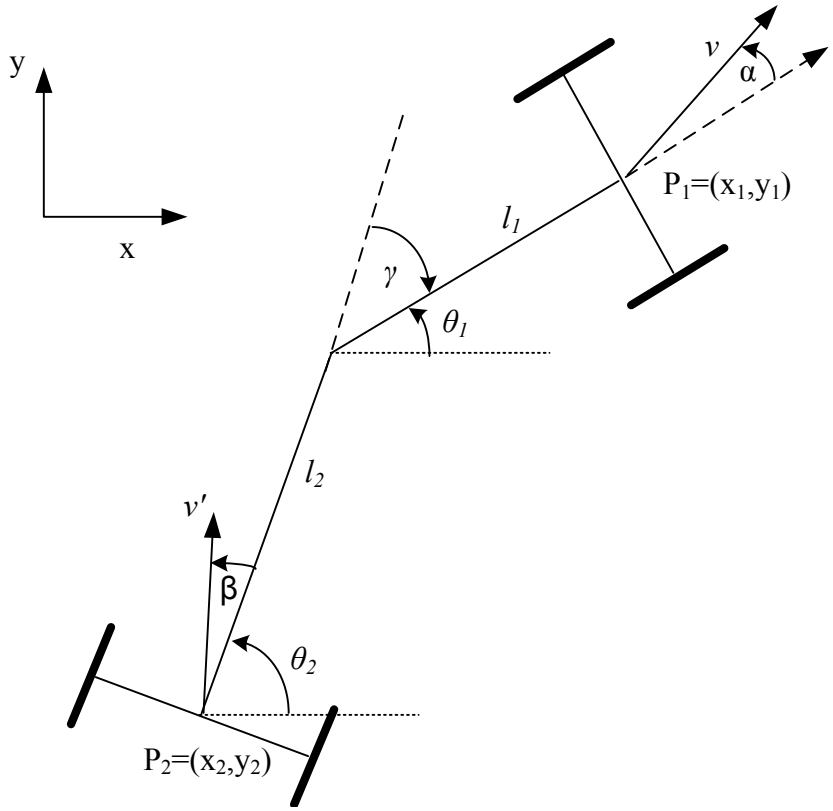

Figure 13. Kinematic geometry of an LHD including the slip angles.

[11] evolved the kinematic model of equations (4.1) and (4.2) to take into account that the vehicle will slip during motion. The slip variables α and β are introduced to represent the slip angles of the LHD. The slip angle of a vehicle is the angle between the kinematically indicated velocity and the true velocity. The variation between true and kinematic velocities is by definition entirely dependent on the slip. When including the slip angles, the velocity in the x and y direction for the rear unit become

$$\dot{x} = v'\cos(\alpha + \theta_2), \tag{4.12}$$

$$\dot{y} = v'\sin(\alpha + \theta_2). \tag{4.13}$$

With reference to Figure 13, the following equation is obtained by determining the velocity of the front unit, P_1, in the direction perpendicular to v and setting this equal to zero:

$$v'\sin(\alpha-\beta-\gamma)+l_1\cos(\beta+\gamma)\dot{\theta}_2+l_2\cos(\beta)(\dot{\theta}_2+\dot{\gamma})=0\,. \tag{4.14}$$

Solving this for the yaw rate of the rear body, $\dot{\theta}_2$, results in

$$\dot{\theta}_2=\frac{v'\sin(\beta-\alpha+\gamma)-l_2\dot{\gamma}\cos(\beta)}{l_1\cos(\beta+\gamma)+l_2\cos(\beta)}\,. \tag{4.15}$$

[56] presents similar results for the yaw rate but, as mentioned before, assumes that $l_1 = l_2$. Rearranging (4.12), (4.13) and (4.15) such that the expression relates to the front unit and using the general notation of $\theta_1=\phi$, then the pose of the front unit is given as

$$\dot{x}=v\cos(\alpha+\phi)\,, \tag{4.16}$$

$$\dot{y}=v\sin(\alpha+\phi)\,, \tag{4.17}$$

$$\dot{\phi}=\frac{-v\sin(\beta-\alpha+\gamma)-l_2\dot{\gamma}\cos(\beta)}{l_1\cos(\beta+\gamma)+l_2\cos(\beta)}\,. \tag{4.18}$$

4.1.4 Slip and kinematic modelling

Since kinematic modelling is based on the pure rolling motion of a vehicle, it does not incorporate any slippage (longitudinal or lateral) that the vehicle may undergo. To compensate for the positioning error that will inevitably result, various methods to include the effects of slip have been proposed and developed, as in [11] and [56].

4.1.4.1 Proof of slip existence

The no-slip kinematic model of equations (4.1) - (4.3) are vastly different from equations (4.16), (4.17) and (4.18), which include the slip angles. Without the inclusion of the slip angles, the model will overestimate the turning rate significantly, causing the navigation system to constantly attempt to rectify the modelling error. Looking specifically at the expression for the yaw rate, $\dot{\phi}$, equation (4.18) most notably includes the effect of the articulation angle rate, $\dot{\gamma}$.

By looking at the relationship between the front and rear unit velocities, it is possible to gain insight into why the articulated vehicle does slip. With reference to Figure 13, the velocity of the rear unit can be derived to be

$$v' = \frac{v\left(\cos(\alpha-\gamma)+\cos(\alpha)\right)-l_2\dot{\gamma}\sin(\gamma)}{\cos(\beta)+\cos(\beta+\gamma)}. \tag{4.19}$$

By design the vehicle drives both the front and rear wheel sets at the same angular velocities. If no slip is present, equation (4.19) reduces to

$$v' = v - l_2\dot{\gamma}\tan\left(\frac{\gamma}{2}\right). \tag{4.20}$$

This indicates that slip has to be present if the articulation is not constant or zero.

4.1.4.2 Dealing with slip in kinematic models

It is clear that including the slip angles in the kinematic models of articulated vehicles will improve the model. Since the slip angles are very difficult to measure directly, they are estimated. Due to the unavailability of GPS data in the underground environment, the pose estimation of the LHD is a challenging task and hence makes the estimation of the slip angles even more difficult. A number of methods exist which attempt to estimate these angles or attempt to eradicate the effect induced by the slip phenomenon by treating it as an external disturbance in the control architecture.

The procedure adopted by [11] treats the slip angles, α and β, as additional states in the model. Modelling the errors of the slip angles is a daunting task since they tend to involve a combination of other parameters and are caused mainly by the non-linear vehicle dynamics. Speed, mass, tyre-terrain interaction and articulation angle all have an influence on the slip angle. [11] and [49] approximate the slip angles by directly relating the vehicle's pose error to the slip angles. An Extended Kalman Filter is used to estimate the vehicle's actual pose whereby the error between model prediction and sensor result is attributed to the slip angles.

Another method of estimating the amount of slip mostly used on automated highway systems is to measure the lateral and longitudinal velocities at the front and rear axles of the vehicle, as is attempted by [57]. Sensors are placed in line with the axles and not at the vehicle's centre of gravity. The slip angles of the front and rear tyres, α_f and α_r, are given by

$$\alpha_i = \delta_i - \tan^{-1}\frac{v_i}{u_i},\ i = f,\ \mathrm{r} \tag{4.21}$$

where u_i and v_i are the longitudinal and lateral velocities at the *ith* tyre and δ_i is the steering angle of that tyre. In the case of articulated vehicles, the steering angle will be that of the articulated angle, γ, as given in Figure 13. Only the vehicle's kinematic model is required meaning that the dynamic parameters such as vehicle mass, inertia and cornering stiffness are irrelevant. The problem with this method is that guidance infrastructure, such as reflective tape or beacons, is a necessity in order to accurately update the vehicle's displacement. Magnetometers, placed as close as possible to each of the tyres, are used to periodically sense the passing beacons.

The third approach commonly used is to assume a no-slip condition and hence correct the positioning error by means of path tracking control. The kinematic model of (4.4), (4.5) and (4.11) is therefore chosen. Both dead reckoning (encoders, inertial sensors, rate gyroscopes and accelerometers) and external sensors (laser and ultrasonic scanners) are used to estimate the pose of the vehicle. External sensors are implemented to identify the tunnel walls in the underground environment.

A path-tracking method by [58] is an applicable example. According to [58], a path down the middle of the tunnel in the vicinity of the vehicle can be computed from the sensor data. Hence errors in displacement (ε_d), heading (ε_θ) and curvature (ε_c) of the vehicle path compared with the tunnel path can be identified. Figure 14 shows three target points, T1, T2 and T3, and the target circle C, with radius R. The control system attempts to keep point P on the circle C while continuously keeping errors ε_d, ε_θ and ε_c to a minimum.

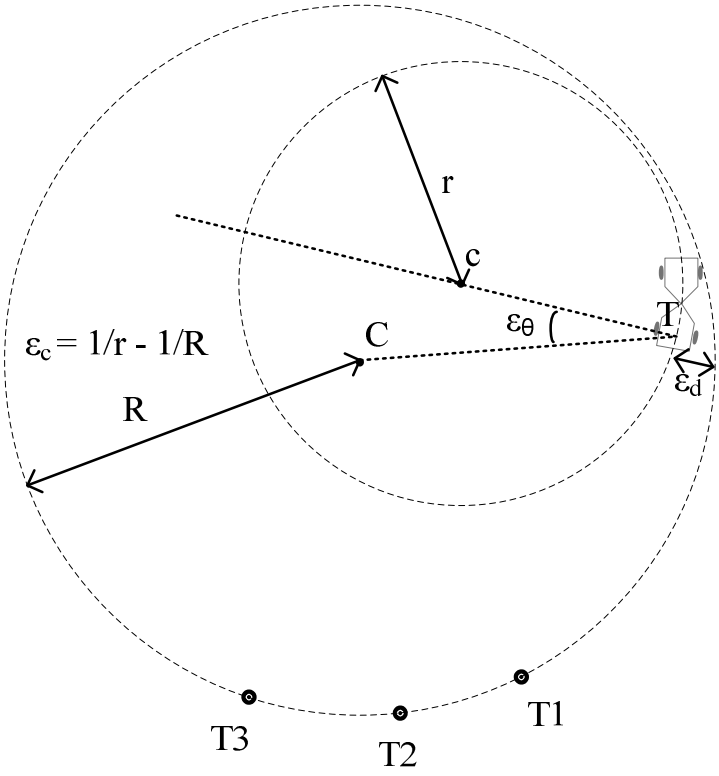

Figure 14. Displacement, heading and curvature error, ε_c, is shown.

If circle c initially started out on circle C and no slip was present, then the positioning errors would always be zero. However, from equation (4.20), it was shown that slip will be present if the vehicle changes its articulation angle, *i.e.* if new target points are selected and circle C changes. The path-tacking method will hence continuously fight to correct the no-slip modelling error.

4.2 DYNAMIC MODELLING

Whereas kinematic equations describe the motion of the vehicle without consideration of the forces and torques producing the motion, the dynamic equations explicitly describe the relationship between force and motion.

Friction force at the tyre/road interface is the main mechanism for converting motor torque to longitudinal force, and is also closely related to vehicle steering. The accuracy of a dynamic vehicle model highly depends on the precision of the tyre/road friction modelling.

The main task of tyre/road friction modelling and monitoring is to determine the relationship between friction forces and longitudinal/lateral slip ratios. The tyre/road friction concept, however, is not easy to analyze.

4.2.1 Tyre longitudinal dynamics

Tyre longitudinal dynamics mainly presents tyre rolling resistance, the slip coefficient, and the relationship between the tyre traction and brake forces and the road condition.

4.2.1.1 Tyre rolling resistance

The rolling resistance of the tyre, which is applied to the wheel, is due to the deformation of the tyre at the tyre/road interface. The energy that is dissipated by this deformation of the tyre leads to rolling resistance. Usually, tyre rolling resistance (F_r) changes linearly with the normal force of the wheel:

$$F_r = \mu_x F_z; \tag{4.22}$$

which implies

$$\mu_x = \frac{F_z}{F_r}. \tag{4.23}$$

The non-dimensional coefficient μ_x is defined as the rolling resistance coefficient; it is the ratio of the driving force and the normal force, F_z, on the rolling wheel in certain conditions. Experiments show that the rolling resistance coefficient is proportional to the tyre deformation, while being inversely proportional to the radius of the tyre. According to [59], if the velocity of the vehicle is less than 50 km/h, then μ_x will be 0.0165. In the case of underground mining vehicles, speeds rarely exceed 20 km/h.

The longitudinal wheel slip s_x can be defined as

$$s_x = \begin{cases} 1 - \dfrac{R\omega}{v_x}, \text{ if } v_x > R\omega,\ v \neq 0, \text{ braking} \\ 1 - \dfrac{v_x}{R\omega}, \text{ if } v_x < R\omega,\ \omega \neq 0, \text{ driving} \end{cases} \tag{4.24}$$

where R is the effective radius of the wheel, ω represents the angular velocity of the wheel, and v_x represents the longitudinal velocity.

Figure 15 displays the typical variation trends between the normalized longitudinal tyre friction, μ_x, and the slippage, s_x, under different road surfaces while Figure 16 shows the same relationship at different velocities [59].

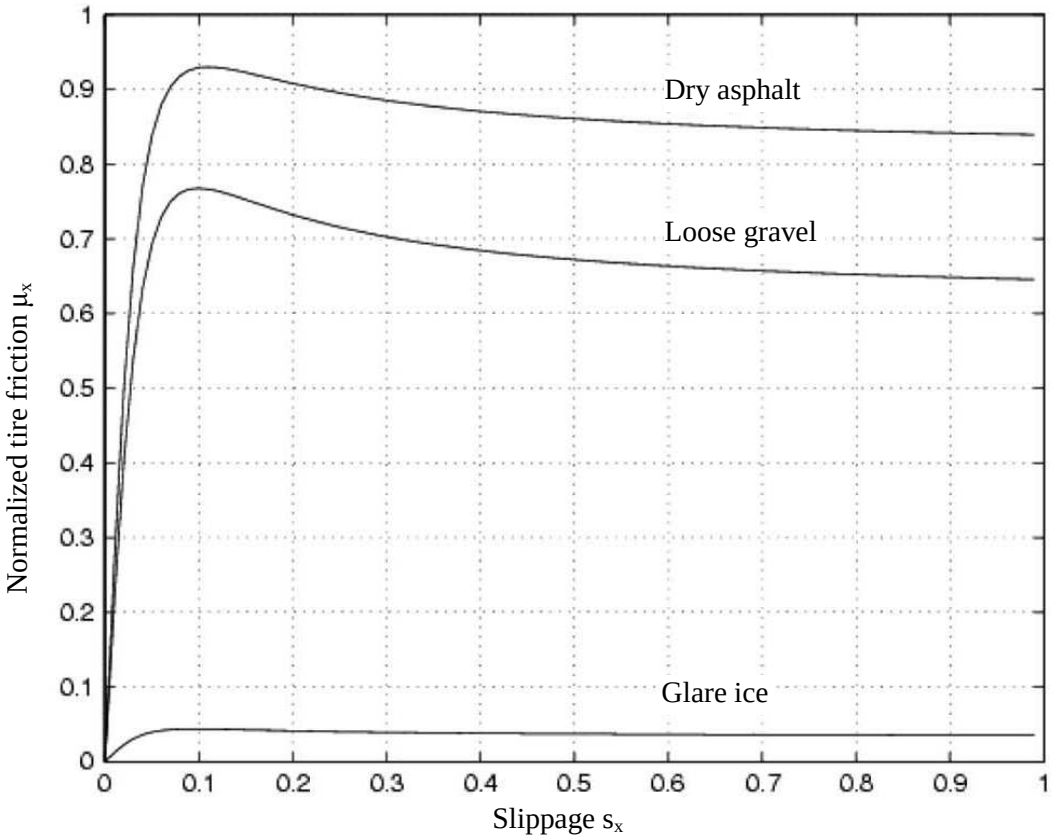

Figure 15. Longitudinal tyre friction on various road surfaces.

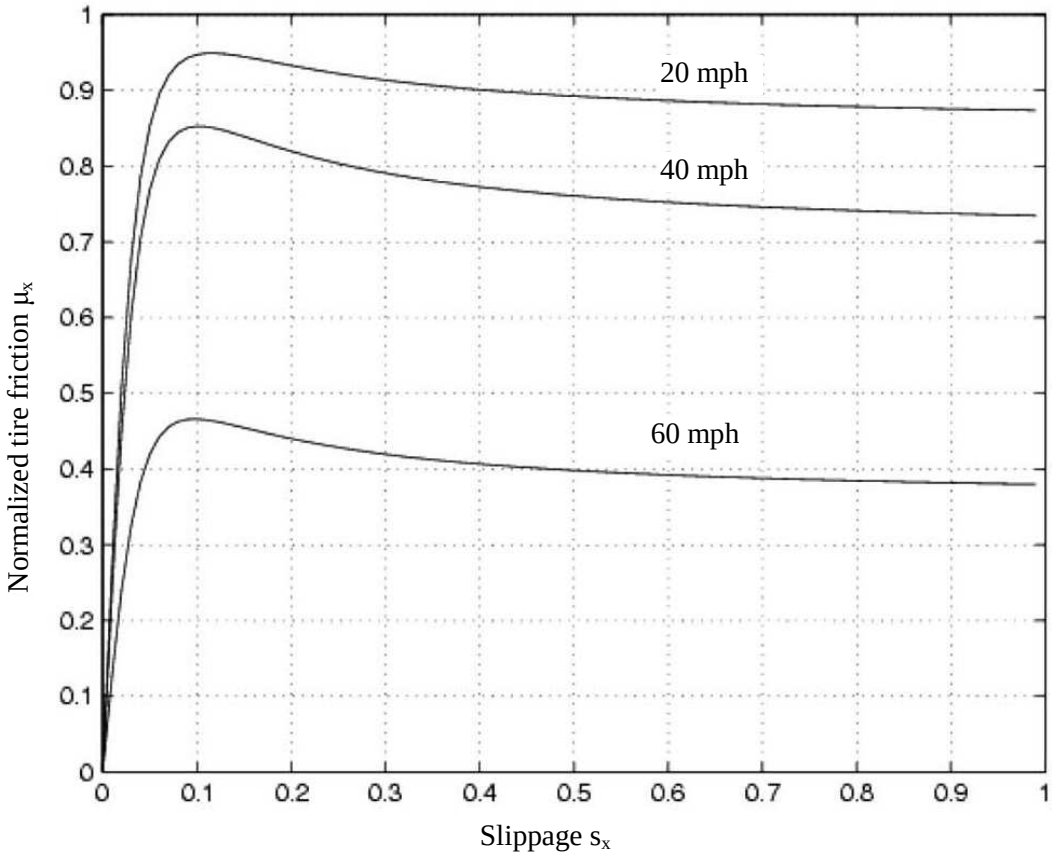

Figure 16. Normalized longitudinal tyre friction at various vehicle speeds.

As shown in Figure 15 and Figure 16, μ_x is a nonlinear function of s_x with a distinct maximum. The relationship between μ_x and s_x can be clearly distinguished into two parts: the steady rising part and the local sliding part (in which μ_x gradually decreases). Performance on slippery roads is qualitatively similar to dry roads, differing primarily in the peak level of friction force that can be achieved. Since the initial, almost linear rate at which friction force builds up with slip is dependent on tyre stiffness properties, the initial slope is very similar at various speeds.

The Factors which affect the friction force are:

- Vertical load: Friction coefficients generally reduce if the vertical load is increased.
- Inflation pressure: On dry roads, the peak friction coefficient is only mildly affected by inflation pressure. On wet surfaces, however, inflation pressure increases are known to significantly improve the peak friction coefficient value.

- Surface condition: With reference to Figure 15, μ_x increases when the road surface becomes rougher.
- Speed: On dry roads, the peak and sliding μ_x values decrease with velocity as illustrated in Figure 16.

Longitudinal traction properties are the properties of the tyre/vehicle system that determine braking performance and stopping distance. The peak value of the friction coefficient μ_x determines the limit for braking when the wheels do not lock up. Also, longitudinal traction properties may also determine acceleration or hill-climbing performance of a vehicle. The acceleration could be limited to ensure that the peak coefficient is not transgressed. Limiting longitudinal slippage in this way will reduce odometry and positioning errors. Tyre/road friction models are therefore required to estimate the longitudinal forces acting on the wheels.

4.2.1.2 Longitudinal tyre/road friction models

Longitudinal tyre/road friction models can be classified in three main types: empirical, semi-empirical and analytical. Empirical techniques are based on curve-fitting techniques which represent the μ_x - s_x curve as a linear or non-linear function. According to [60], empirical models can accurately represent the steady-state characteristics of tyre/road friction, but they cannot describe several significant dynamic behaviours such as hysteresis. That is why these were also often called static models. Furthermore, these do not include the effects of physical tyre parameters and cannot directly show the effects of some special influences such as humidity and tyre pressure. Semi-empirical models, however, incorporate, to some extent, the effects of varying physical tyre parameters.

On the other side, analytical models use differential equations to represent the tyre/road friction. The dynamic effects acting on the tyre, including the forces and torques, make up the differential equations. The most popular analytical model is the Brush model, presented in [61] and [62].

4.2.1.2.1 Piecewise linear model

The Piecewise linear model is the simplest form of representing the μ_x - s_x relationship. With reference to Figure 15, the model approximates the μ_x by a linear function which passes through the origin, the maximum value of μ_x and the final steady-state value of μ_x. Due to its simplicity, this model is widely used [63], [64], [65], mainly in cases where the nonlinear dynamic characteristics of tyre/road friction are not deemed to be of significant importance.

4.2.1.2.2 Burckhardt model

The Burckhardt model is proposed by [66] and is a frequently mentioned model. The original model was written as follows:

$$\mu_x = \left[C_1 \left(1 - e^{-C_2 |s_x|}\right) - C_3 |s_x| \right] e^{-C_4 v_x}, \tag{4.25}$$

where C_i, i = 1,...,4, are parameters that are derived from experimental data. With accurately assigned C_i, the equation can approximate the μ_x - s_x curve. According to [64], the parameter identification cost is relatively high and hence [57] modified the model in order to simplify parameter identification. The revised model is given as

$$\mu_x = C_1 e^{-C_2 |s_x|} \cdot |s_x|^{(C_3 |s_x| + C_4)} \cdot e^{-C_5 v_x}, \tag{4.26}$$

which, by using the linear logarithm, can be identified more readily than equation (4.25).

4.2.1.2.3 Rill model

The Rill model proposed in [67] is a semi-empirical model. It is based on steady-state force/torque characteristics of a tyre together with a simple transient tyre deflection model. It calculates the slip in steady-state and a corresponding tyre force using a curve fit with initial inclination at $s_x = 0$ and location/magnitude of the peak μ_x and the final steady state μ_x value as parameters. The nonlinear dependence of the vertical load is handled by an interpolation between a set of the parameters for predefined-load cases.

4.2.1.2.4 Magic formula

In 1980, an empirical formula in which the properties shown above could be described in closed form [68]. It was originally written as

$$\mu_x = C_1 \sin\left(C_2 \tan^{-1}\left\{C_3 s_x - C_4\left[C_3 s_x - \tan^{-1}\left(C_3 s_x\right)\right]\right\}\right), \tag{4.27}$$

where C_i, i = 1,..,4, are determined through experiments.

The “magic formula” is presently the most important semi-empirical tyre friction model. However, it is over-parameterized and thus difficult to analyze.

4.2.1.2.5 Dahl model

Dahl developed a comparatively simple tyre/road friction model in the 1970s, which is basically a generalization of Coulomb friction. The frictional hysteresis during pre-sliding is approximated by a generalized first-order equation of the position depending only on the sign of the velocity [69].

Specifically, Dahl proposed the following equation

$$\frac{dF}{dt} = \sigma_0 \left(1 - \operatorname{sgn}(v_r) \cdot \frac{F}{F_s}\right)^{\delta_d} v_r, \tag{4.28}$$

where σ_0 denotes the initial stiffness at velocity reversal, δ_d denotes a model parameter determining the shape of the hysteresis, and v_r is the relative moving speed. The nominal contribution of the Dahl model is that the model represents the stress-strain curve as a differential equation. It also incorporates important phenomena of friction including zero slip displacement and hysteresis. The main drawback of the Dahl model, however, is that it does not describe the relationship between the velocity and the friction. Dahl’s dynamic-modelling idea led to the development of several other analytical models, most notably the LuGre model.

4.2.1.2.6 LuGre model

The LuGre model combines the merits of the Dahl model with several other steady-state characteristics, *e.g.*, the Stribeck curve. Since the LuGre model is still a first-order model, it is easier to analyze than most second-order models. In [70], it is further shown that a slightly modified LuGre model can incorporate disturbance caused by unsteady road surfaces.

Because of its simplicity and convenient combination of pre-sliding and sliding into one equation set, the LuGre model has become a popular model for friction compensation and estimation after its initial presentation.

Table 4 summarizes the longitudinal tyre friction models.

Table 4. A summary of the mentioned longitudinal tyre/road friction models.

Model Name	Model Type	Main Features
Piecewise Linear Model	Empirical	1. Cannot accurately fit curves 2. Easy to identify
Burckhardt Model	Semi-Empirical	1. Can accurately fit curves 2. Has some revised formula
Rill Model	Semi-Empirical	Easy to identify
Magic Formula	Semi-Empirical	1. Can accurately fit curves 2. Has many revised formulas 3. Can employ different factor
Dahl Model	Analytical	1. Can describe Coulomb friction 2. Can produce smooth transition around zero velocity
LuGre Model	Analytical	1. Can combine pre-sliding and sliding in addition 2. Can capture the Stribeck effect

4.2.2 Tyre lateral dynamics

In the cornering process, the tyre develops a lateral force and will experience lateral slip associated with a slip angle. With reference to Figure 17, the slip angle is the angle between a rolling wheel's actual direction of travel and the direction towards which it is pointing.

.

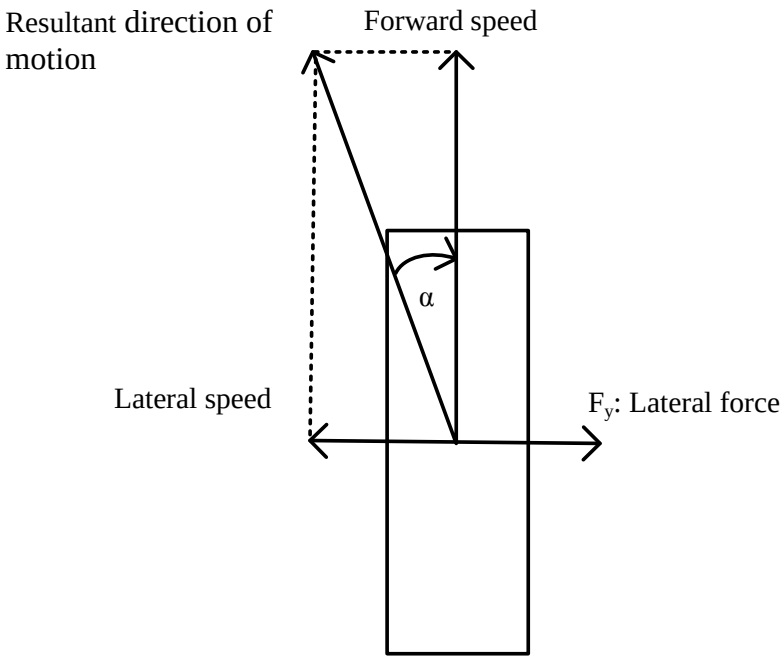

Figure 17. Definition of the tyre forces.

Here, the lateral force, F_y, is defined as the cornering force. [68] showed that the cornering force increases as the slip angle increases for a given tyre load. Figure 18 shows the cornering force as a function of the slip angle for various road adhesion coefficients. The lateral force initially increases with an increased slip angle but then saturates as the slip angle reaches a certain maximum.

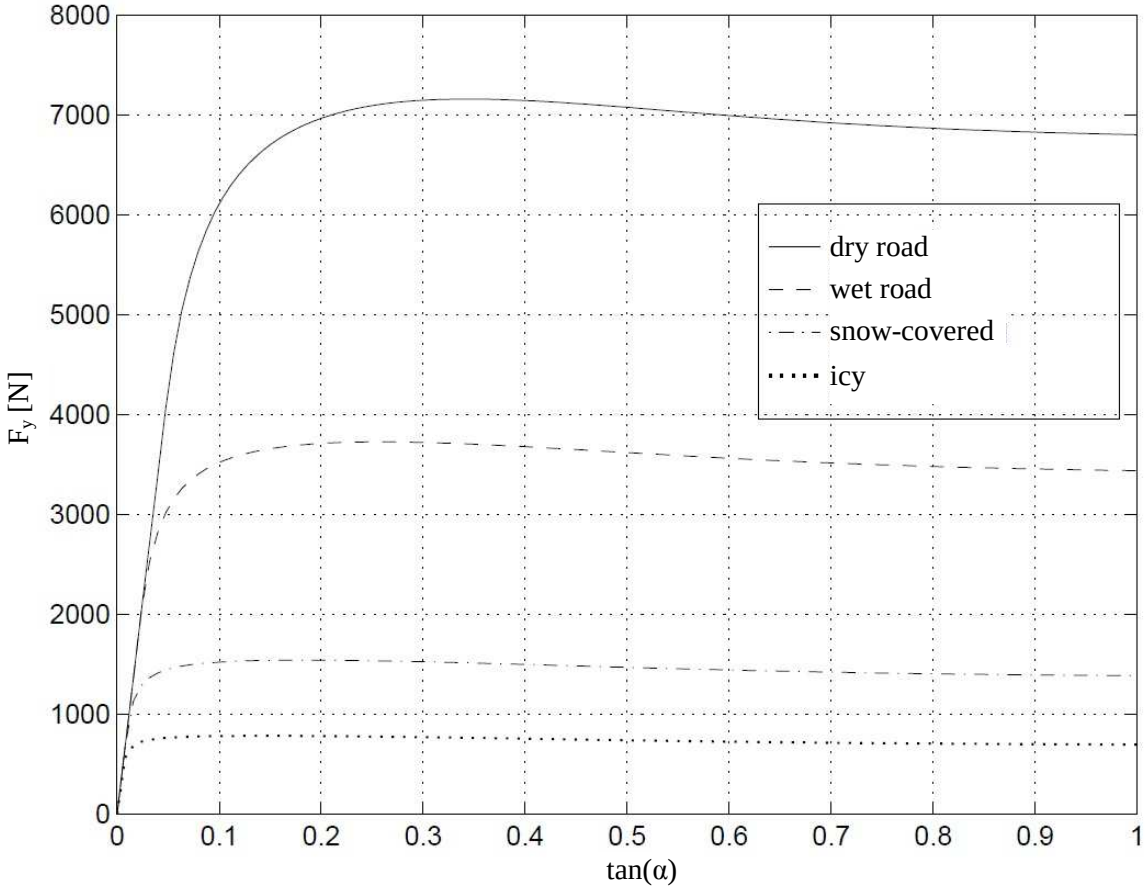

Figure 18. The lateral tyre force relationship to slip angle [68].

At a low slip angle, such as 5° or less, the relationship is linear and can be expressed as

$$F_y = C_\alpha \alpha \,. \tag{4.29}$$

The proportional constant, C_α, is known as the cornering stiffness, which is the slope of the curve of the cornering force versus slip angle α, at α = 0.

The maximum value of the cornering force is determined by the tyre/road adhesion conditions. Several tyre properties have a notable effect on the cornering stiffness:

- Size: a large-size and low-profile tyre has a high cornering stiffness due to the large contact patch area.

- Normal load: an increase in the normal load on the tyre generally increases the cornering stiffness.
- Inflation pressure: a high inflation pressure results in a high cornering stiffness. However, when the tyre pressure reaches a certain high level, the cornering stiffness stays constant.
- Tyre type: generally, radial tyres have a higher cornering stiffness than bias-ply tyres.

Velocity does not significantly affect cornering stiffness of tyres [68]. Also, the surface property has little effect on cornering stiffness. The surface effects have their strongest influence on the peak traction that can be achieved in cornering.

4.2.2.1 Lateral tyre/road friction models

Lateral tyre/road friction models can be classified in two main types: empirical and semi-empirical. As has been mention in section 4.2.1.2, empirical techniques are based on curve-fitting techniques as a linear or non-linear function. The semi-empirical models, however, incorporate, to some extent, the effects of physical tyre parameters into the model.

4.2.2.1.1 Linear proportional model

The simplest form of lateral friction modelling relies on the linear region of the lateral force versus slip angle curve. The lateral force is taken as linearly proportional to the slip angle, in which the proportionality constant is called the cornering stiffness, as in equation (4.29).

The equation is reformulated here

$$\begin{cases} F_{yf} = C_f^{'} \alpha_f \\ F_{yr} = C_r^{''} \alpha_r \end{cases}, \tag{4.30}$$

Where F_{yf} and F_{yr} are the front and rear tyre forces that are perpendicular to the vehicle moving direction, $C_f^{'}$ and $C_r^{''}$ are the front and rear cornering stiffness coefficients and α_f and α_r are the slip angles as defined in Figure 17.

Although it is not very accurate, this model is used in some online estimation cases due to its simplicity [64].

4.2.2.1.2 Nonlinear proportional model

To capture the saturation property of lateral tyre/road friction, several nonlinear models have been proposed. For instance, the nonlinear proportional model in [43] was chosen as

$$F_{yf} = \left[C_f^{''} \frac{C_f^{''2}}{\mu} \frac{C_f^{''3}}{\mu} \right] \cdot \left[|\mathbf{tan\alpha_f}| \frac{-|\mathbf{tan\alpha_f}|^2}{3F_z} \frac{-|\mathbf{tan\alpha_f}|^3}{27F_z^2} \right]^T . \tag{4.31}$$

Nonlinear proportional models can provide more accurate descriptions for the lateral tyre/road friction phenomena and are still easy to identify.

4.2.2.1.3 Magic Formula

Similar to the above mentioned “Magic Formula”, [68] developed another famous formula for the lateral tyre/road friction model. It differs from the above proportional models, it assumes that front tyre force f_f does not only depend on front slip angle α_f, but also on vehicle slide slip angle β, steering angle δ_f, and read slip angle α_r; and so does rear tyre force f_r. Normally, it is written as

$$f_f = D_f \sin\left\{ C_f \tan^{-1}\left(B_f \left[1 - E_f \right] \alpha_f + E_f \tan^{-1}\left(B_f \alpha_f \right) \right) \right\}, \tag{4.32}$$

$$f_r = D_r \sin\left\{ C_r \tan^{-1}\left(B_r \left[1 - E_r \right] \alpha_r + E_r \tan^{-1}\left(B_r \alpha_r \right) \right) \right\}, \tag{4.33}$$

where

$$\begin{cases} \alpha_f = \beta + \tan^{-1}\left(\frac{l_f}{v} r \cdot \cos\beta\right) - \delta_f \\ \alpha_r = \beta - \tan^{-1}\left(\frac{l_f}{v} r \cdot \cos\beta\right) \end{cases}, \tag{4.34}$$

where the coefficients B_j, C_j, D_j, and E_j (j = f, r) in the models are obtained from practical experiments. The "Magic Formula" outperforms the above two kinds of models in modelling accuracy, since it reflects the effect of yaw rate *r* on tyre-force distribution. Moreover, it can be incorporated into the steering model to directly describe the road surface condition. The values of the coefficients, however, require intensive tests on the specified tyre. Such tests are rarely performed on mining vehicle sized tyres and thus the required information is not readily available. The "Magic Formula" model will therefore not be considered in this research.

Table 5. A summary of the mentioned lateral tyre/road friction models.

Model Name	Model Type	Main Features
Linear Proportional Model	Empirical	1. Cannot accurately reflect saturation properties 2. Easy to identify
Nonlinear Proportional Model	Semi-Empirical	Can accurately fit curves
Magic Formula	Semi-Empirical	Can accurately fit curves

4.2.2.2 Combined longitudinal and lateral tyre model

A comprehensive tyre model would include both the longitudinal and lateral tyre dynamics. The tyre model developed by [71], which is shown in Figure 19, is a semi-empirical model which makes use of the proportional models mentioned in both the longitudinal and lateral tyre models.

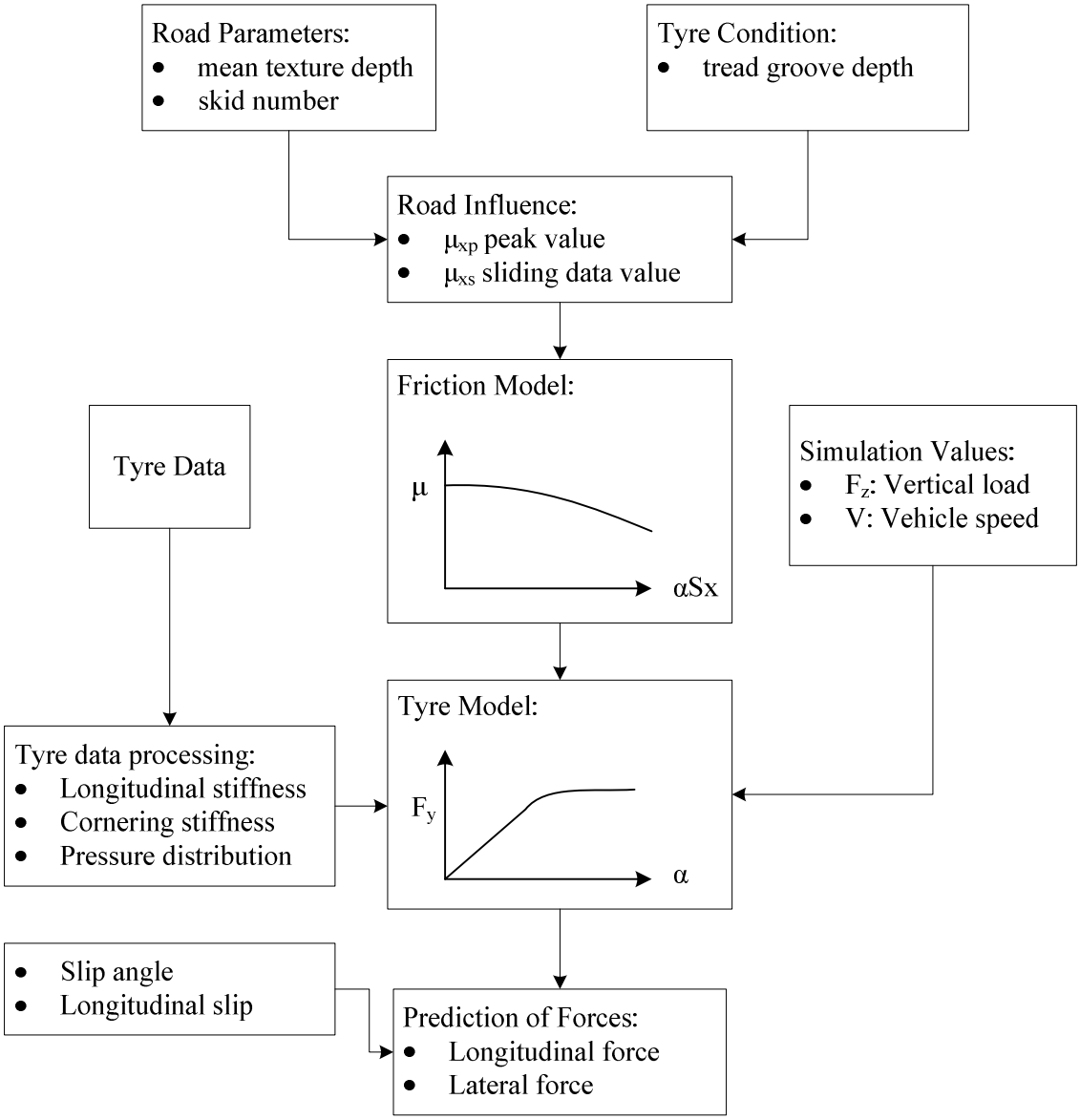

Figure 19. Comprehensive tyre model, adapted from [19], with permission.

The road parameters and tyre condition determine the friction model which is governed by the peak tyre rolling resistance. The tyre data is obtained by offline tests on the vehicle's tyre. The tyre model then incorporates the tyre information with the road conditions while being dependant on the vehicle's speed and vertical load to predict the longitudinal and lateral forces. Including the estimated slip further enhances the accuracy of the predicted tyre forces. The predicted forces are then incorporated into the vehicle model such that the vehicle's response to the forces can be predicted.

4.2.3 Cornering behaviour

The cornering equations may be deduced from the single-track or bicycle model [68]. These equations are derived by application of Newton's second law and are based on the steady-state cornering assumption. Also, it is assumed that the turn radius is much larger than the wheelbase of the vehicle.

The forces in the lateral direction generated by the tyres of the vehicle must equal the mass of the vehicle times the centrifugal acceleration in order for the vehicle to stay on its desired trajectory, when travelling at a specific speed, *v*. This equates to

$$\sum F_y = F_{sf} + F_{sr} = \frac{Mv^2}{R}, \tag{4.35}$$

where the following definitions were made:

F_{sf} = Lateral force at the front axle,
F_{sr} = Lateral force at the rear axle,
R = radius of turn, and
M = mass of the vehicle.

Also, the sum of the moments induced by the front and the rear tyre forces have to equate to zero for the vehicle to be in moment equilibrium, as is shown here:

$$F_{sf} a - F_{sr} b = 0, \tag{4.36}$$

$$\therefore F_{sf} = F_{sr} \frac{b}{a} \tag{4.37}$$

where a is the distance from the front axle to the centre of gravity and b is the distance between the centre of gravity to the rear axle. Combining equations (4.35) and (4.37) as such

$$\frac{Mv^2}{R} = F_{sr}(\frac{b}{a}+1) = F_{sr}(\frac{b}{a}+1) = \frac{F_{sr}L}{a} \tag{4.37}$$

gives

$$F_{sr} = M\frac{av^2}{LR} = \frac{W_r v^2}{gR}, \tag{4.38}$$

where L is the wheelbase, W_r is the mass on the rear axle, g is the gravitational acceleration constant and R is the radius of turn. The lateral force generated by the rear axle may be solved in a similar method. Now, using the piecewise linear tyre model given in 4.2.2.1.1, where it states that $F_s = C'\alpha$ with α being the slip angle and C' the cornering stiffness of the specific tyre, the slip angles are given as

$$\alpha_f = \frac{W_f v^2}{C_f' gR}, \tag{4.39}$$

$$\alpha_r = \frac{W_r v^2}{C_r' gR}. \tag{4.40}$$

The radius of turn was derived from the vehicle's kinematics and is given by

$$R = \frac{v(l_1\cos(\gamma)+l_2)}{v\sin(\gamma)+l_2\dot{\gamma}}, \tag{4.41}$$

where γ is the articulation angle and l_1 and l_2 are the lengths of the front and the rear unit, respectively.

4.2.4 Steering gradient

The steering gradient is an important parameter in the turning response properties of a vehicle [68]. The parameter describes to what extent the lateral acceleration, a_y, influences the turning response and indicates how the turning angle has to be adjusted in order to remain on the desired curved path. It is derived from the relationship between the axle load

on both the front and rear units (W_f and W_r, respectively) and the corresponding cornering stiffness ($C_{\alpha f}$ and $C_{\alpha f}$) of the tyres. Due to the three possible load situations, the understeer ratio can take on three different forms:

- Neutral Steer: $\frac{W_f}{C_{\alpha f}} = \frac{W_r}{C_{\alpha r}}$.

  This situation implies that the front unit slip is equal to the rear unit slip which implies that no change in steering input is required to maintain the wanted curved trajectory, even if the speed is varied.

- Understeer: $\frac{W_f}{C_{\alpha f}} > \frac{W_r}{C_{\alpha r}}$.

  In the case of a LHD, this situation prevails when the load bucket is filled. It implies that the front slip is greater than the rear slip. An increase in speed will cause the front unit's trajectory to overestimate the heading angle and hence the steering angle will need to be increased in order to maintain the desired radius of turn.

- Oversteer: $\frac{W_f}{C_{\alpha f}} < \frac{W_r}{C_{\alpha r}}$.

  If the vehicle experiences oversteer, which, in the case of a LHD, corresponds to an empty load bucket, the rear slip is larger than the front slip. A speed increase during a constant radius turn will necessitate a decrease in the turning angle in order to maintain the radius of turn.

4.2.5 Dynamic LHD models

4.2.5.1 Dynamic model 'A'

The dynamic model of an LHD proposed by [15] is derived from Lagrangian dynamics and, for reference purposes, is named model 'A'. First of all, the general coordinate system governing the vehicle's motion is given in Figure 20.

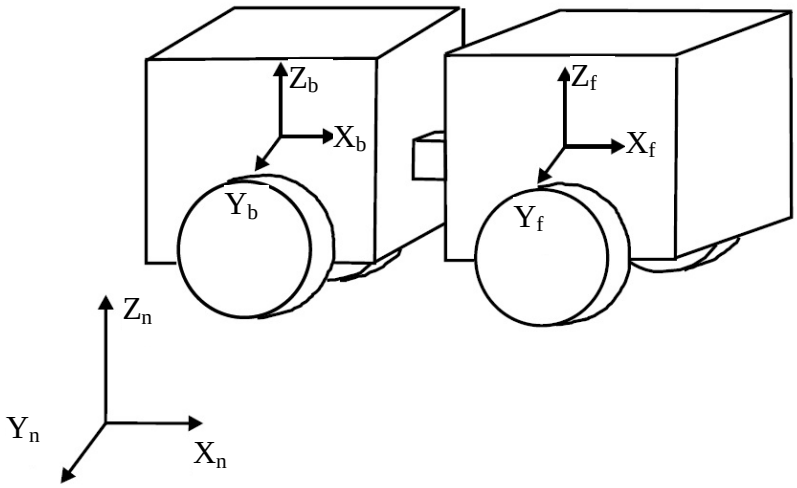

Figure 20. The coordinate system relative to which the LHD's movement is given.

With reference to Figure 20, X_N, Y_N, Z_N is the global coordinate system. The potential and kinetic energy equations, used in the Lagrange method, will be derived according to the global reference frame. X_f, Y_f, Z_f is the coordinate system governing the front unit. The vertical reference frame, Z_f, is positioned in such as way that it passes through the front unit's centre of gravity. Lastly, X_b, Y_b, Z_b is the rear unit's coordinate system. Z_b is placed at the centre of gravity of the rear unit.

The motion of the front unit of the LHD is described by the relative motion of the X_f, Y_f, Z_f coordinate system with respect to the global X_N, Y_N, Z_N coordinate system. The rear unit, in turn, is then referenced to the front unit's coordinate system by the articulation angle. Implementing the above reference system, the following set of variables describes the vehicle's motion:

x_n : position of front unit's center of gravity (C.G.) in x-direction on inertial coordinates

$\dot{x}_n$: velocity of front unit's C.G. in x-direction on inertial coordinates

y_n : position of front unit's C.G. in y-direction on inertial coordinates

$\dot{z}_n$: position of front unit's C.G. in z-direction on inertial coordinates

ε_1 : front unit's yaw angle with respect to inertial coordinate system

$\dot{\varepsilon}_1$: front unit's yaw rate with respect to inertial coordinate system

γ_f : articulation angle between front and rear unit of LHD

$\dot{\gamma}_f$: rate of articulation angle between front and rear unit of LHD

In order to apply the Lagrange equation, the vehicle's kinematic and potential energies need to be determined. To achieve this, the rotational and translational velocities have to be determined.

4.2.5.1.1 Centre of gravity

Before the centre of gravity can be calculated, the dynamic axle loads of the LHD vehicle need to be determined. It also gives an indication of the tractive effort obtainable from each axle which affects acceleration, braking and the cornering characteristics of the vehicle's tyres [68]. Figure 21 indicates the position of the traction forces on the LHD vehicle when subjected to a specific incline of an angle σ.

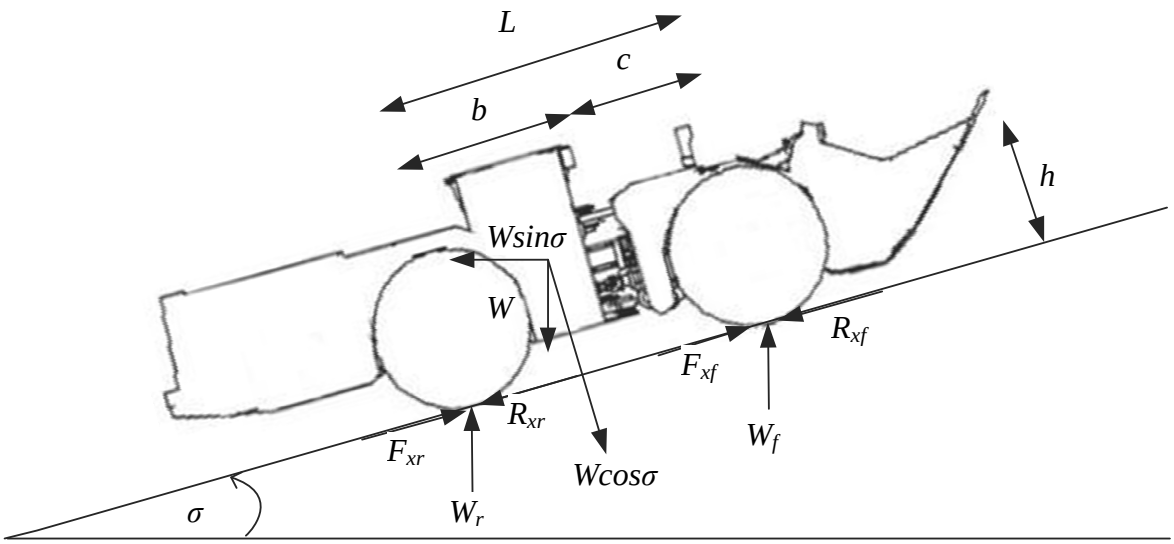

Figure 21. The traction forces on the LHD vehicle.

With reference to Figure 21 the following forces are of importance:

W: the weight of the vehicle expressed in its mass multiplied by the gravitational constant. On an incline, both a horizontal and vertical component of this weight is present.

Normal tyre forces: W_f and W_r denote the vertical forces exerted on the front and the rear tyres, respectively.

Tractive forces: F_{xf} and F_{xr} are the forces exerted on the tyres in the direction of forward motion on the ground plane.

Rolling resistance forces: R_{xf} and R_{xr} are the forces exerted on the tyres in the direction opposite of forward motion on the ground plane.

The load on either the front or the rear axle can now be expressed by the above definitions. The loads are defined by two components, a static and a dynamic load. The dynamic load results from the weight shifting to and fro from either side of the vehicle. The load on the front axle can be computed by summing the torques about the rear tyre. Similarly, the load on the rear axle can be computed by summing the torques about the front tyre. The result is as follows:

$$W_f = \frac{(Wc\cos\sigma - \frac{W}{g}a_x h - Wh\sin\sigma)}{L}, \tag{4.42}$$

$$W_r = \frac{(Wb\cos\sigma - \frac{W}{g}a_x h - Wh\sin\sigma)}{L}. \tag{4.43}$$

The reference point for the coordinate system explained above is at the centre of gravity of both the front and the rear unit. Figure 22 shows the approximate positions of the centre of gravities where a is the distance from the front centre of gravity to the articulation joint and b is the distance from the rear centre of gravity to the articulation joint. W_f and W_r are the weight on the front and the rear axle, respectively.

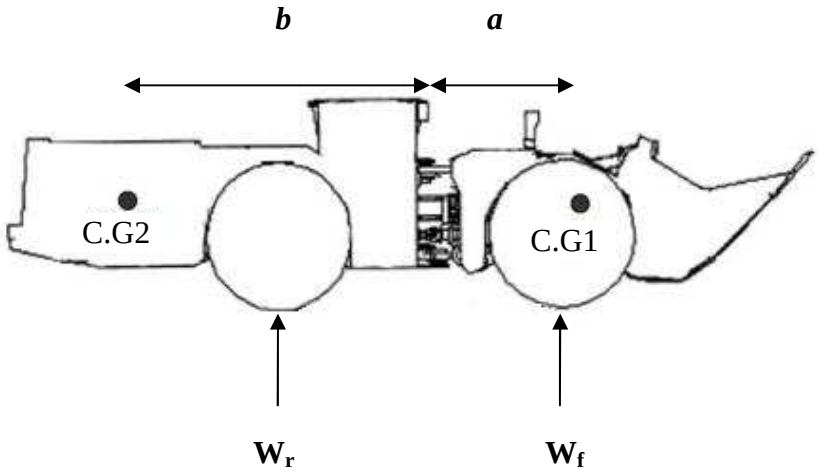

Figure 22. The centre of gravity calculations are derived from this figure.

In order to obtain the values of *a* and *b*, the moments about the articulation joint is equated to zero as follows:

$$W_r b - W_f a = 0, \tag{4.44}$$

hence

$$\frac{b}{a} = \frac{W_f}{W_r}. \tag{4.44}$$

Further, it is assumed that the centre of gravity lies within the wheelbase (L) of the LHD, which justifies the conclusion that $a = L - b$. Substituting this expression into equation (4.44) results in

$$b = \frac{\frac{W_f}{W_r} L}{1 + \frac{W_f}{W_r}}. \tag{4.45}$$

Figure 23 displays and Table 6 defines and describes all of the included parameters.

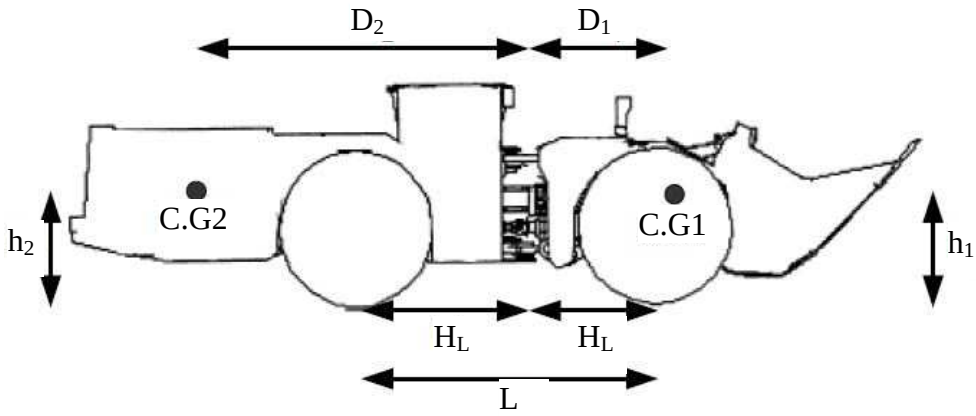

Figure 23. Schematic diagram of LHD parameters used in the dynamic model derivation, from [15].

Table 6. Parameters of the vehicle model.

Parameter	Description
m_1	Mass of front unit
I_{x1}, I_{y1}, I_{z1}	Front unit moment of inertia
m_2	Mass of rear unit
I_{x2}, I_{y2}, I_{z2}	Rear unit moment of inertia
T_{w1}	Track width of front axle
T_{w2}	Track width of rear axle
$C_{\alpha f}$	Front tyre cornering stiffness
$C_{\alpha r}$	Rear tyre cornering stiffness
H_L	Distance from axle to articulation joint
L	Vehicle wheelbase
h_1, h_2	Heights of centre of gravity (CG)
D_1, D_2	Distance from joint to CG
d_1, d_2	Vertical distance from joint to CG

4.2.5.1.2 Euler-Lagrange equations

The Euler-Lagrange equations describe the evolution of a mechanical system subject to holonomic constraints. In order to determine these equations, one has to form the

Lagrangian of the system, which is the difference between the kinetic energy and the potential energy [15].

In terms of the unit vector (***i**n, **j**n, **k**n*), the velocity of the front unit with respect to the global coordinate system is given as

$$\begin{aligned} V_{CG1/n} &= \dot{x}_n i_n + \dot{y}_n j_n + 0 \\ &= \left(\dot{x}_n \cos\varepsilon_1 + \dot{y}_n \sin\varepsilon_1\right) i_f + \left(-\dot{x}_n \sin\varepsilon_1 + \dot{y}_n \cos\varepsilon_1\right) j_f, \end{aligned} \tag{4.46}$$

whereas the velocity of the rear unit with respect to the global coordinate system is given as

$$\begin{aligned} V_{CG2/n} &= V_{CG1/n} - D_1 \frac{d}{dt} i_f - d_1 \frac{d}{dt} k_f - D_2 \frac{d}{dt} i_r - d_2 \frac{d}{dt} k_r \\ &= V_{CG1/n} - D_1 \varepsilon_1 j_f - D_2 \left(\dot{\varepsilon}_1 + \dot{\varepsilon}_f\right) j_r, \end{aligned} \tag{4.47}$$

with the Lagrangian defined as follows

$$L = T_1 + T_2 + P_E, \tag{4.48}$$

where T_1 is the kinetic energy of the front unit, T_2 the kinetic energy of the rear unit and P_E the potential energy of the vehicle; the various energy equations need to be found. First of all, the potential energy, P_E, is derived from the roll motion experienced by the LHD. However, due to the limited amount of suspension travel and the heavy loads carried by the LHD, [15] assumed that the effects of roll motion may be neglected. The potential energy is therefore not included in the Lagrangian since

$$P_E = 0. \tag{4.49}$$

Equation (4.48) now becomes

$$L = T_1 + T_2, \tag{4.50}$$

with

$$\begin{aligned} T_1 &= \frac{1}{2} m_1 {V_{CG1}}^2 + \frac{1}{2} \omega_f I_1 \omega_f \\ &= \frac{1}{2} m_1 \left(\dot{x}_n \cos\varepsilon_1 + \dot{y}_n \sin\varepsilon_1 \right)^2 + \frac{1}{2} m_1 \left(-\dot{x}_n \sin\varepsilon_1 + \dot{y}_n \cos\varepsilon_1 \right)^2 + \frac{1}{2} I_{z1} \dot{\varepsilon}_1^{\,2}, \end{aligned} \tag{4.51}$$

and

$$\begin{aligned} T_2 &= \frac{1}{2} m_1 {V_{CG2}}^2 + \frac{1}{2} \omega_r I_2 \omega_r \\ &= \frac{1}{2} m_2 \left(\dot{x}_n \cos\varepsilon_1 + \dot{y}_n \sin\varepsilon_1 \right)^2 + \frac{1}{2} m_1 \left(-\dot{x}_n \sin\varepsilon_1 + \dot{y}_n \cos\varepsilon_1 \right)^2 \\ &\quad + \frac{1}{2} m_2 \left(-D_1 \dot{\varepsilon}_1 - D_2 \left(\dot{\varepsilon}_1 + \dot{\varepsilon}_f \right) \right)^2 - m_2 \sin\varepsilon_f \left(\dot{x}_n \cos\varepsilon_1 + \dot{y}_n \sin\varepsilon_1 \right) \cdot D_2 \left(\dot{\varepsilon}_1 + \dot{\varepsilon}_f \right) \\ &\quad + m_2 \cos\varepsilon_f \left(-\dot{x}_n \sin\varepsilon_1 + \dot{y}_n \cos\varepsilon_1 - D_1 \dot{\varepsilon}_1 \right) - D_1 \left(\dot{\varepsilon}_1 + \dot{\varepsilon}_f \right) + \frac{1}{2} I_{z1} \left(\dot{\varepsilon}_1 + \dot{\varepsilon}_f \right)^2. \end{aligned} \tag{4.52}$$

From the Lagrange equations the following dynamic equations defining the generalized forces are derived:

$$\frac{d}{dt} \frac{\partial L}{\partial \dot{x}_n} - \frac{\partial L}{\partial x_n} = F_{gx_n}, \tag{4.53}$$

$$\frac{d}{dt} \frac{\partial L}{\partial \dot{y}_n} - \frac{\partial L}{\partial \dot{y}_n} = F_{gy_n}, \tag{4.54}$$

$$\frac{d}{dt} \frac{\partial L}{\partial \dot{\varepsilon}_1} - \frac{\partial L}{\partial \varepsilon_1} = F_{g\varepsilon_1}, \tag{4.55}$$

$$\frac{d}{dt} \frac{\partial L}{\partial \dot{\varepsilon}_f} - \frac{\partial L}{\partial \varepsilon_f} = F_{g\varepsilon_f}, \tag{4.56}$$

Where F_{gxn}, F_{gyn}, $F_{g\varepsilon 1}$ and $F_{g\varepsilon f}$ are the generalized forces generated at the tyres. The generalized forces are calculated from the forces generated as a result of the tyre/road interface as shown in Figure 24.

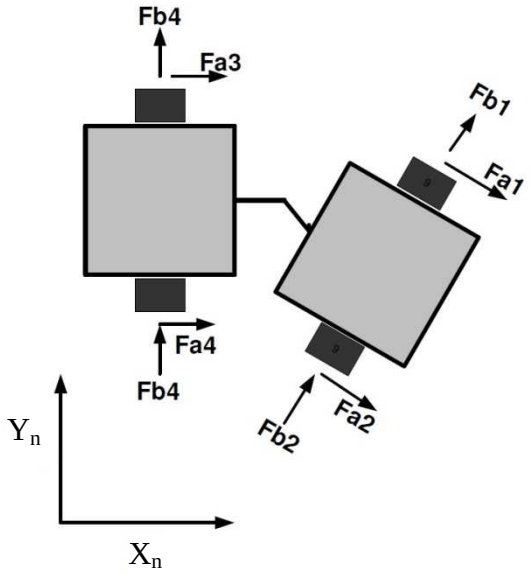

Figure 24.The generalized forces acting on the tyres, adapted from [19], with permission.

[15] shows that combining equations (4.53), (4.54), (4.55) and (4.56) with the expressions derived from the generalized forces yields the following state-space equation:

$$\left(\ddot{\mathbf{q}}\right) = -\mathbf{M}^{-1}\mathbf{h}\left(\mathbf{q},\dot{\mathbf{q}}\right) + \mathbf{M}^{-1}\mathbf{F}_g, \tag{4.57}$$

where

$$\mathbf{q} = \begin{pmatrix} x \\ y \\ \varepsilon_1 \\ \varepsilon_f \end{pmatrix}, \tag{4.58}$$

while **M** is the inertia matrix and $\mathbf{F_g}$ represents the generalized forces acting on the wheels as shown in Figure 24.

The forces shown in Figure 24 are determined by a tyre model. The semi-empirical tyre model implemented in this specific dynamic vehicle model is depicted in Figure 19.

4.2.5.2 Dynamic model 'B'

A similar approach, but where the generalized forces are derived from the kinematic constraints on the wheels, is given by [14]. The kinematic constraints are incorporated in the Lagrange equations in a similar manner as it is done for nonholonomic constraints. This leads to the expressions of the side forces generated by the slipping of the wheels. Due to the similarity to model 'A', the lengthy derivation of the model 'B' will not be given here.

4.2.5.3 Decoupling vehicle dynamics from kinematic control

A technique whereby both the kinematic and the dynamic properties of the vehicle are incorporated in a navigation and control problem is presented by [1] and [72]. The kinematic model, based on the model presented in section 4.1.2, is used to predict the vehicle's pose as part of a path-tracking controller implemented to reduce vehicle position errors within a localization framework. The modelled dynamics of the vehicle are decoupled and distinctly controlled in such a way that both angular and longitudinal velocities are reliably and robustly regulated according to the specified references from the path-tracking controller. The introduction of sufficient bandwidth separation between the path-tracking controller and the regulator of the vehicle's dynamics contributes to the efficient operation of the path-tracker [1]. More information regarding such a path-tracking solution is given in section 6.2.2.

4.3 CHAPTER SUMMARY

Both kinematic and dynamic modelling of the articulated vehicle was discussed in this chapter. A number of tyre models, which form an intricate part of the dynamic model, have also been named. The simplicity of the kinematic model makes it an attractive choice for localization and control purposes. On the other hand, the potential accuracy of the dynamic model is a good platform from which the vehicle's handling can be intricately studied.

CHAPTER 5

FIELD TEST AND MODEL SIMULATIONS

This chapter firstly gives an insight into the field vehicle test procedure after which the results are compared with the known kinematic models. Simulations were performed to evaluate the various available kinematic models and some of their underlying assumptions. Also, a simulation of a dynamic model is given.

5.1 TEST PROCEDURE

In order capture field test data, two test sessions were executed on articulated vehicles. The first such test was done on a Wright 365B LHD, a commonly implemented LHD in the South African mining industry. Figure 25 to Figure 27 are photos taken of the LHD on which the tests were completed.

5.1.1 LHD test

Due to the short availability of the LHD, the main aim of the test was to gather insight into the daily implementation of such a vehicle in the mining environment. The LHD was made available by the Anglo Coal Colliery in Kriel, South Africa. The dusty and dirty state the LHD was in illustrated the harsh working conditions the driver has to endure, daily. Furthermore, in order to save space, the driver's sitting position is such that he faces the steering wheel which, in turn, is placed perpendicular to the vehicle's heading. This implies that the driver has to twist his upper body to face the direction in which the vehicle is moving. To observe the driver's point of view, refer to Figure 26. In addition, the space in which the driver has to operate is designed to be as small as possible, further worsening the ergonomics. The cabin is shown in Figure 27. According to the driver, the stiff wheel suspension in conjunction with the limited sprung seat often leads to back pain after a lengthy shift.

Figure 25. The Wright 365B LHD on which the tests were performed.

Figure 26. The driver's point of view.

Figure 27. The driver's cabin, which is laid out perpendicular to the vehicle's heading.

In order to capture data on the performance of the LHD, it was equipped with a VBOX II GPS system. The VBOX II system is a GPS data logging system from Racelogic. The specifications of the VBOX II system are given in the following table:

Table 7. The VBOX II specifications.

Parameter	**Specification**
Velocity	
Accuracy	0.2 km/h
Resolution	0.01 km/h
Absolute Positioning	
Accuracy with DGPS	< 1.8 m
Resolution	1 cm
Heading	
Accuracy	0.01 º
Resolution	0.2 º

Parameter	Specification
Acceleration	
Accuracy	1%
Resolution	0.01 G
Distance	
Accuracy	0.05 % (< 50 cm / km)
Resolution	1 cm
Time	
Accuracy	0.05 s
Resolution	0.01 s

The VBOX II GPS system captures the data at a rate of 20 Hz.

Although the tests were performed on an asphalt surface, similar results were expected on an underground mining surface due to the fact that the LHD travels at a fairly low speed.

In order to accurately simulate the LHD's trajectory, the main tests were to determine the acceleration, deceleration and maximum operating speed of such a vehicle. Figure 28 shows the maximum speed test result. The maximum acceleration achieved was 1.85 m/s^2. The time taken to reach a top speed of around 2.8 m/s or 10 km/h was just over 5 s. The maximum deceleration was measured to be 8.5 m/s^2.

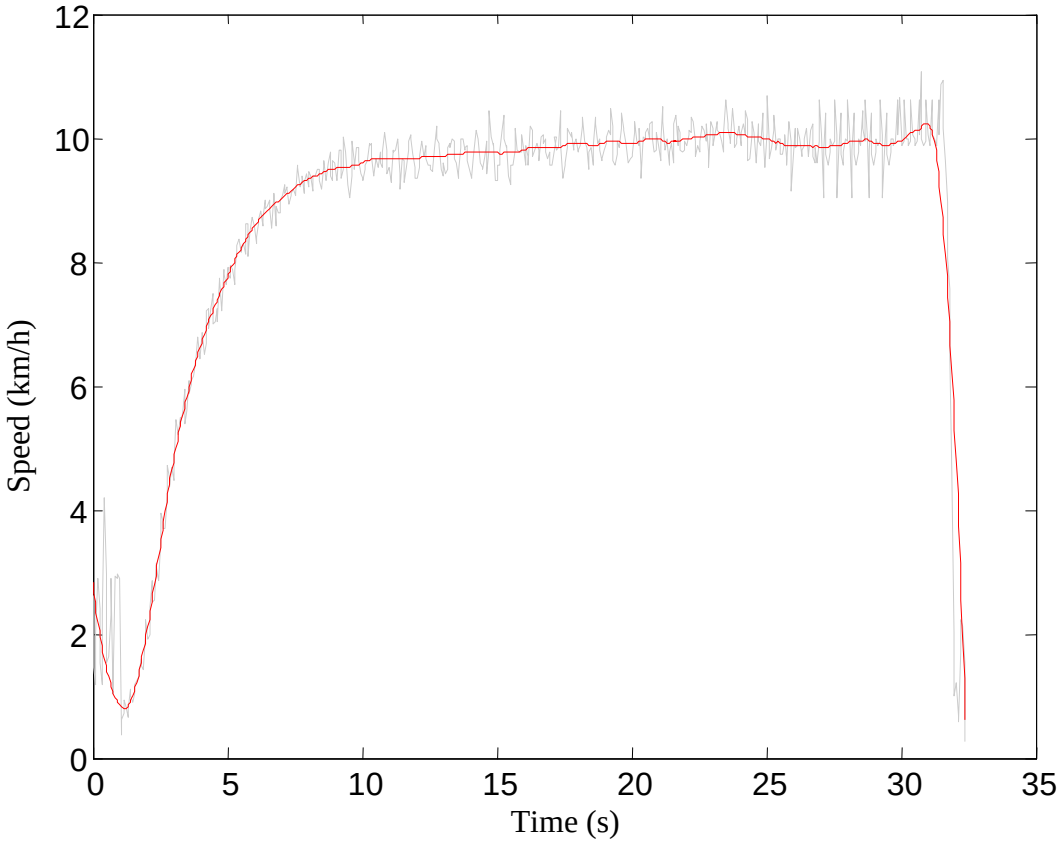

Figure 28. The maximum acceleration, speed and deceleration of the Wright LHD.

With reference to Figure 28, the light grey graph represents the raw data obtained from the GPS velocity measurement while the red line is the smoothed version of the original data. The smoothed data was obtained by making use of the locally weighted scatter plot smoothing method, using least squares quadratic polynomial fitting, averaging 300 data points at a time.

From this test it becomes obvious why researchers tend to ignore most of the dynamic forces involved during motion. The maximum operating speed is seldom above 10 km/h which substantiates and verifies some of the fundamental assumptions made during kinematic modelling.

5.1.2 Articulated loader test

The second, more thorough test was performed on a Bell L1606C articulated loader. Although the loader is not an underground mining vehicle, its kinematic behaviour is comparable to the LHD vehicle since its wheelbase and the individual unit lengths are similar to those of the Wright LHD. A photo of the loader is shown in Figure 29.

Figure 29. The Bell L1706C articulated loader.

The sensor suit which was employed is listed here:

- VBOX II GPS system
- 2 accelerometers,
- gyrometer and
- rope displacement sensor.

The two accelerometers were attached to the front and rear axle in order to sense the lateral acceleration at the axles. The following table summarizes the specification of the identical accelerometers.

Table 8. The accelerometer specifications.

Parameter	Specification
Range	-2 < G < 2
Sensitivity	833 to ± 67 mV / G
Noise Density	20 µG / √Hz
Zero G Drift Over Temperature	170 µV / ºC

The high stability, low noise and suitable measurement range were considered as the main factors when choosing the appropriate accelerometer. The temperature drift was also deemed as an important parameter because the field tests were to be performed in direct sunlight.

The gyrometer senses the vehicle's yaw, roll and pitch. Only the yaw rate was recorded because its integral would give an indication on the vehicle's heading. The following table summarizes the specification of the yaw sensor.

Table 9. Gyrometer specifications.

Parameter	Specification
Range	-180<°<180
Sensitivity	7mV / ° / s
Noise Density	0.06 ° / s / √Hz

Lastly, the rope displacement sensor was installed to measure the articulation angle. The sensor was calibrated in such a way that the fully extended hydraulic cylinder matched the top end of the sensor's measurement range.

The VBOX system, specified in Table 7, records the following information from its GPS measurements:

- number of active satellites
- time,
- latitude,

- longitude,
- velocity,
- heading and
- altitude.

All the sensors, other than the VBOX system, had their output recorded at a sufficiently high rate of 100Hz using a 16 bit data acquisition device, called eDAQ. Figure 30 shows the placement of the gyrometer box, close to the centre of gravity of the front unit. Figure 31 shows the placement of the rope displacement sensor. The extension of the hydraulic steering cylinder was measured in order to derive the articulation angle.

Figure 30. The gyrometer placement.

Figure 31. Placement of the rope displacement sensor.

The venue for this test was a barren field on the outskirts of Pretoria East, near a sand quarry. Figure 32 displays the field on which the tests were performed. The desired paths were laid out by cones.

Figure 32. The venue of the articulated loader test.

As Figure 32 shows, the test was performed on a solid gravel surface, similar to surfaces found in the underground mines. A number of tests were performed to assess both the vehicle's kinematic and dynamic properties. Each test was repeated with a full dirt load. The following lists the tests that were done:

- Straight line,
- constant radius with steady-state turning,
- lane change,
- slalom and
- a laid-out circuit.

The purpose of the straight line test was to determine the loader's maximum acceleration and deceleration. The results were similar to those of the LHD. Since the top speed of such a loader is far in excess of that of a LHD vehicle, testing it was superfluous. The straight-line test speed result of the empty loader is shown in Figure 33. The graph given in Figure 33 is a smoothed representation of the original data. The result of the test with a full dirt load was similar. Maximum acceleration was around 1.86 m/s^2 while the maximum deceleration was measured to be about 2.5 m/s^2. When compared to the equivalent test results of the Wright LHD, depicted in Figure 28, the acceleration is similar but the braking effort by the LHD is far better. This is due to the fundamental design of the LHD braking system which is specifically designed (for safety reasons) to bring the vehicle to an abrupt stop.

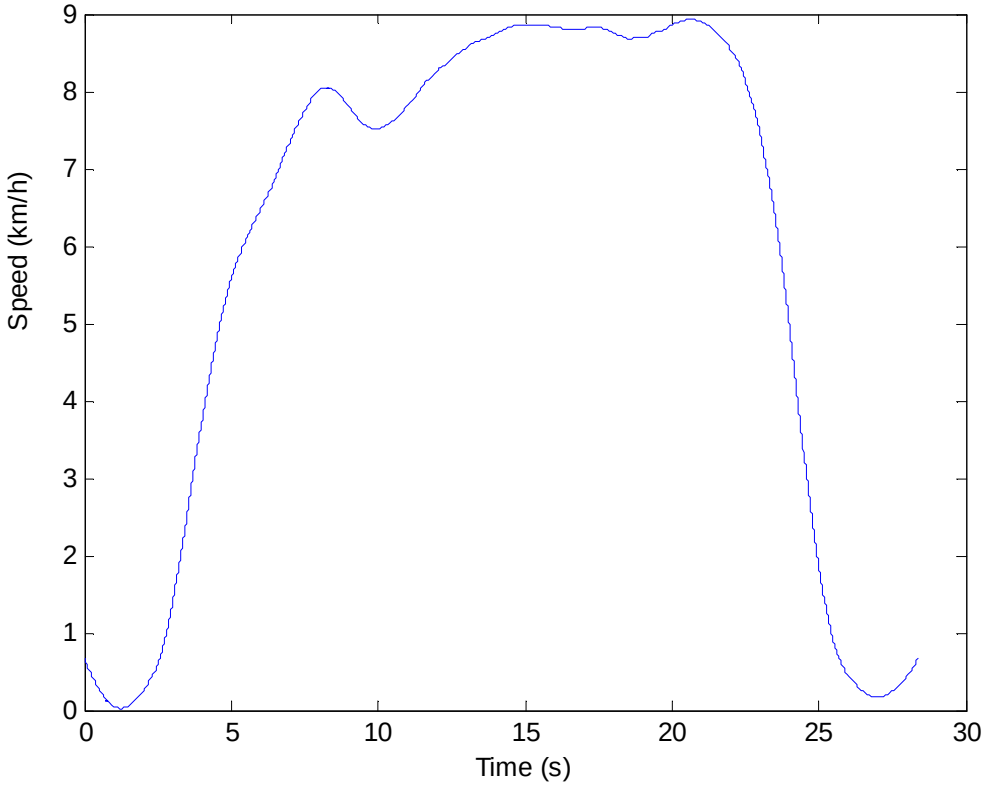

Figure 33. Straight-line acceleration and deceleration of the articulated loader.

The constant radius test was performed in order to determine the tyres' understeer gradient, from which their cornering stiffness can be determined. The understeer gradient is an important property of a vehicle's turning response characteristics, as was explained in Chapter 4. This property determines how the steering angle of the vehicle must be changed with the radius of the turn or the lateral acceleration in order to remain on the same curved trajectory. The vehicle was driven in a constant radius while its steering angle and lateral acceleration were recorded. The procedure was to drive the vehicle in a circular trajectory of constant radius at a very low speed at which the lateral acceleration is negligible, and note the steering angle required to maintain the turn. While attempting to drive along the same trajectory, the speed is increased and the steering angle noted at each speed. The steering angle is then plotted as a function of the lateral acceleration. In order to obtain the understeer gradient, the derivative of the function is taken. A run of the constant radius test on an empty loader is plotted in Figure 34. The starting point was at the x-y coordinate position (0;0).

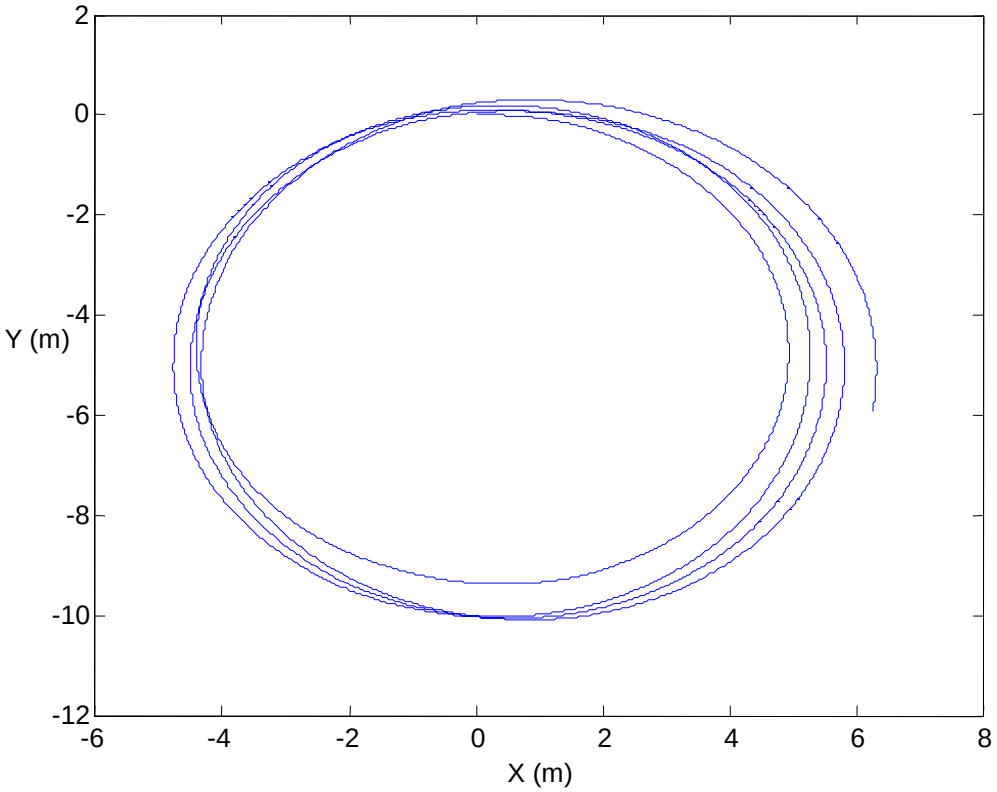

Figure 34. The trajectory of a constant radius test run.

The corresponding speed is given in Figure 35 and the raw articulation angle in Figure 36. The steering angle had to be decreased in order to maintain the same trajectory. This indicates that the understeer gradient, as was expected, is negative. As the speed increased, so did the lateral acceleration of both the front and the rear unit, as is depicted in Figure 37.

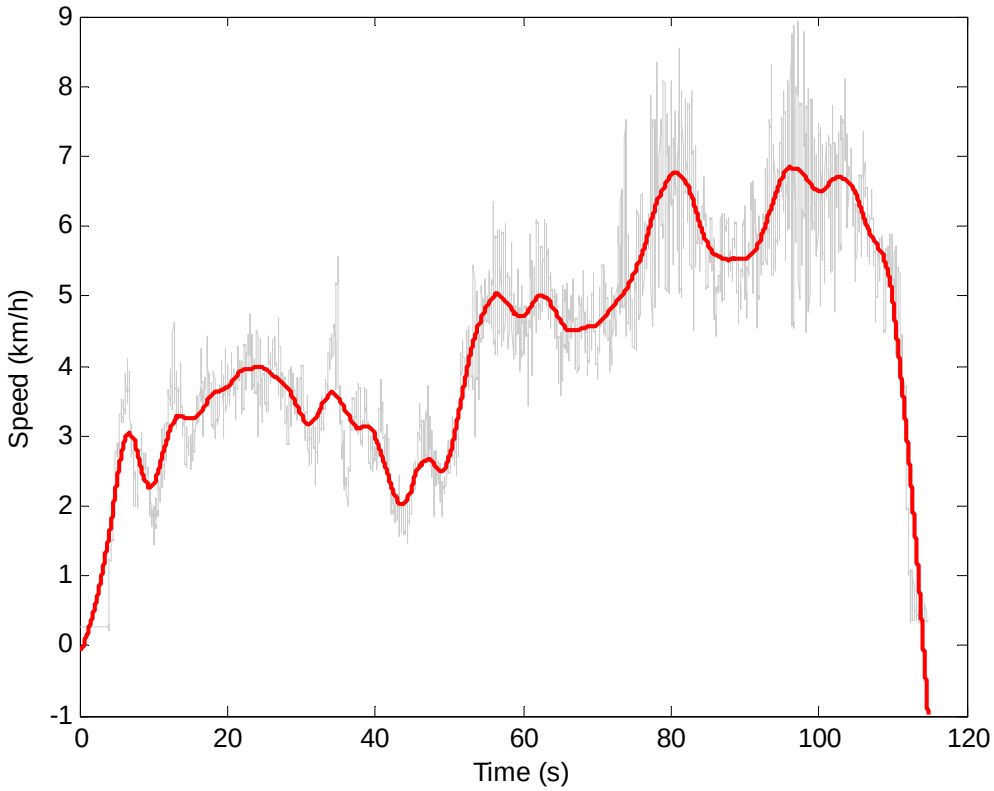

Figure 35. The speed of the constant radius test.

With reference to Figure 35, the light grey trajectory represents the original GPS velocity measurement while the red line represents the smoothed version of the original data. The inherent noise is mainly as a result of the constant change of the GPS satellite lock.

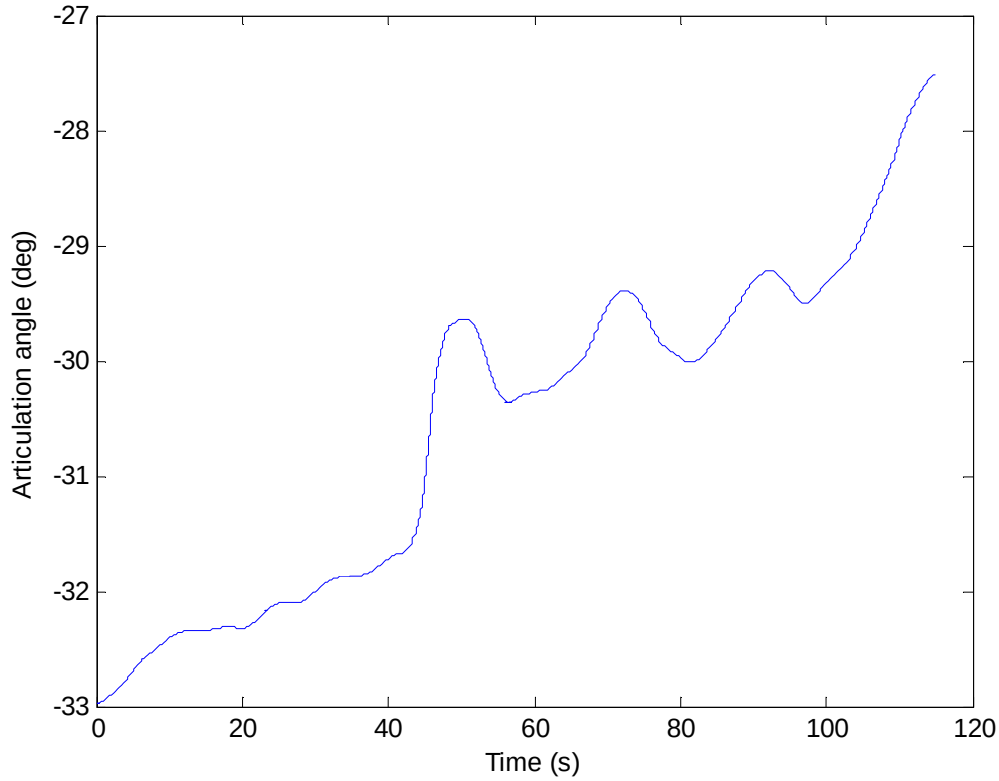

Figure 36. The articulation angle during the constant radius test.

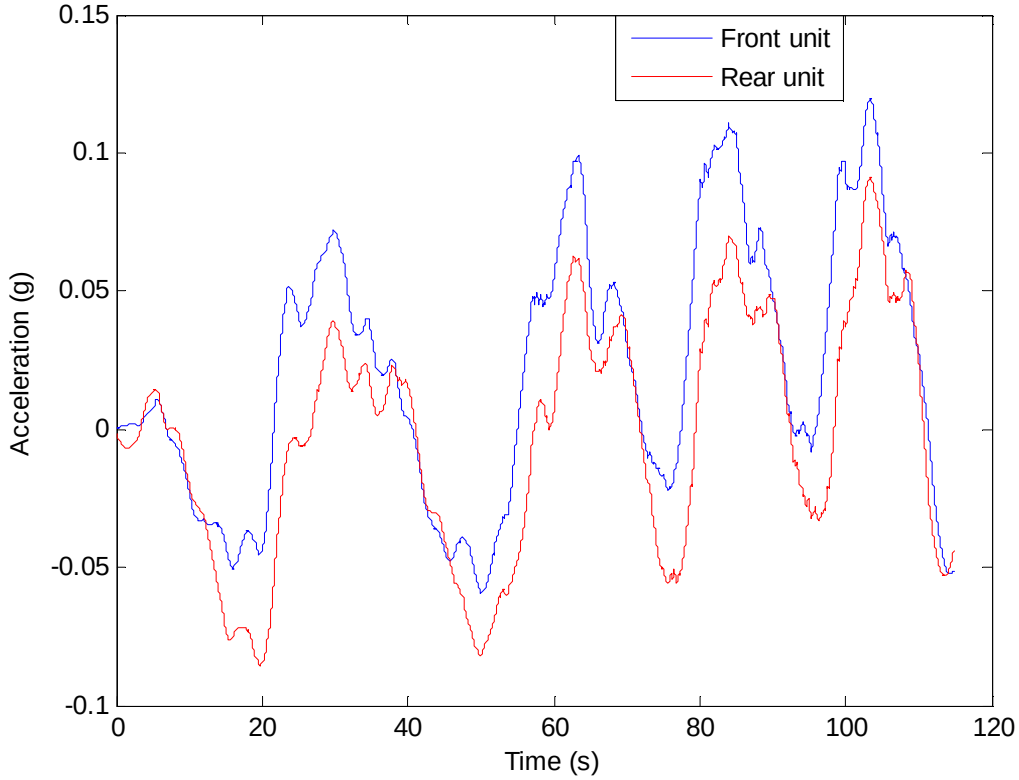

Figure 37. The lateral acceleration of both the front and the rear units.

Both the lane change and the slalom test were performed in order to observe the vehicle's response to rapid articulation angle changes.

Lastly, a circuit was laid out to mimic a possible path in the underground mine. The circuit included straight paths, sharp intersections and a slow turn. Chapter 6 uses this test data for the LHD localization and control implementation. Figure 38 displays the circuit layout. It contains a long straight, sharp right and left turns and a long right turn.

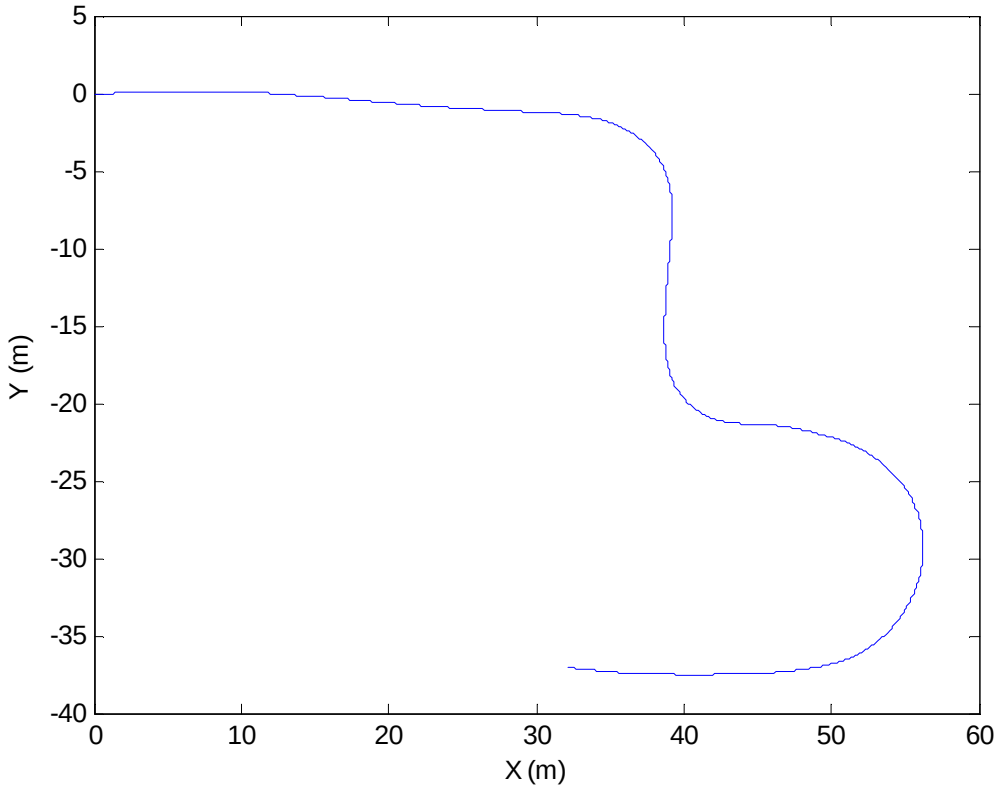

Figure 38. The circuit trajectory.

5.2 KINEMATIC MODEL

The following time-dependent kinematic model was used as the basis model from which the simulations where performed:

$$\dot{x} = V\cos(\phi) \tag{5.1}$$

$$\dot{y} = V\sin(\phi) \tag{5.2}$$

$$\dot{\phi} = \frac{-V\sin(\gamma) - l_2\dot{\gamma}}{l_1\cos(\gamma) + l_2} \tag{5.3}$$

The inputs to the model are the front unit's velocity, V, and the articulation angle, γ. Both were measured during the real test runs which enabled the evaluation of the model's performance. The test data trajectories used throughout this chapter refer to the GPS data captured during the various test runs.

5.2.1 Assumptions

The two most prominent assumptions generally made in literature concerning the kinematic modelling of LHD vehicles is the no-slip condition and the assumption that the length of the front unit is equal to the length of the rear unit. These assumptions were investigated and their influence on the kinematic model was noted.

5.2.1.1 Half-length assumption

The kinematic model given by [56], which was discussed in Chapter 4, assumes that the vehicle's articulation joint is at its half-length. The heading is then represented as

$$\dot{\phi} = \frac{V\sin(\gamma) - \frac{L}{2}\dot{\gamma}}{\frac{L}{2}\cos(\gamma) + \frac{L}{2}}, \tag{5.4}$$

where L is the length of the wheelbase of the LHD. Taking the dimensions of a commonly used Wright LHD 356B model, the wheelbase is given as 3080mm. However, the length of the front unit is about 10 cm shorter than the rear unit. In order to observe the effect of this

erroneous front unit length assumption, simulations have been done to compare the various state trajectories at various front unit lengths. The length of the rear unit was kept constant at 1.6 m while the length of the front unit was systematically incremented by 10 cm. Also, the articulation angle and the vehicle's velocity were kept constant. The trajectories given in the following simulations represent the following front unit lengths: A = 1.4 m, B = 1.5 m, C = 1.6 m, D = 1.7 m and E = 1.8 m. Figure 39 gives the circular path trajectory chosen for this simulation.

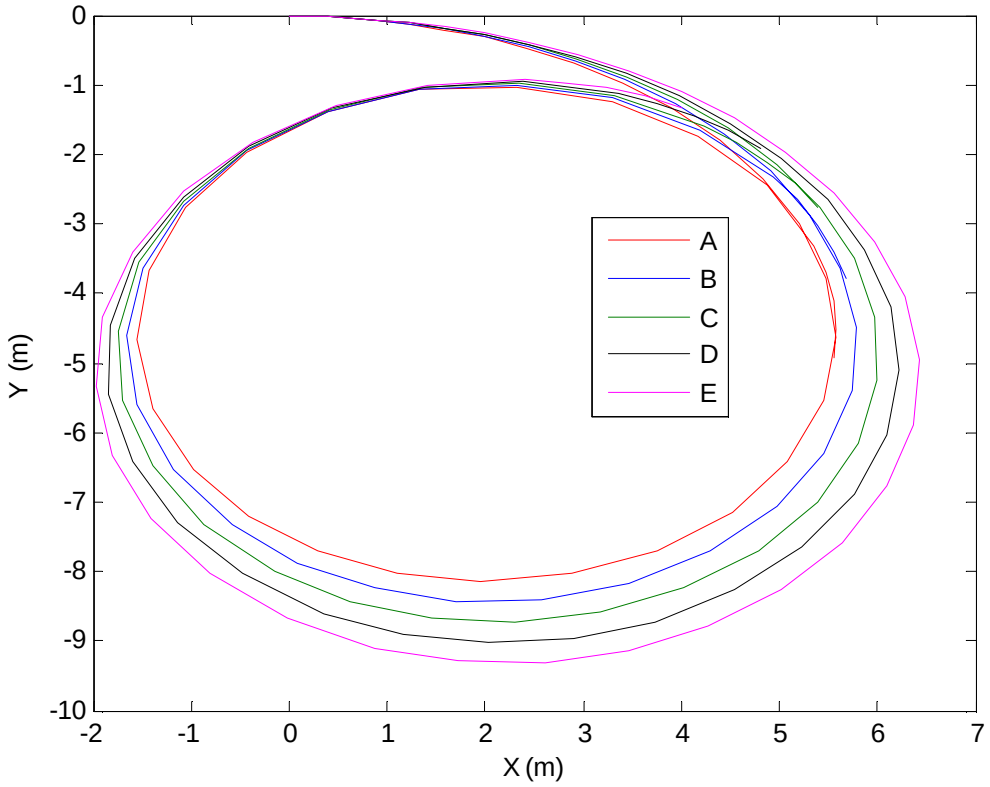

Figure 39. The comparison of the vehicle's path trajectory with various front-unit lengths.

With reference to Figure 39, the model underestimates the turning radius if the front unit's length is too short. Trajectory B is approximately the front unit length of the Wright LHD and when compared to the half-length assumption of path C, path C clearly overestimates the turning radius. For arguments sake, paths D and E indicate that while the articulation angle is kept constant at a non-zero value, the turning radius constantly increases with constant front unit length increases.

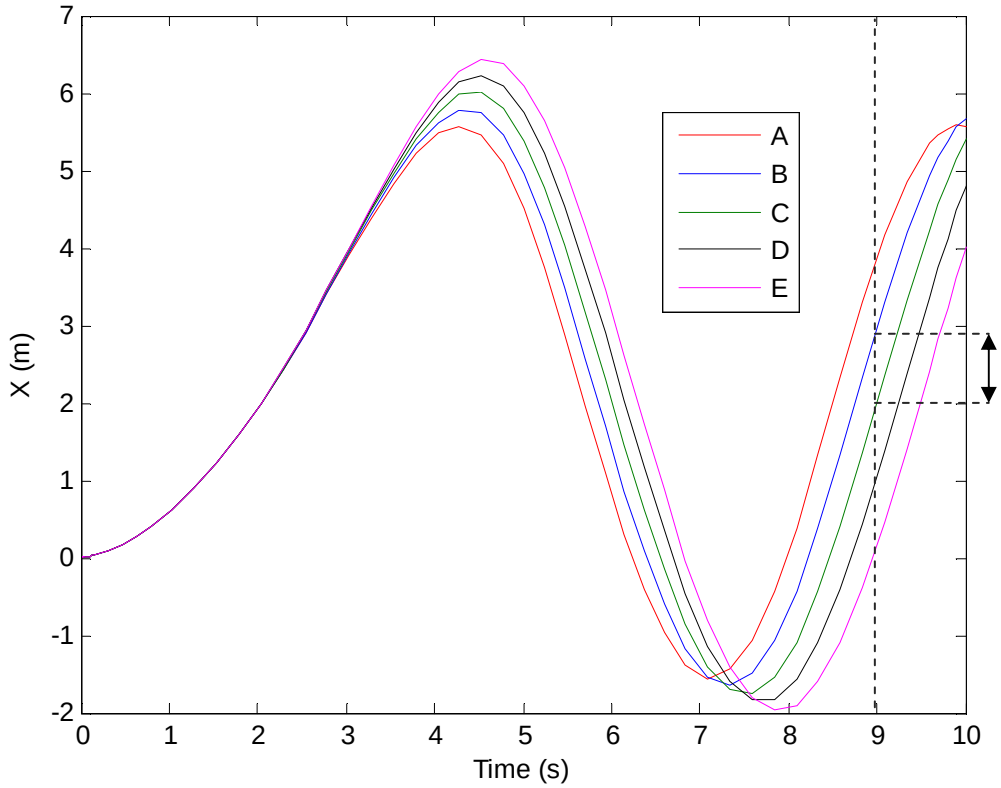

Figure 40. Comparison of the vehicle's X-direction trajectory with various front-unit lengths.

Figure 40 shows the comparison of the *x*-state trajectories. Taking the ninth second as a reference, the error between path B and C is already approaching 1m. When the articulation angle is non-zero, the error will accumulate.

Similar to Figure 40, Figure 41 shows how the error in the *y*-state trajectory increases over time.

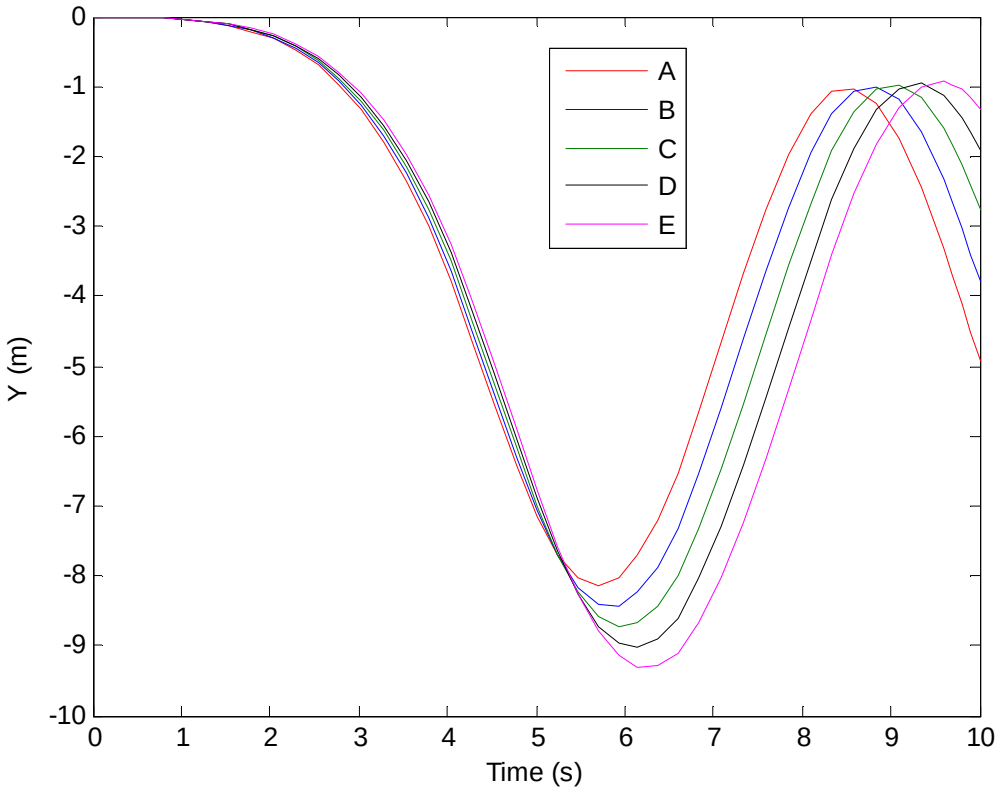

Figure 41. Comparison of the vehicle's Y-direction trajectory with various front-unit lengths.

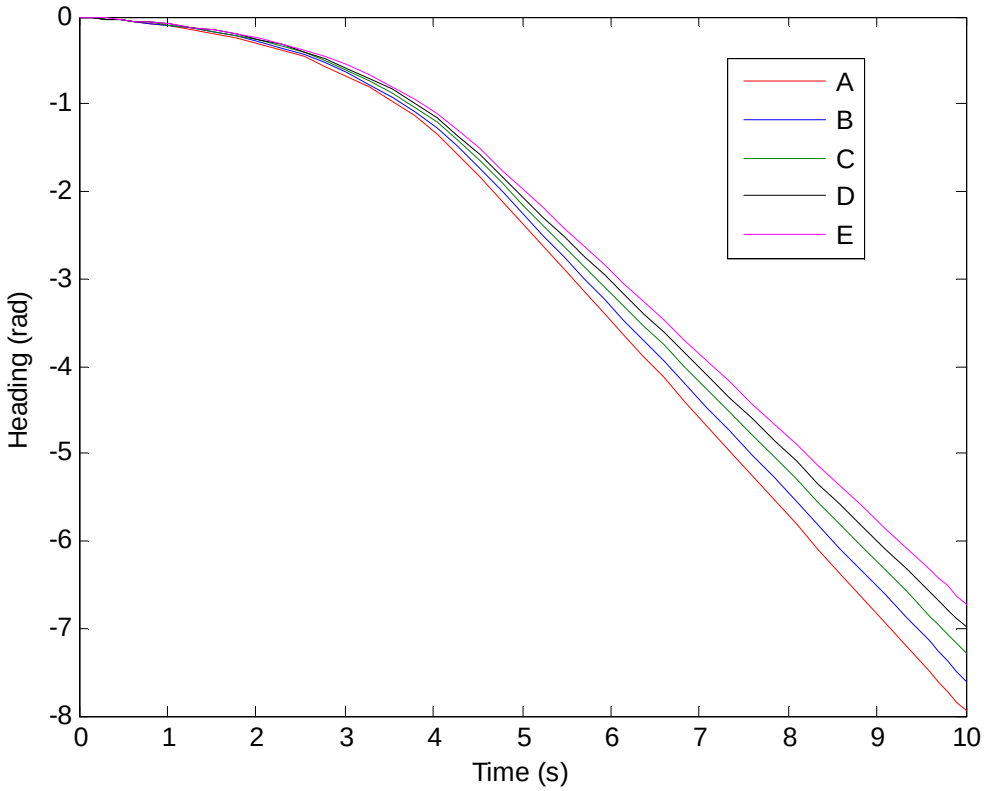

Figure 42. Comparison of the vehicle's heading with various front-unit lengths.

Figure 42 shows the heading of the vehicle at the various front unit lengths over time. Again, the error accumulates over time. Also, is it important to keep in mind that the off-tracking error will be non-zero if the units are not of equal length. Equation (2.4) gives the off-tracking error.

5.2.1.1.1 Discussion

Without any further analysis, it may be concluded that unequal LHD unit lengths do have a notable influence on the kinematic model's predictions. Although the error induced by the equal half-length assumption may be reduced by implementing robust path tracking control, introducing two distinct unit lengths into the model, as in equation (5.3), does not substantially complicate the model.

5.2.1.2 No slip assumption.

Firstly, the performances of the slip- and no-slip models were evaluated. In Chapter 4, the LHD vehicle slip factor was discussed. To start off with, the no-slip kinematic model, given in equations (5.1) to (5.3), was compared to the test data.

As has been mentioned, the side-slip angle has to be present if the articulation is not constant or zero. Hence, if a side-slip angle is present at the front unit, the turning radius of the front unit will be larger than in the case when no slip is present. To illustrate this, the driver of the articulated loader drove a constant circle by making sure that the turning angle was kept constant, i.e. steady-state turning.

With reference to Figure 43, the blue path represents the GPS data captured by the VBOX system while the red trajectory is the no-slip kinematic model's x versus y state output. The results show that the turning radius of the loader is just below 9m while the corresponding turning radius predicted by the model is about 8m. Figure 44 and Figure 45 give the x and the y state trajectories, respectively. Both figures substantiate the fact that the no-slip model underestimates the vehicle's turning angle. Figure 46 shows the vehicle heading over time. The rate of change of the heading of the no-slip kinematic model (red line) is high when compared to the test data.

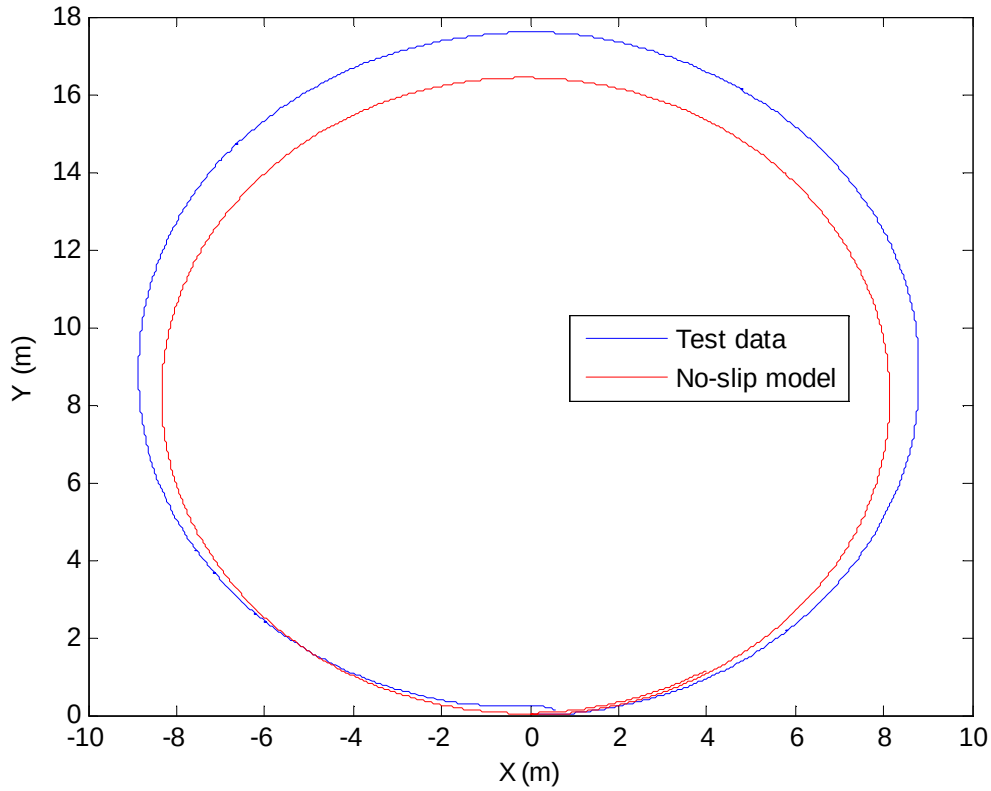

Figure 43. Circular trajectory to show the amount of slip.

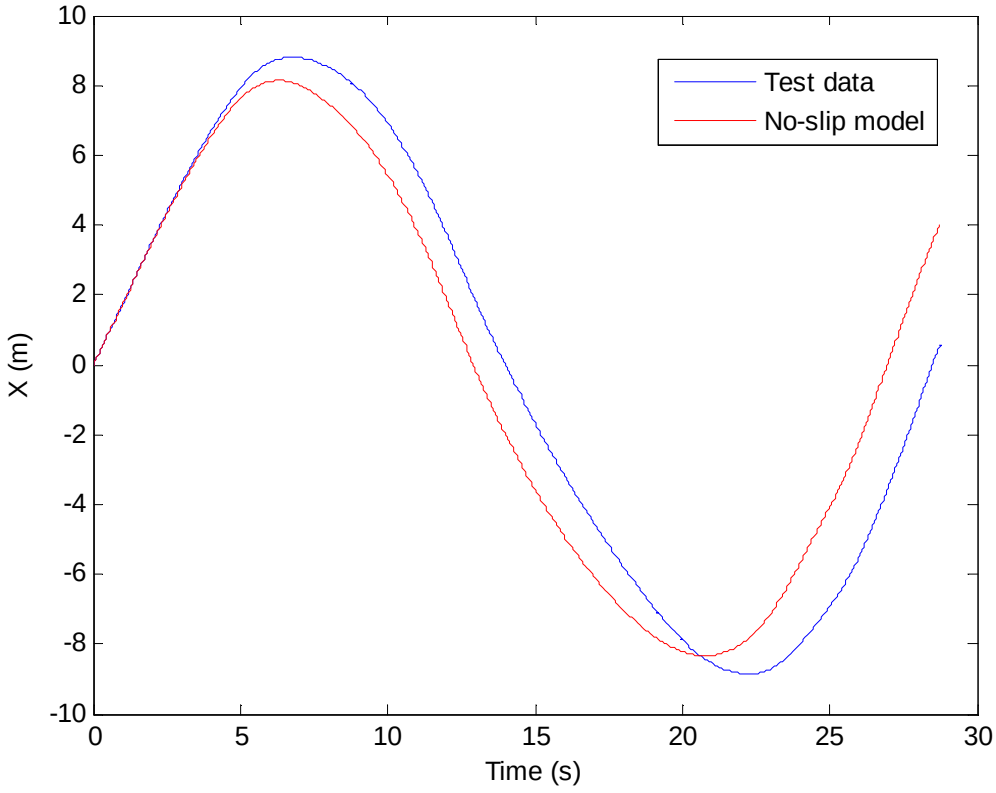

Figure 44. The *x* state trajectory of the path shown in Figure 43.

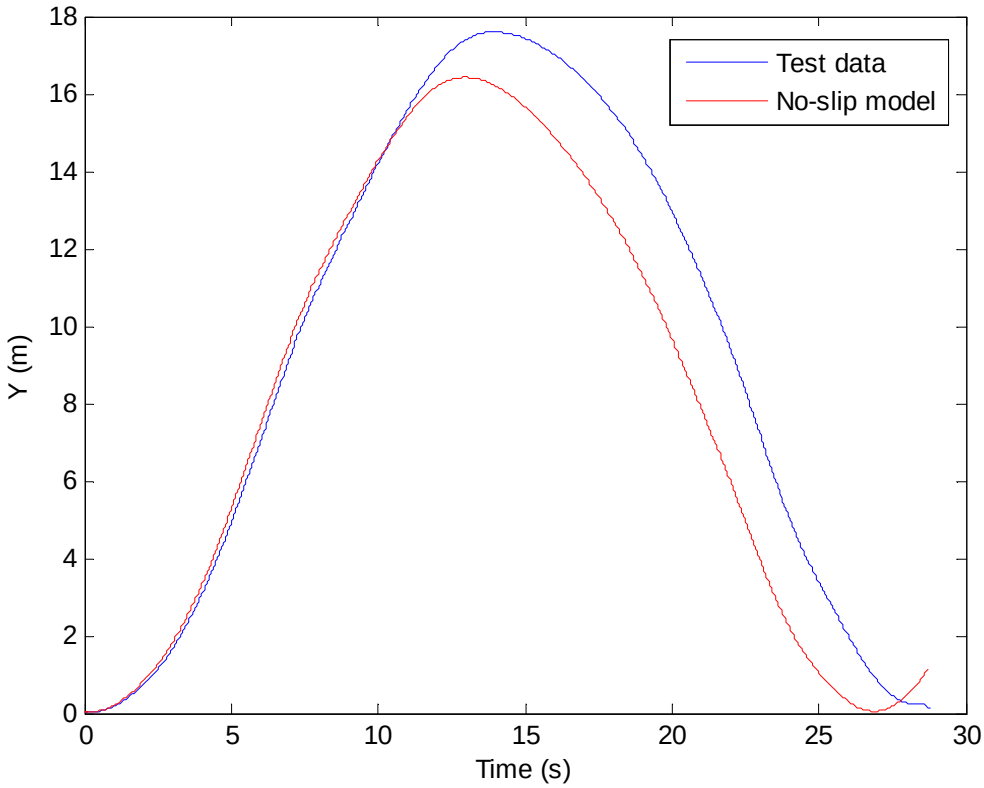

Figure 45. The *y* state trajectory of the path shown in Figure 43.

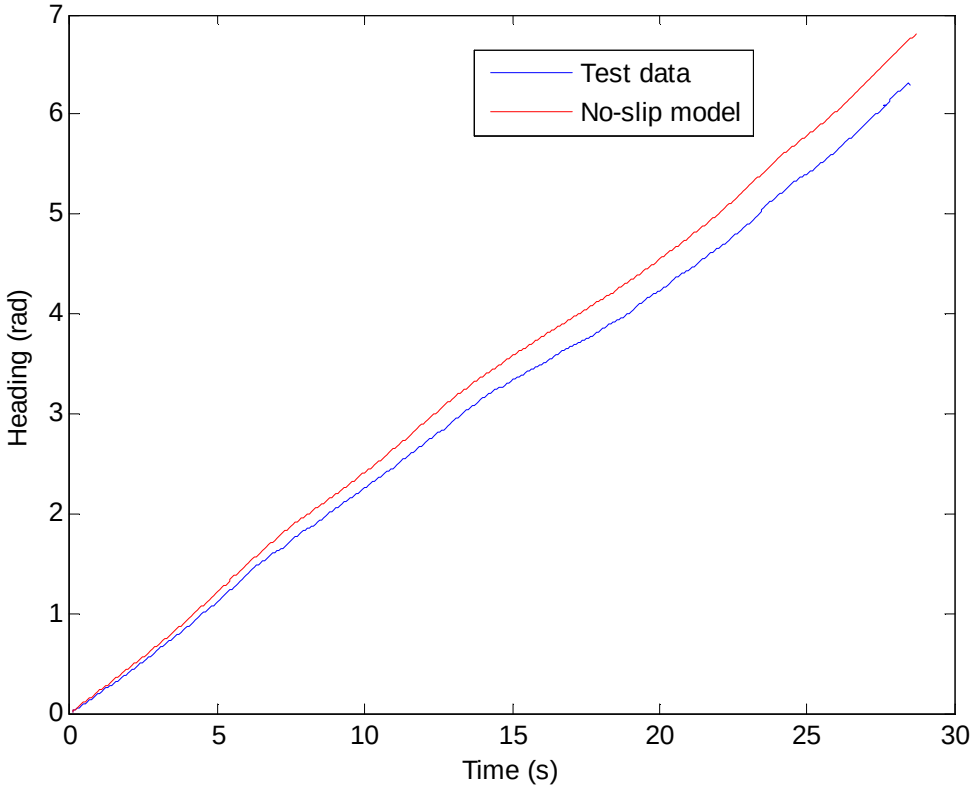

Figure 46. The heading trajectory of the path shown in Figure 43.

The inclusion of a slip factor, which in effect decreases the rate of change of the heading, should improve the accuracy of the kinematic model prediction. The basic model of equations (5.1) to (5.3) is now written as the following system:

$$\begin{aligned}\dot{x} &= V\cos(\alpha+\phi)\\ \dot{y} &= V\sin(\alpha+\phi)\\ \dot{\phi} &= \frac{-V\sin(\beta-\alpha+\gamma)-l_2\dot{\gamma}\cos(\beta)}{l_1\cos(\beta+\gamma)+l_2\cos(\beta)},\end{aligned} \tag{5.5}$$

where α and β are the front and the rear slip angles, respectively. This system has also been discussed in Chapter 4 where it was mentioned that various methods exists to predict the slip angles. A novel approach would be to directly include the involved turning forces into the kinematic framework. These turning forces will be estimated by a simple dynamic tyre model such as the piecewise linear model. The amount of slip can be estimated by equations (4.39) and (4.40). In the case of an empty load, the weight on the front and rear axles is estimated at 4800kg and 8400kg, respectively.

In order to use the model, the tyre's cornering stiffness and the lateral force exerted on the tyre are required. Figure 47 shows the side slip force versus the slip angle graph of a 16x20 sized truck tyre [60], carrying a vertical load of 2.4 tons. Since the tyres used on the loader are similar and should present similar characteristics, the graph was used in the tyre model.

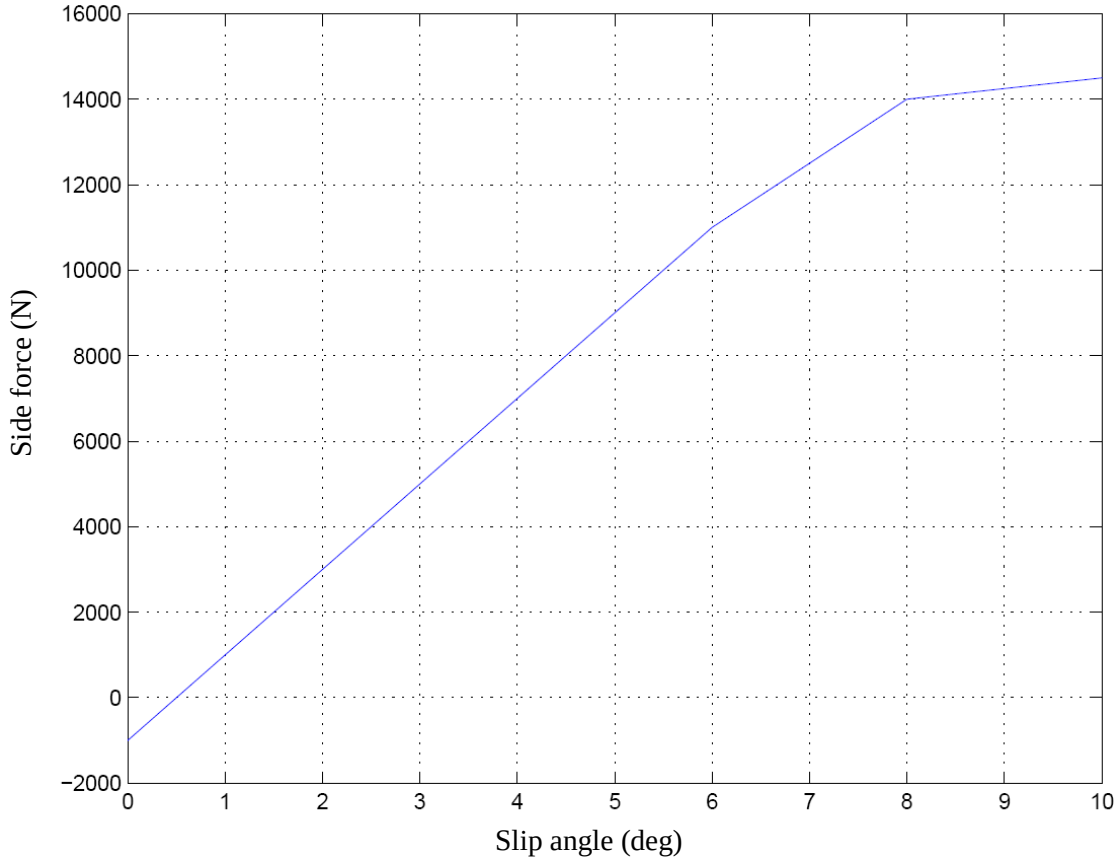

Figure 47. The side force *vs*. the slip angle graph used to calculate the cornering stiffness.

From the data gathered by the accelerometers on the axles throughout the test runs, it was found that the side force never exceeded 5000 N, even during vigorous turns; hence the cornering stiffness, which is taken as the gradient calculated from Figure 47, was taken as 2000 N/deg or 114590 N/rad.

The above simulations were repeated with the tyre model added to the kinematic model. Figure 48 compares the blue GPS trajectory to the red kinematic model's *x*-state versus its *y*-state output. The model predicts the actual trajectory fairly accurately, with never having a root mean square offset error larger than 3m. To illustrate the improvement, the time-specific position error of the no-slip model is compared to that of the slip model in Figure 49. However, it is important to keep in mind that the tyre model is based on steady-state turning and may not be as accurate in situations where the articulation angle varies. Figure 50 and Figure 51 compare the *x* and the *y* state trajectories, respectively.

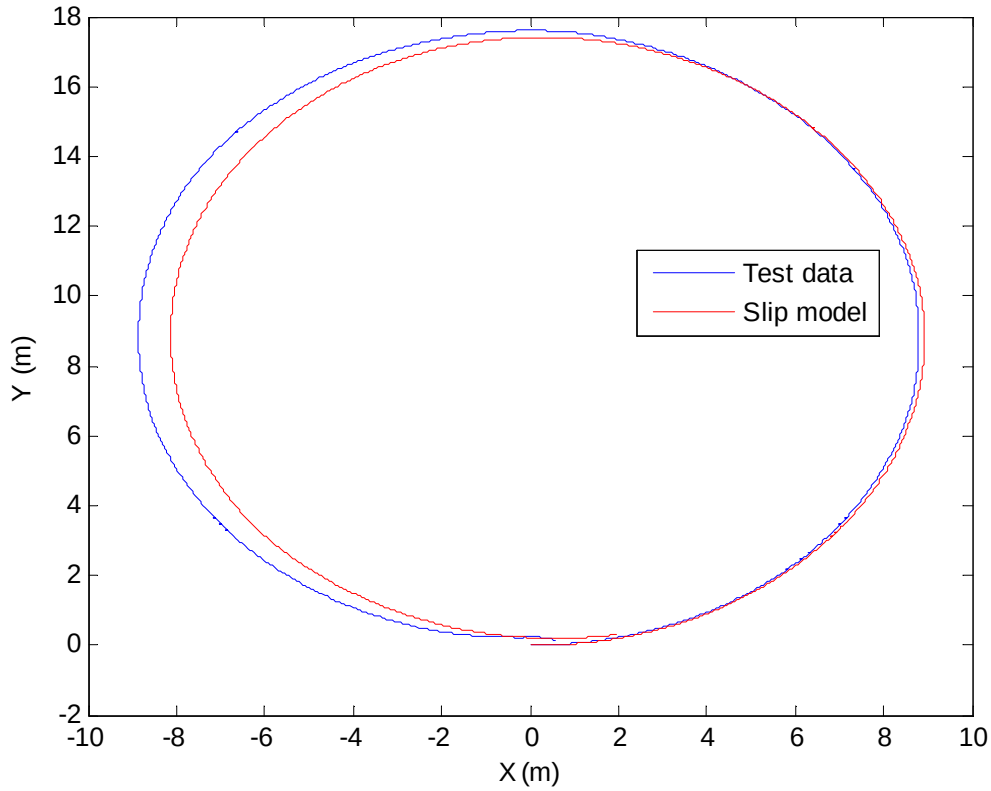

Figure 48. The circular path simulated with the inclusion of the tyre model.

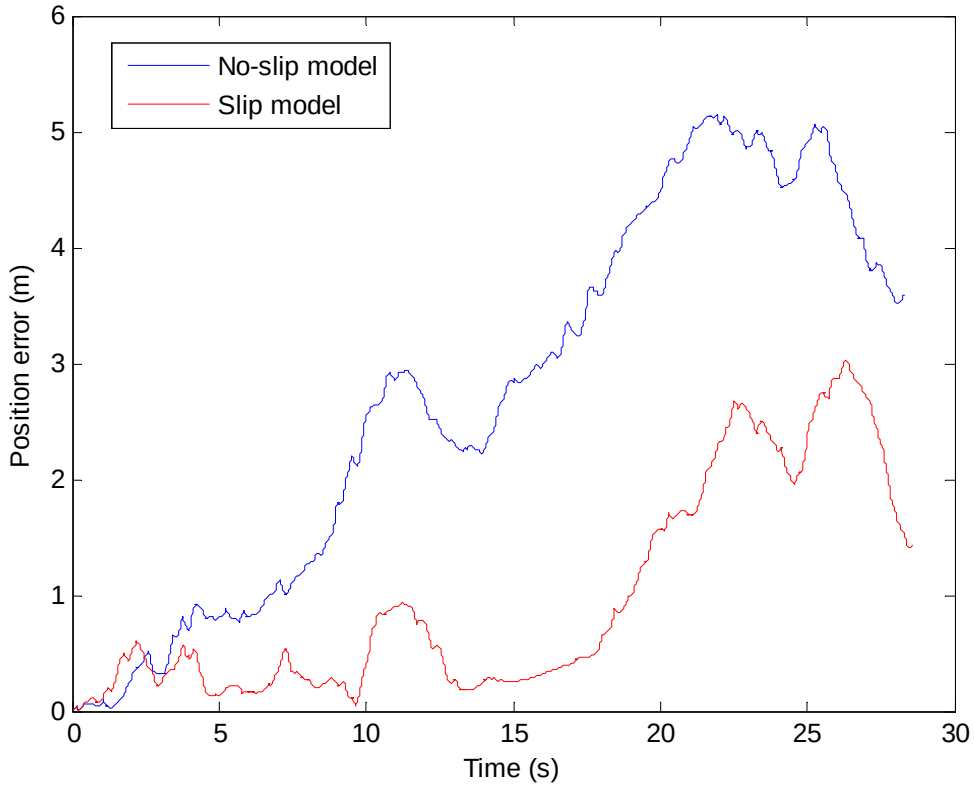

Figure 49. The position error comparison between the slip and no-slip models.

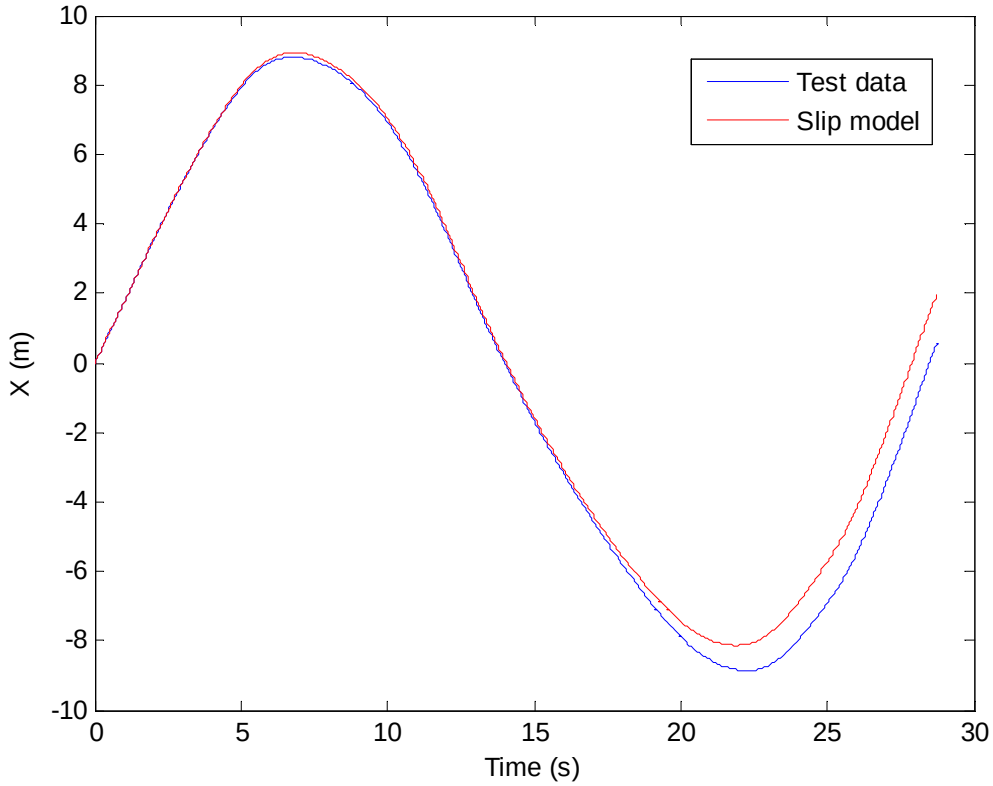

Figure 50. The *x* state trajectory of the path shown in Figure 48.

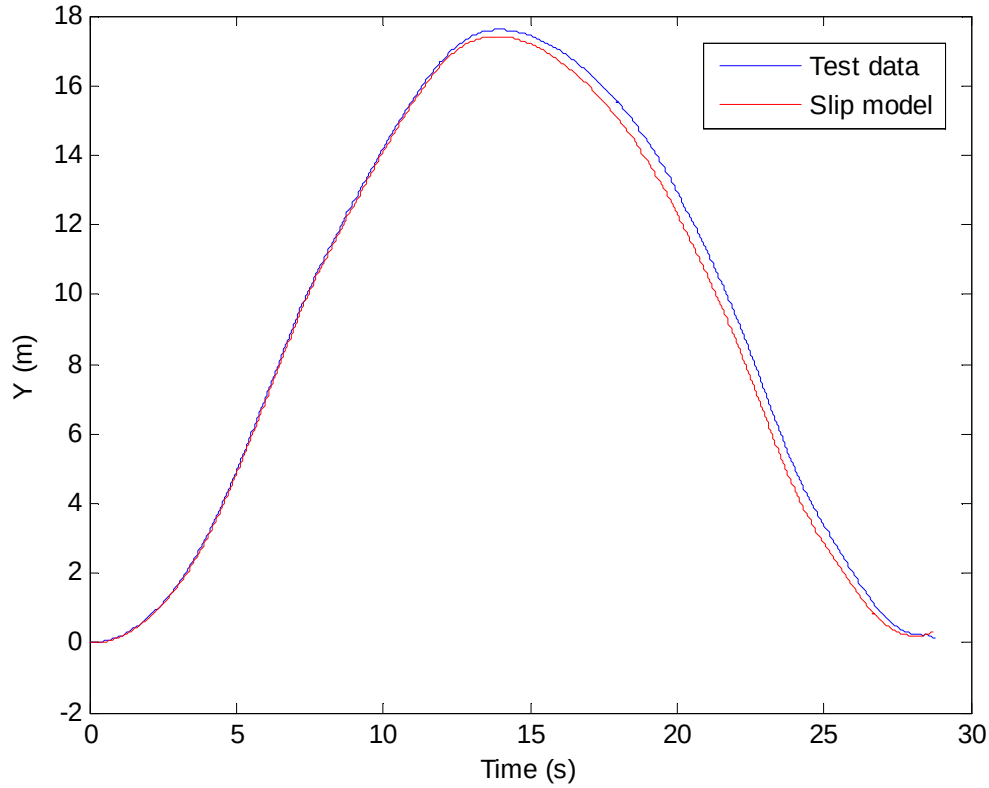

Figure 51. The *y* state trajectory of the path shown in Figure 48.

The heading associated with the path in Figure 48 is given in Figure 52. When compared to Figure 46, the rate of change of the heading has decreased to almost match the heading recorded during the test run.

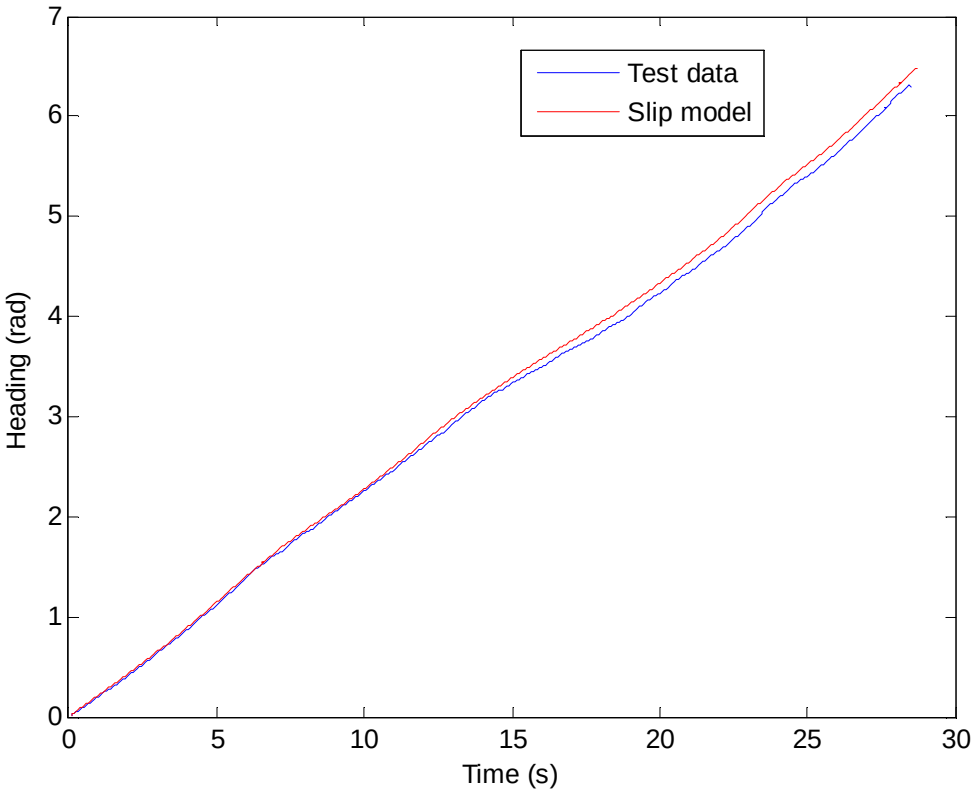

Figure 52. The heading trajectory of the path shown in Figure 48.

The original (grey) and the smoothed (red) estimated slip angles of the front and rear unit during the path given in Figure 48 are shown in Figure 53 and Figure 54, respectively. The smoothed graph averaged 500 data points per interval. The value of the slip angle stays below the 3° mark.

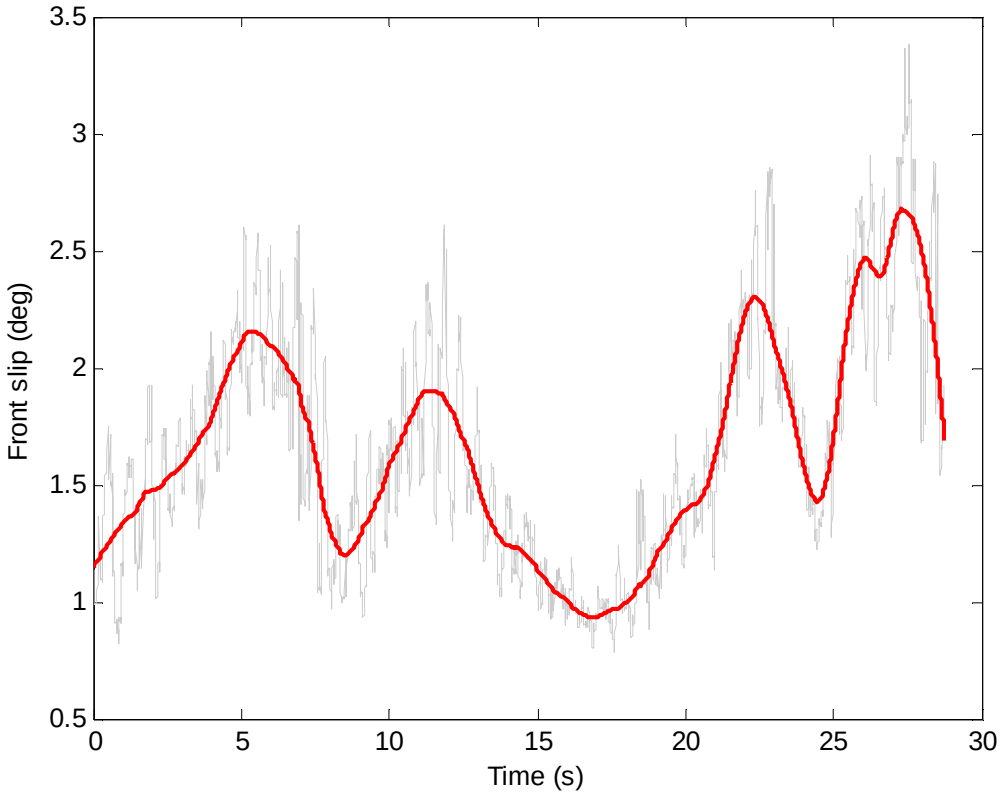

Figure 53. The estimated slip angle of the front unit during the path shown in Figure 48.

The value of the rear unit slip angle, shown in Figure 54, is marginally larger than that of the front unit. This is mainly caused by the larger weight on the rear tyres due to the heavier rear unit. As has been stated in chapter 4, an increase in vertical load generally reduces the friction coefficient of the tyre.

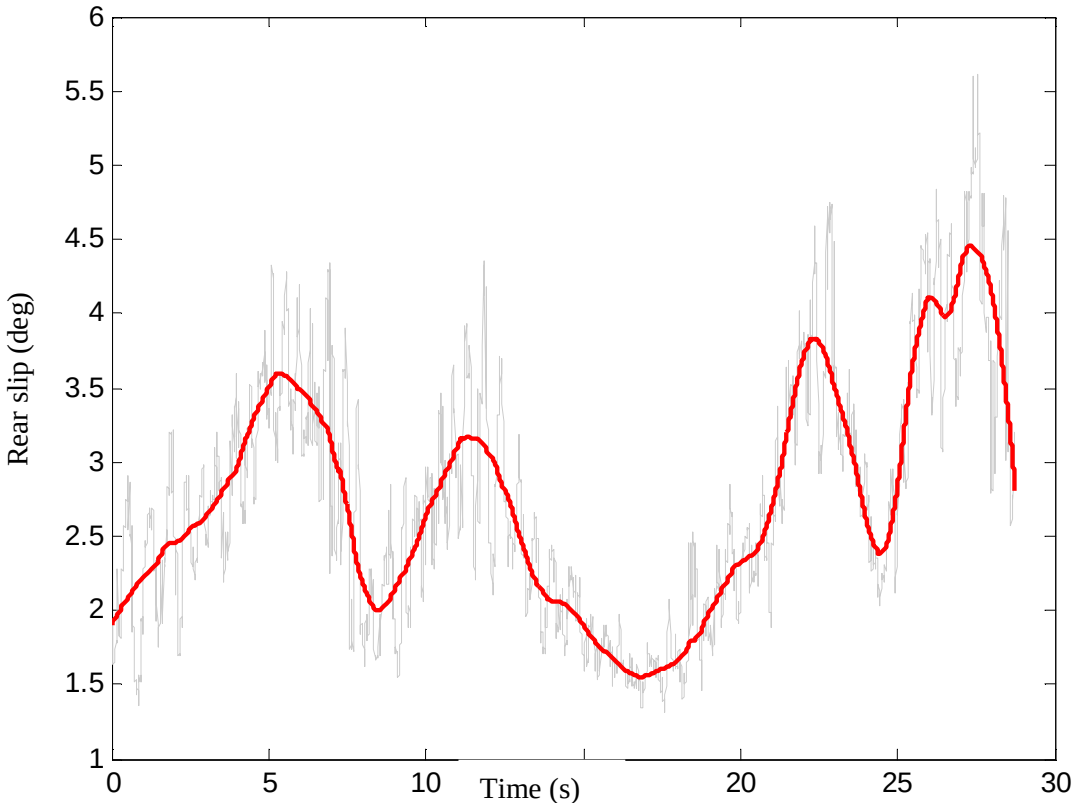

Figure 54. The estimated slip angle of the rear unit during the path shown in Figure 48.

The following slalom and lane change tests confirmed that the slip model is not nearly as accurate when the articulation angle is changing rapidly. Figure 55 shows the trajectory of the loader (blue line) compared to the predicted trajectory of both the slip and the no-slip models during a portion of a slalom manoeuvre. Again, the time-specific position errors of the predicting models are compared in Figure 56. Further comparisons are made in Figure 57 and Figure 58 where the *x* state and the *y* state trajectories are shown, respectively.

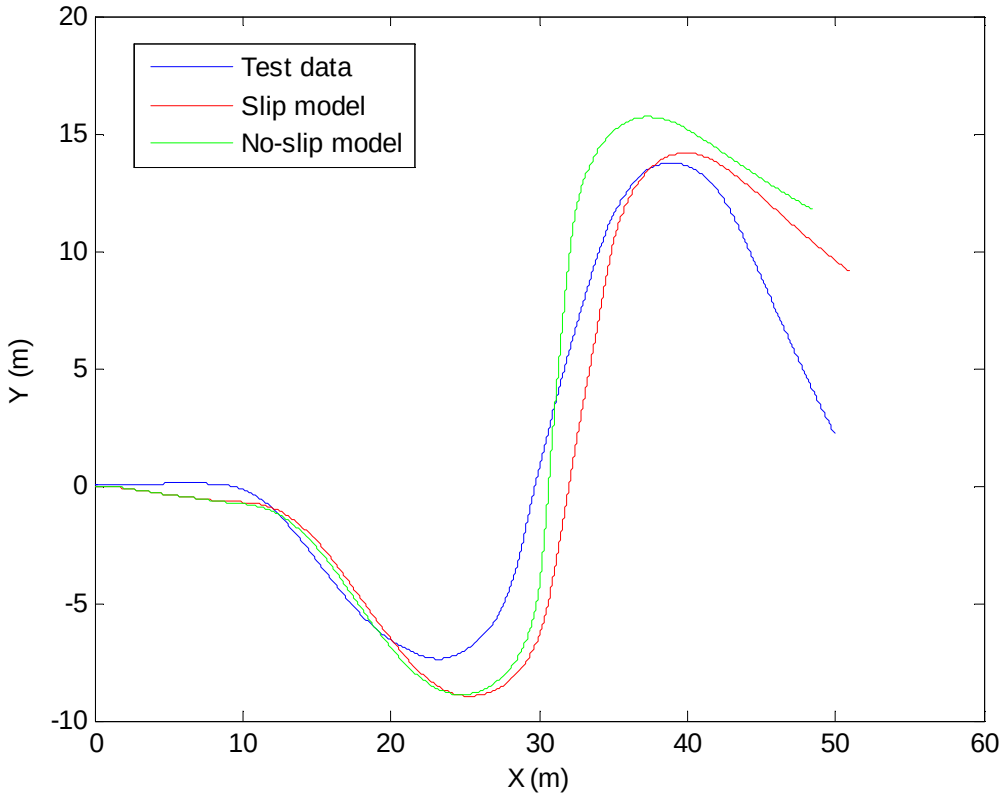

Figure 55. The trajectory of the loader compared to the predicted trajectories.

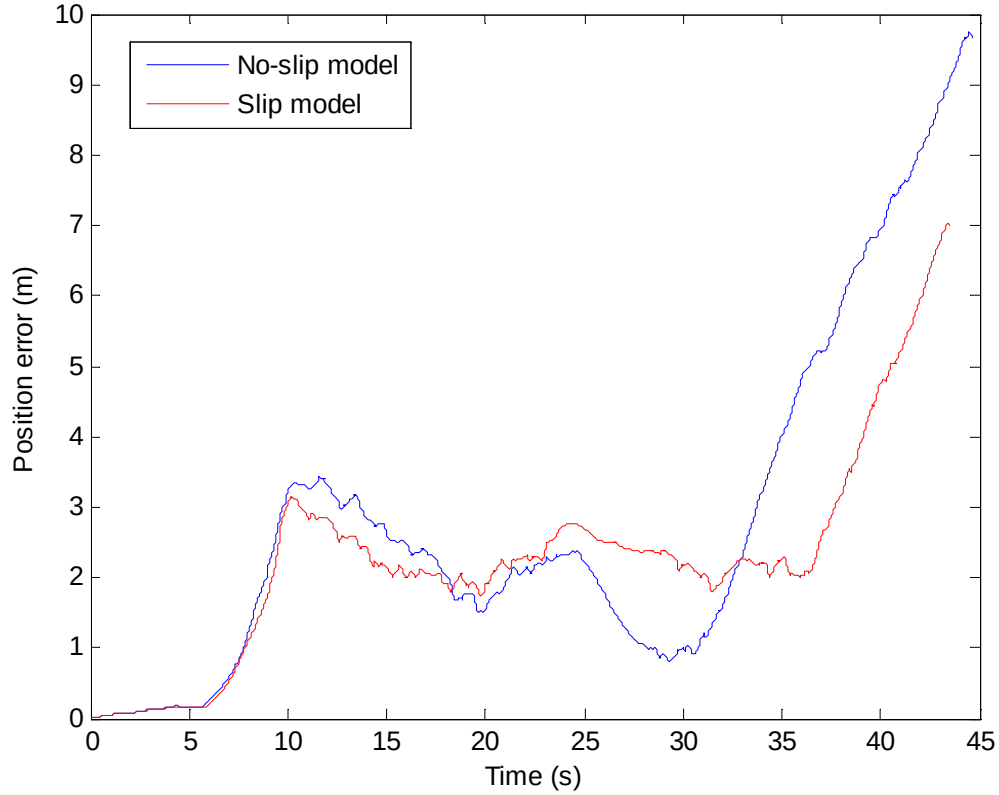

Figure 56. The position error comparison between the slip and no-slip models for the slalom manoeuvre.

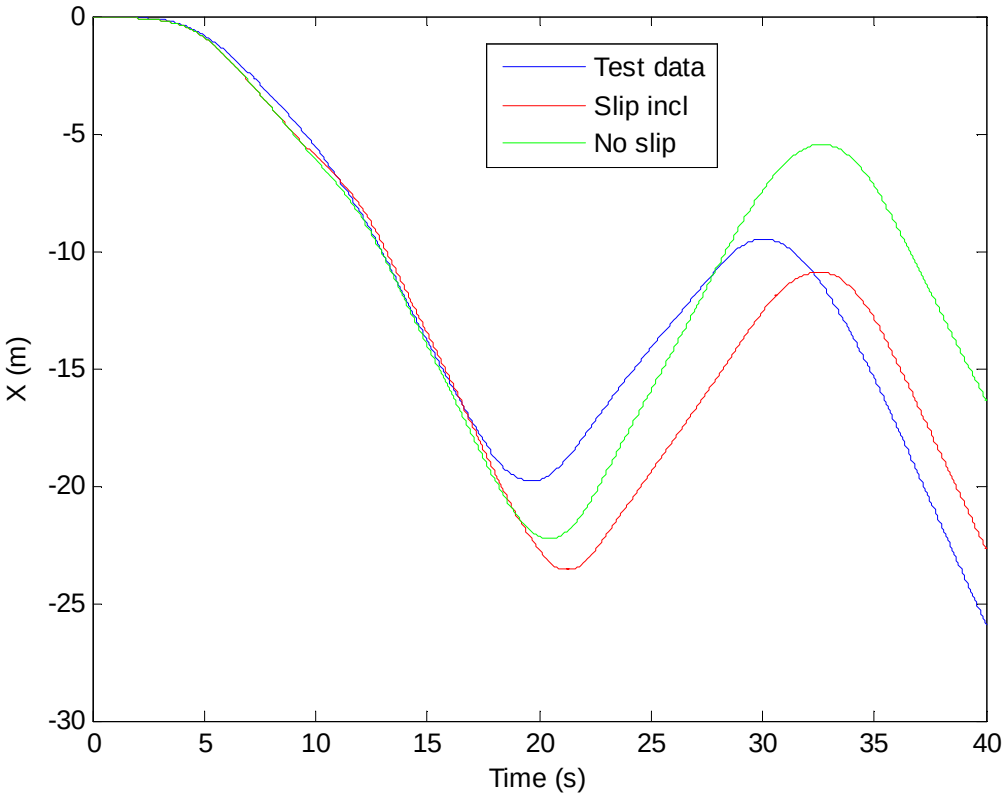

Figure 57. The *x* state trajectory comparison of the path shown in Figure 55.

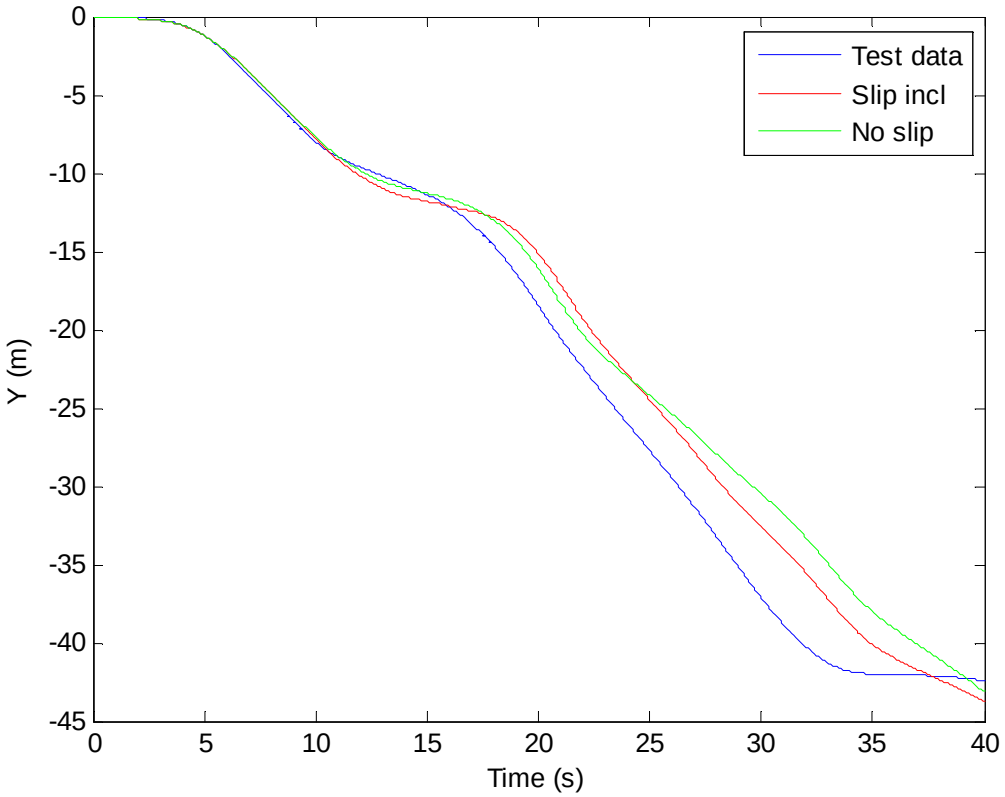

Figure 58. The *y* state trajectory comparison of the path shown in Figure 55.

Figure 59 and Figure 60 show the estimated front and rear unit slip angles, respectively.

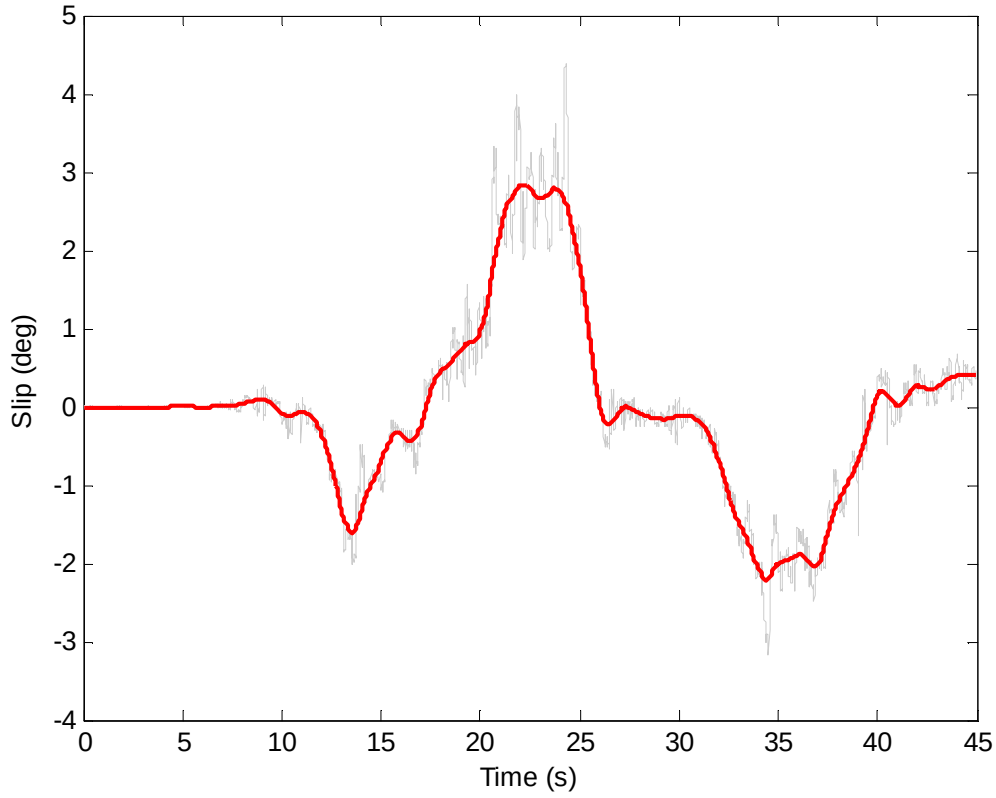

Figure 59. Front unit slip.

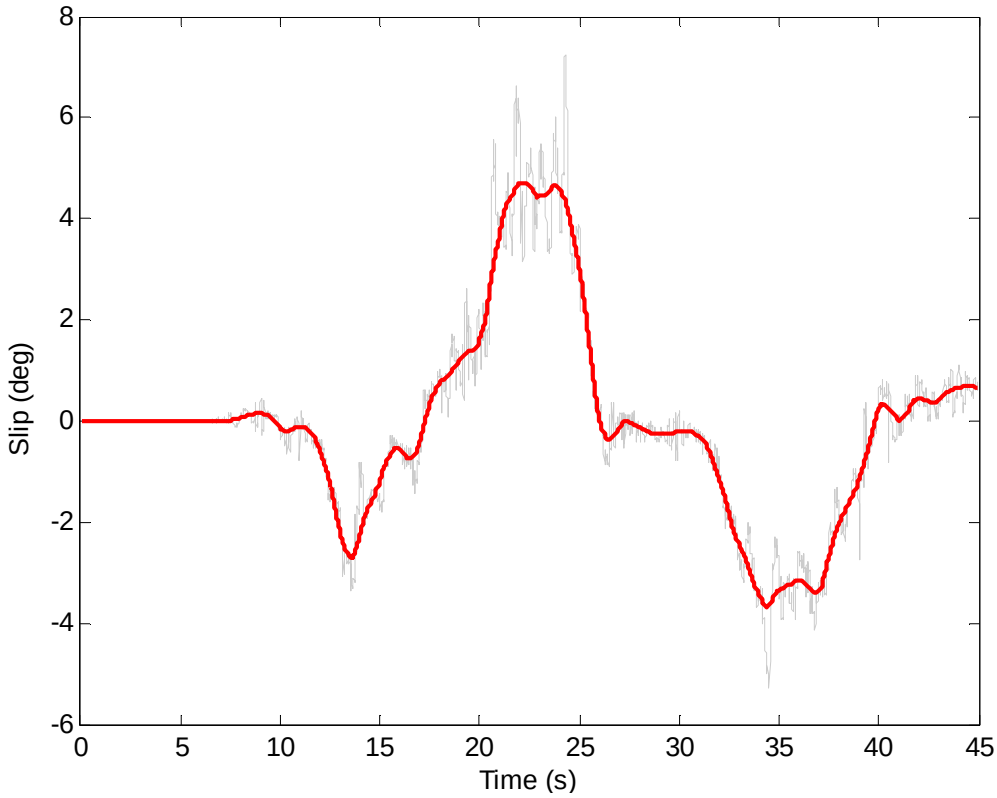

Figure 60. Rear unit slip.

5.2.1.2.1 Discussion

The inclusion of a tyre model in the kinematic model does improve the model's performance, especially during steady-state turning. Conversely, during rapid steering angle changes, as in Figure 55, the position error of the "slip model", depicted in Figure 56, is barely an improvement on the no-slip model. Although the above simulations are based on the empty loader, field tests suggest that the results concur with those of the fully loaded loader.

Inclusion of a slip angle is an attempt to involve some of the neglected dynamics of the vehicle in the purely kinematic model; in this case the dynamic property is the lateral force on the tyres. However, in order to produce a precise model, many more dynamic properties of the vehicle should be included. These include the longitudinal force on the tyres to account for skidding, the steering dynamics and the tyre's radius deformation. As is to be expected, this will complicate the model quite significantly and hence its application in real-time localization and control could prove to be impractical. The simplicity of the kinematic model, however, is a strong motivation to ignore these dynamic effects and rather concentrate on designing a robust control system and to handle the dynamic effects as external "disturbances"; these include the effects induced by wheel slippage.

5.3 DYNAMIC MODEL

Very few dynamic models have been developed for the LHD vehicle to date. The dynamic model [15], will be discussed here although the model has never been practically validated. [15] claims that, for small slip angles, their vehicle model incorporates an accurate tyre model. Details on the dynamic model and its tyre model are given in Chapter 4. The inputs to the model are the longitudinal forces (which is noted as the speed input) and the force required in altering the articulation angle (which is seen as the steering input). Due to the sensitive sensor suite required to sense such forces, it is difficult to validate the model using practical data gathered from field trials. Validating such a model is beyond the scope of this project and so only the simulation results will be discussed here. This implies that it is impossible to compare the above-mentioned practical results gathered from either the LHD or the articulated loader directly to the simulation results of this dynamic model.

A number of parameters need to be defined in order to run the simulation.

Table 10 shows the parameters for the Bell L1706E. The values where mostly obtained from [73] and from practical experiments. The estimation of the moments of inertia about the vertical axes, however, where derived from [71]. The friction coefficient was taken as a typical value for a gravel road surface [68].

Table 10. The Bell L1706E wheeled loader parameters.

Parameter	Description	Value
m_1	Mass of front unit	4800 kg
m_2	Mass of rear unit	8400 kg
Tw1	Track width of vehicle axle	2.048 m
$C_{\alpha f}$	Cornering stiffness of front tyres	2000 N/m
$C_{\alpha r}$	Cornering stiffness of rear tyres	2000 N/m
I_{z1}	Moment of inertia about vertical axis of the front unit	50000 kg·m^2
I_{z2}	Moment of inertia about vertical axis of the rear unit	50000 kg·m^2
h	Vertical height of the centre of gravity	1 m
h_l	Vehicle half length	1.5 m
L_1	Distance between front unit centre of gravity and front axle	1.9 m
L_2	Distance between rear unit centre of gravity and rear axle	1.1 m
μ	Friction coefficient	0.5
a_{max}	Maximum Acceleration	1.86 m/s^2
a_{min}	Maximum Deceleration	2.5 m/s^2
$\dot{\varepsilon}_{f\max}$	Maximum rate of change of steering angle	0.48 rad/s or 27 deg/s
$\varepsilon_{f\max}$	Maximum steering angle	0.7 rad or 40 deg

5.3.1 Simulation

A sinusoidal trajectory was simulated in order to investigate the slip angles. Figure 61 shows this trajectory where both tight left- and right-turns were made.

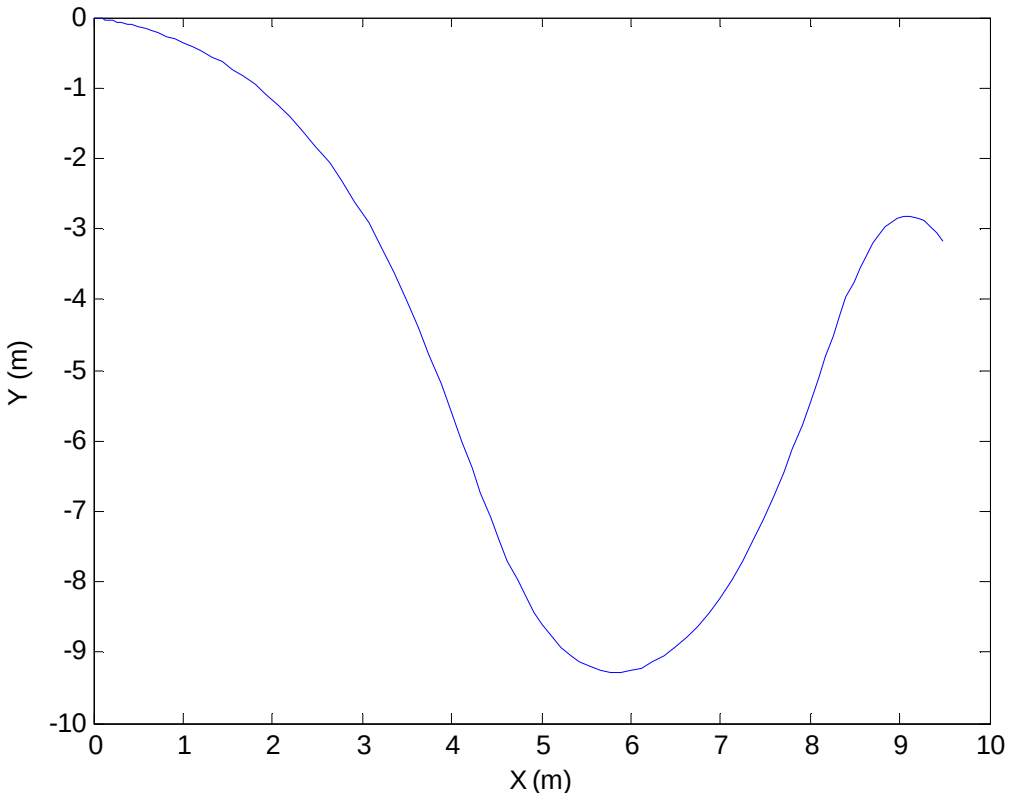

Figure 61. A sinusoidal path simulated with the dynamic model.

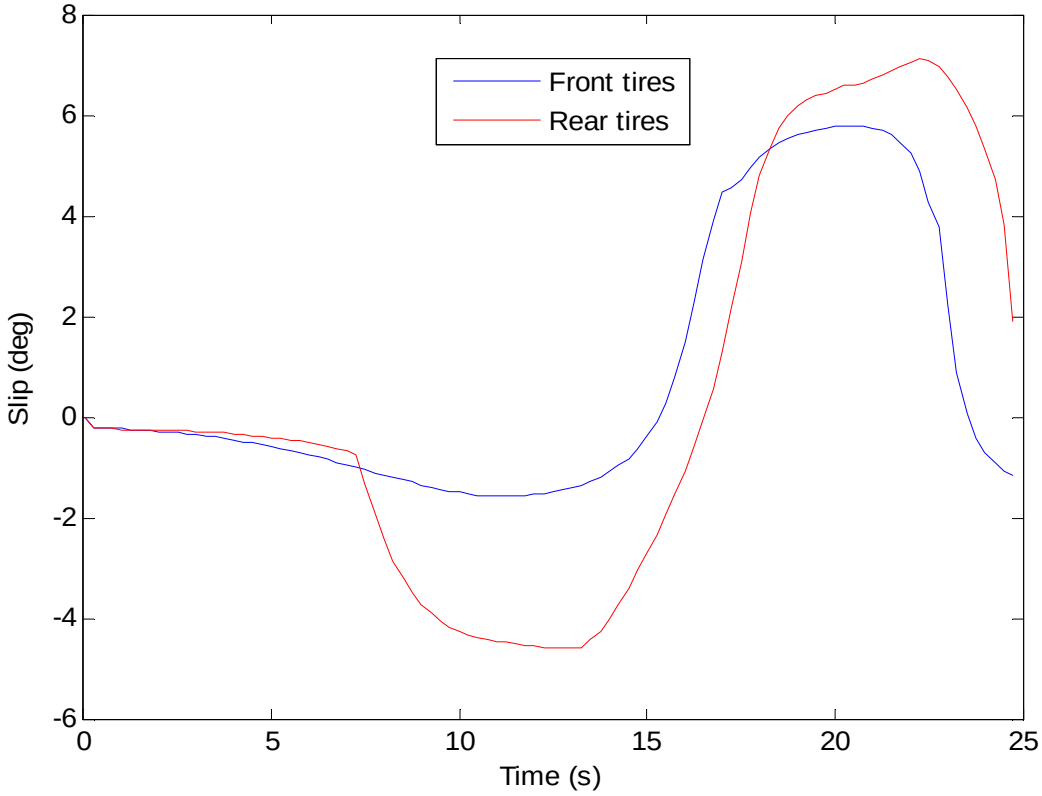

Figure 62. The front and rear slip angles, estimated by the dynamic model.

5.3.2 Discussion

The estimated slip angles are, intuitively, realistic. As the right-hand turn is made, the slip angles are negative and a left-hand turn results in a slip angle of opposite sign. The purpose of the above dynamic model, however, is not as intuitive.

The system was rewritten in a set of first-order differential equations resulting in a model with eight states. This system was then used to search for an optimal control vector which would drive the system of nonlinear differential equations to the desired set point, within specific constraints. Finding the optimal control vector was computationally intense and seldom drove the cost function to the desired value of zero. The time taken to run the short simulation depicted in Figure 61 takes roughly five minutes; the simulations were run on an Intel Xeon 5140 (Dual-Core) 2.33 GHz processor, with 2GB random access memory (RAM) and 1333MHz front-side bus (FSB). The realistic implementation of such a model, therefore, needs to be debated. [15] implemented the model using an open-loop control strategy. However, the cost function of the control strategy rarely tended towards the

desired zero value, mainly due to the complex method by which its inputs are defined. Straightforward physical implementation on a LHD vehicle, therefore, is not a plausible option. The purpose of the model, according to [15], might therefore be similar to that of a Kalman filter. It would then be used to update and improve the estimate of the vehicle's position between samples of an external sensor in a navigation system. The computational requirements, however, need to be drastically reduced.

A different purpose of such a dynamic model might therefore only be for vehicle development. Accurate estimates of the involved forces during cornering could give vehicle designers a good insight into the steering actuator requirements and the required strength of materials. But before any use for the dynamic model can be found, it needs to be validated.

In most cases, where a dynamic model is preferred over a kinematic model, a more accurate estimation is required of the vehicle states. Also, the higher the speeds and the resultant forces that are involved are, the more reluctant one will be to implement a kinematic model. On the other hand, the relatively low speeds involved in the underground tramming process tend to persuade the developer to rely on the kinematic model. This implies that the control system governing the movement of the vehicle needs to be robust and reliant on accurate external sensing. Chapter 6 deals with this problem and indeed shows that navigation is possible without the need of a complex dynamic model.

5.4 CHAPTER SUMMARY

The test runs performed on the articulated vehicles were demonstrated in this chapter and some of the results were displayed and discussed. Then, the kinematic model was simulated and compared to the real test runs. The two prominent assumptions, namely vehicle half-length and wheel slippage, were tested and discussed. Also, the dynamic model by [15] was discussed. Furthermore, the practicality of a dynamic model was debated, were the conclusion was drawn that the real-time implementation of the current dynamic models are not practical. Modelling a LHD, therefore, should be based on kinematic principles.

CHAPTER 6

LOCALIZATION AND CONTROL

The control and underground localisation of a mining vehicle is a notable challenge. The task of navigation is to guide a vehicle/robot through its world using sensory information. In order to achieve this requirement, the following three questions need to be answered: Where am I? Where are other places relative to me? How do I get to those other places from here? To realize the second and third goals, the first question, which concerns the pose (position and orientation) estimation problem, is to be solved.

As has been mentioned in Chapter 3, a number of navigation methods exist in literature. However, few can guarantee the ideal scenario of an infrastructure-free guidance system which allows the vehicle to operate at its optimum operating speed. Even before a navigation system can be thought of, a sound and sufficiently accurate vehicle model is required.

In the section, the kinematic model developed in Chapter 4 will be used as the primary model around which a navigation system will be developed.

6.1 ABSOLUTE VERSUS REACTIVE NAVIGATION

In Chapter 3, both absolute and reactive navigation was explained. As a reminder, absolute navigation refers to a navigation system where the position of a vehicle is always known with respect to a real-world fixed coordinate system. In contrast, reactive navigation allows the vehicle to sense its immediate surroundings and hence react in relation to these surroundings. In absolute navigation, the vehicle's global position and pose is estimated by external sensors. It heavily relies on the fact that its absolute position and pre-determined path is accurately known, implying that its sensor's should be exact. Also cumulative position errors are to be kept to a strict minimum, which entails regular sensor updates.

Contrary to the implementation by aforementioned literature, a new navigation scheme is developed in this section which implements both absolute and reactive navigation. The new navigation scheme incorporates opportunistic localization with absolute path planning.

6.1.1 Opportunistic localization

Opportunistic localisation is a term first defined by [6] and refers to a procedure where the autonomous vehicle uses reactive navigation techniques to guide itself along a path (by wall-following for instance) and uses opportune situations to confirm its location. Such opportune situations could be a natural landmark, an intersection or any other recognizable location.

The structured environment of an underground mine is a fitting setting for opportunistic localization. During the tramming procedure, an LHD will encounter numerous intersections which would act as recognizable landmarks to enable the vehicle to locate itself within a global (and local) framework.

The challenge arises in the sensing and detecting of such a landmark. As discussed in Chapter 3, the best-suited sensor to detect immediate surroundings in an underground mining environment is a two-dimensional laser scanner. Figure 63 shows a cumulative laser reading, enabling the vehicle to “see” its immediate surroundings; recognizing an intersection is not trivial process.

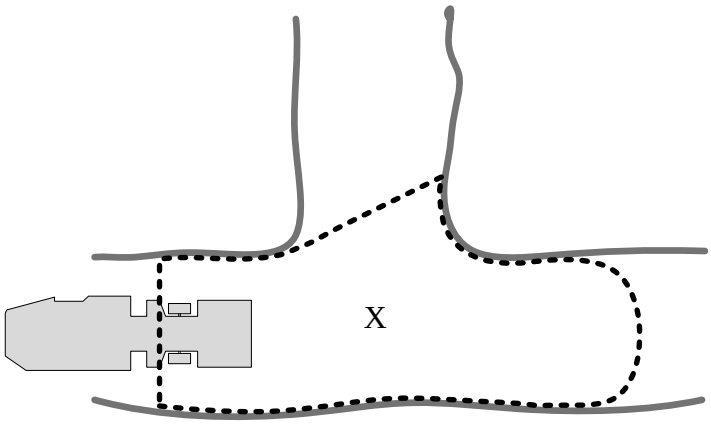

Figure 63. A laser scanner sensing an intersection.

With reference to Figure 63, the vehicle will recognize this specific intersection as ‘X’. Each labelled landmark will represent a node. The desired path can now be laid out by a sequence of these nodes. Figure 64 shows an example of a simple circuit or pathway described by a sequence of nodes: A-B-C-D-E-F.

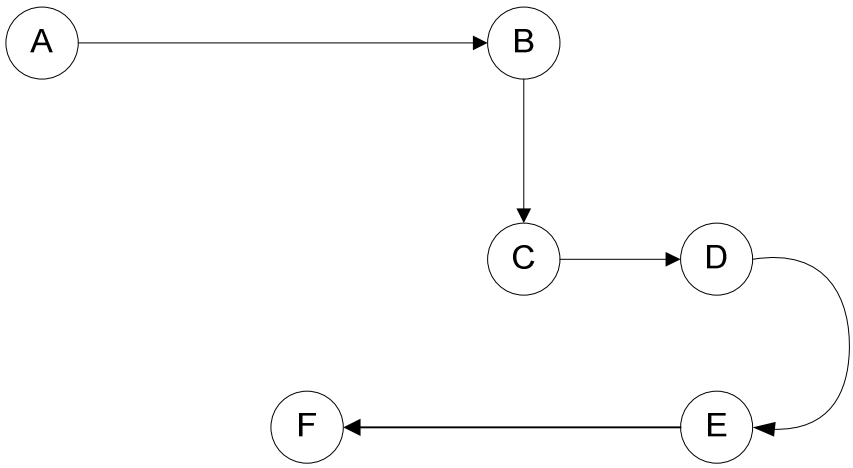

Figure 64. A simple pathway described by a sequence of nodes.

The automated vehicle starts at node ‘A’ and proceeds up to node ‘F’. The following table lists potential properties defining each node. Each property is coupled with an instruction.

Table 11. The property of each node.

Node	Instruction
A	Start
B	Intersection
C	Intersection
D	Circular/curved path start
E	Circular/curved path end
F	Stop

No specific path-learning is required, but the vehicle needs to know the metric position of the upcoming node with reference to the previous node. The position of the upcoming node is defined by an x-y coordinate system derived from the vehicle’s odometry sensors.

As mentioned in Chapter 3, odometry errors, in practice, are as low as 1% for LHD vehicles when travelling over short distances (the distance between nodes is relatively short). Once a node has been passed, the vehicle's local metric coordinate position is reset to (0;0).

Vehicle guidance requires a look-ahead strategy to achieve accurate path tracking. Circular interpolation incorporates this feature by anticipating changes in path curvature and optimum vehicle heading and position. Adding such circular interpolation to the circuit in Figure 64 by choosing three consecutive nodes as points on the circular path gives the layout shown in Figure 65.

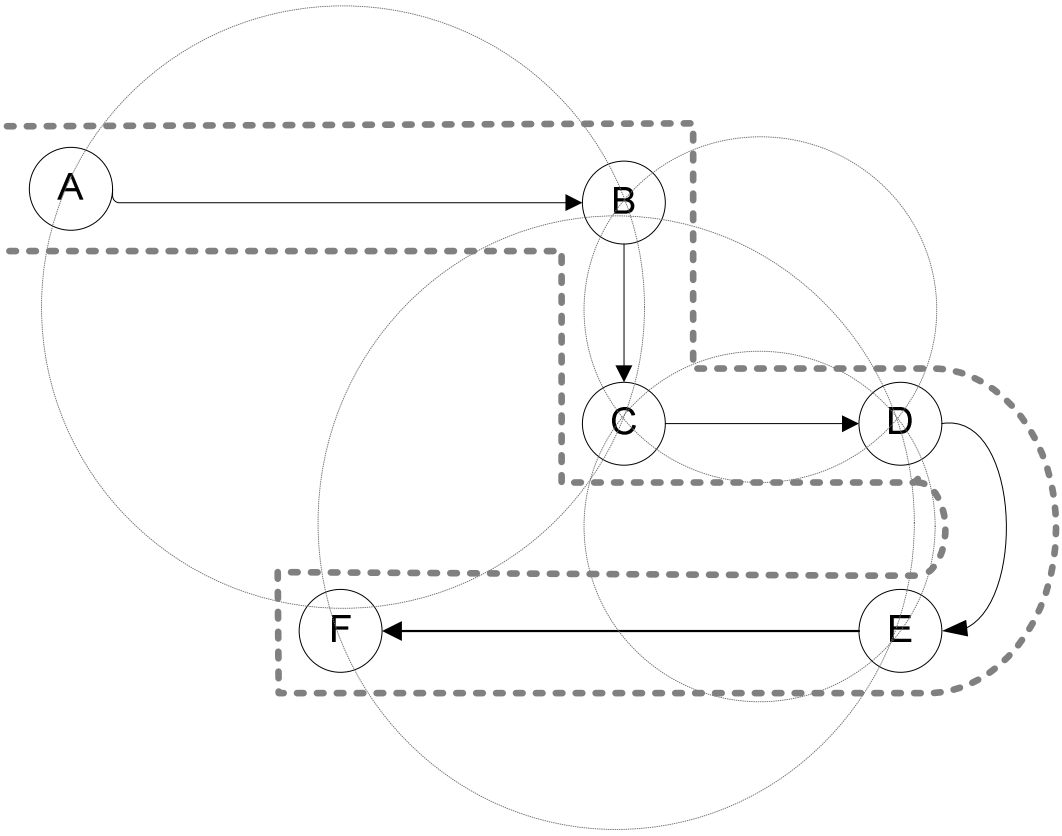

Figure 65. The circuit layout with wall boundaries and circular path description.

With reference to Figure 65, four circles (ABC, BCD, CDE and DEF) are drawn to represent the circular pathway between the nodes. The dotted line outlying the circuit represents the tunnel walls. The red pathway shown in Figure 66 indicates the desired circular pathway.

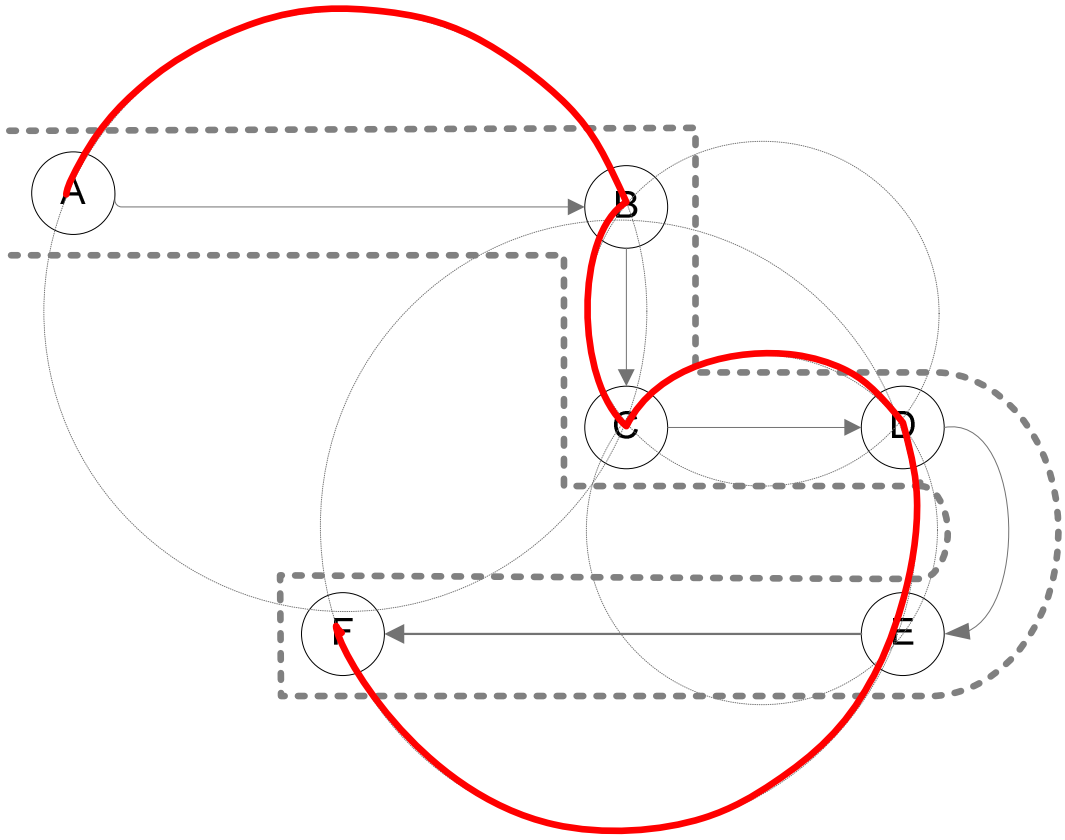

Figure 66. The circuit layout with respective radius measurement and proposed pathway.

With reference to Figure 66, the circular pathway intercepts the tunnel walls on numerous occasions. Such an instance is during the route from node A-B. A simple solution would be to add an extra node in between nodes A and B, calling it ‘Z1’. Now, the circle AZ1B will have a large radius, ensuring that the desired pathway from A-B will not intercept the tunnel walls. This solution, however, implies that the vehicle’s navigation system has to have a-priori knowledge of the position of the extra node since this node may not necessarily be recognizable by a natural landmark. The position of the added node will be defined by its x-y position in relation to the previous node. Figure 67 shows the circuit with added nodes.

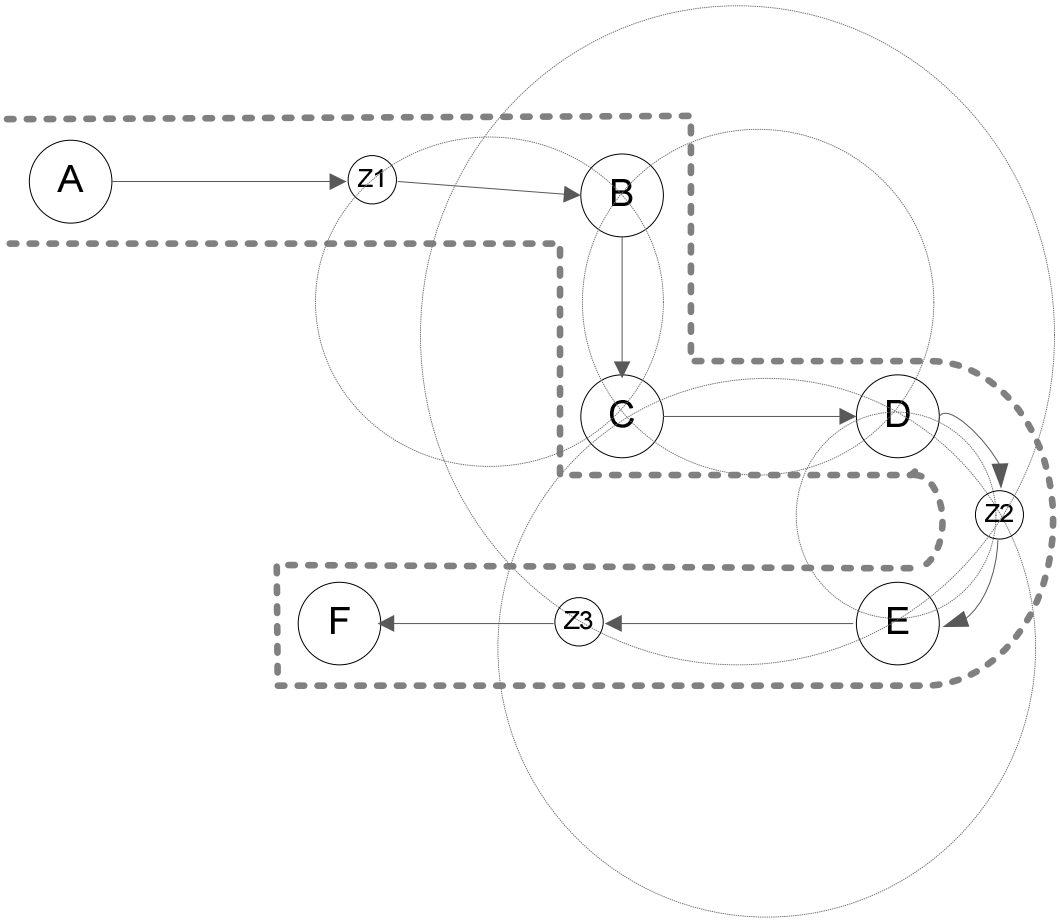

Figure 67. The circuit layout with added nodes.

Nodes Z1, Z2 and Z3 were placed in specific positions which will ensure that the vehicle's path does not intercept any of the tunnel walls. The new circles formed by the inclusion of the extra nodes are also displayed in Figure 67. The projected pathway is highlighted in Figure 68.

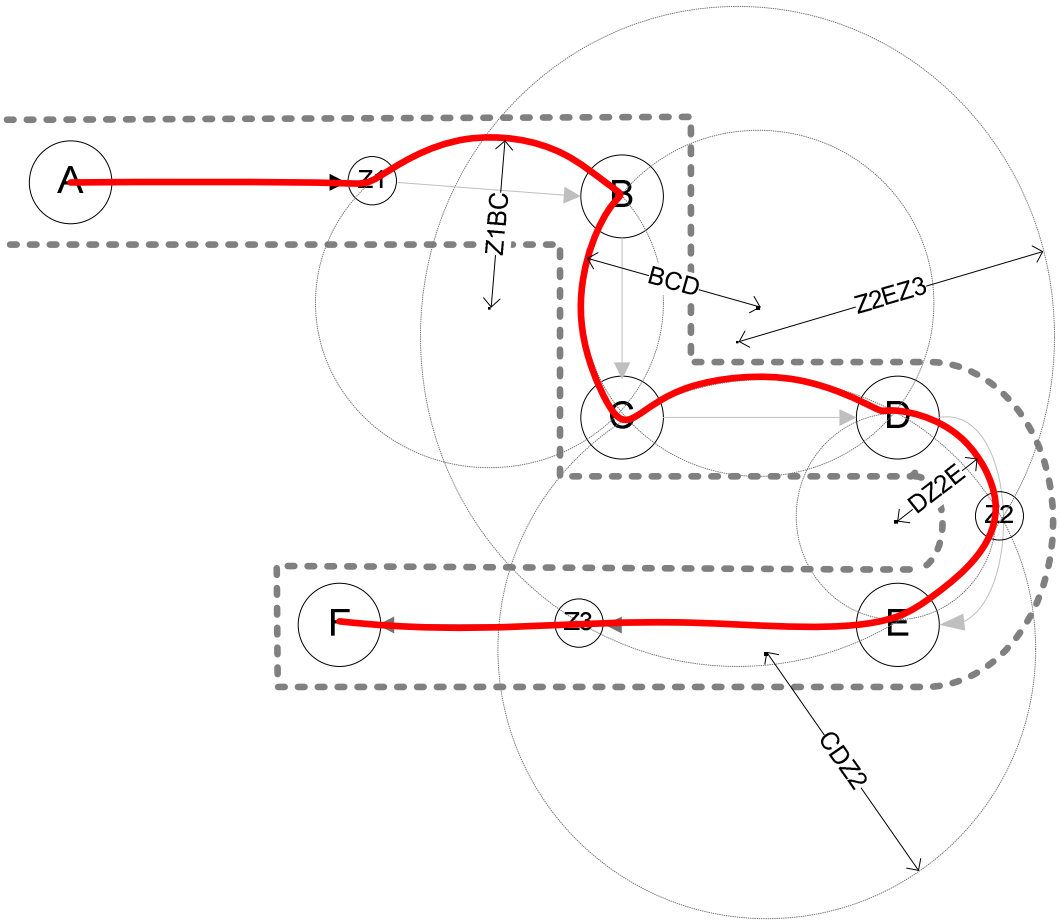

Figure 68. The route from node A to node F described by the circular pathway.

With reference to Figure 68, the highlighted pathway does not intersect the tunnel walls. However, distinct impractical kinks result at nodes B and C. These can be smoothed by adding a node in close proximity both before and after a turn, in line with the previous and upcoming node. The curved projection before approaching a sharp turn ensures that the vehicle can travel at higher speeds through the corner than it would if it were to approach the corner in a straight line. The vehicle's trajectory will depend on the radius of each of the circular segments and is defined in the following way for this specific circuit layout:

1. Start at node A and calculate radius of circle AZ1B.
2. Track the trajectory of circle AZ1B clockwise and proceed towards node Z1.

3. At node Z1, calculate radius Z1BC.
4. Track the trajectory of circle Z1BC clockwise and proceed towards node B.
5. At node B, calculate radius BCD.
6. Track the trajectory of circle BCD anticlockwise and proceed towards node C.
7. At node C, calculate radius CDZ2.
8. Track the trajectory of circle CDZ2 clockwise and proceed towards node D.
9. At node D, calculate radius DZ2E.
10. Track the trajectory of circle DZ2E clockwise and proceed towards node Z2.
11. At node Z2, calculate radius Z2EZ3.
12. Track the trajectory of circle Z2EZ3 clockwise and proceed towards node E.
13. At node E, calculate radius EZ3F.
14. Track the trajectory of circle EZ3F clockwise and proceed towards node Z3.
15. At node Z3, proceed straight towards F.
16. Stop at node F.

The algorithm or instructions given above are fed to the vehicle's navigation system. Next, the method of determining the radius of each of the circular segment is given.

Figure 68 gives the radius of each circular segment for the particular node placement. The radius of a circle is calculated using the method depicted in Figure 69.

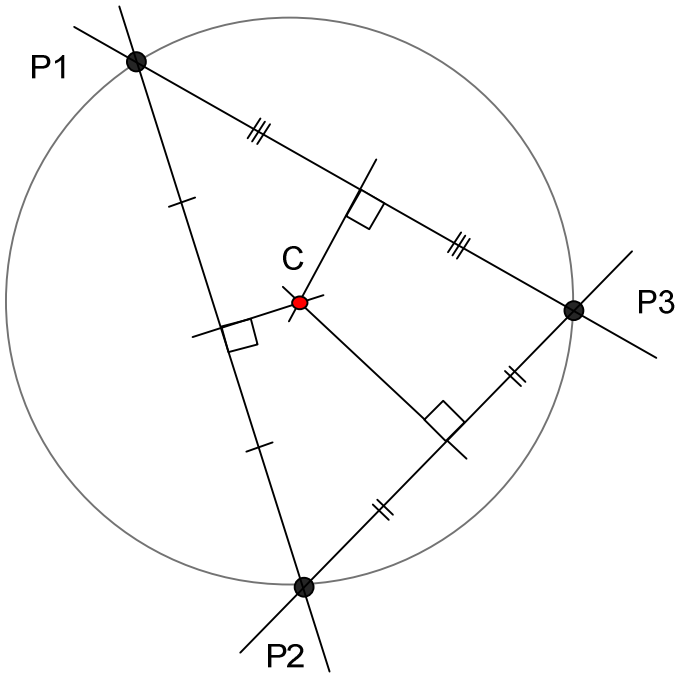

Figure 69. The method for calculating the radius of a circle from three concentric points.

We define the x-y coordinates of each of the three points on the circle as follows:

$$P1 = (x_1;y_1), \tag{6.0}$$

$$P2 = (x_2;y_2), \tag{6.0}$$

$$P3 = (x_3;y_3), \tag{6.0}$$

and C represents the position of the circle centre.

We also define the length of the three sides of the triangle as follows:

$$|P1P2| = \sqrt{(x_2 - x_1)^2 + (y_2 - y_1)^2} = a, \tag{6.1}$$

$$|P2P3| = \sqrt{(x_3 - x_2)^2 + (y_3 - y_2)^2} = b, \tag{6.2}$$

$$|P3P1| = \sqrt{(x_1 - x_3)^2 + (y_1 - y_3)^2} = c, \tag{6.3}$$

and

$$s = \frac{(a+b+c)}{2}, \tag{6.4}$$

is the semi-perimeter.

Now, the radius of the circle is given by

$$radius = \frac{abc}{|\Delta P1P2P3|}, \tag{6.5}$$

where $|\Delta P1P2P3|$ is the area of the triangle. The area of the triangle is given by

$$|\Delta P1P2P3| = \sqrt{s(s-a)(s-b)(s-c)}\,. \tag{6.6}$$

6.2 CONTROL

Now, with the desired pathway described by the circular segments, the challenge is to keep the vehicle on the desired trajectory. Two distinct methods to guide the vehicle along the circuit layout given in Figure 68 will be investigated and simulated: optimal control and path-tracking. The control architectures are built around the no-slip kinematic model of the LHD.

6.2.1 Nonlinear optimal control

The basic objective of optimal control is to determine the control signals that will cause a process to satisfy the physical constraints and at the same time minimize some performance criterion [74]. In this case the performance criterion will be a cost function containing the desired final states at the nodes and to minimize the time to reach the desired states.

The no-slip kinematic model representing the pose of the front LHD unit is given by

$$\dot{x} = v\cos(\phi), \tag{6.7}$$

$$\dot{y} = v\sin(\phi), \tag{6.8}$$

$$\dot{\phi} = \frac{-v\sin(\gamma) - l_2\dot{\gamma}}{l_1\cos(\gamma) + l_2}, \tag{6.9}$$

where x is the horizontal displacement, y is the vertical displacement, v is the velocity, γ is the articulation angle, ϕ is the heading, l_1 is the length of the front unit and l_2 is the length of the rear unit. The velocity, v, and the articulation angle rate, $\dot{\gamma}$, are the inputs to the system. For simplicity, the time dependency has been omitted. The variable transformation to obtain $\overline{f}(\overline{z}(t), t)$ is made by:

$$\begin{bmatrix} z_1 \\ z_2 \\ z_3 \\ z_4 \\ z_5 \\ z_6 \end{bmatrix} = \begin{bmatrix} x \\ y \\ \phi \\ \gamma \\ \dot{\gamma} \\ v \end{bmatrix}. \tag{6.10}$$

Now, the system given in equations (6.7) to (6.9) is

$$\begin{aligned} \dot{z}_1 &= z_6\cos(z_3) \\ \dot{z}_2 &= z_6\sin(z_3) \\ \dot{z}_3 &= \frac{-z_6\sin(-z_4) - l_2 z_5}{l_1\cos(z_4) + l_2}, \\ \dot{z}_4 &= z_5 \\ \dot{z}_5 &= u_1 \\ \dot{z}_6 &= u_2 \end{aligned} \tag{6.11}$$

where the new inputs, u_1 and u_2 represent the articulation angle acceleration ($\ddot{\gamma}$) and vehicle acceleration ($\dot{v}$), respectively. The parameters of the Bell L1706E wheeled loader were used (given in section 5.3, Table 10), where the length of the front unit, l_1, was given as 1.5m and the length of the rear unit, l_2, 1.9 m.

6.2.1.1 Constraints

The constraints given below were verified by the tests done on the articulated loader and are similar to the constraints experienced by underground LHD vehicles.

The vehicle's articulation angle, given in radians, is constrained as follows:

$$-0.7 \leq z_4 \leq 0.7, \tag{6.12}$$

and the velocity of the vehicle, in m/s^2, is limited as follows:

$$-4.2 \leq z_6 \leq 4.2. \tag{6.13}$$

The rate of change of the articulation angle, z_5, given in radians/second, is constrained as follows:

$$-0.48 \leq z_5 \leq 0.48. \tag{6.14}$$

Also, the system given in (6.11) has to adhere to an input constraint. The acceleration of the vehicle, u_2, given in m/s^2, is limited in the following way:

$$-2 \leq u_2 \leq 0.85. \tag{6.15}$$

Implementing a penalty function method to enforce the constraints, equations (6.12) to (6.15) are represented as

$$\bar{g}(\bar{z}(t), t) \geq 0, \tag{6.16}$$

where $\bar{g}$ is a vector function of the states assumed to have continuous first and second partial derivatives with respect to state $\bar{z}(t)$. The function $\bar{g}(\bar{z}(t), t)$ is defined as

$$
\begin{aligned}
&g_1(z_4(t),t): z_4(t)+0.7\geq 0\\
&g_2(z_4(t),t): 0.7-z_4(t)\geq 0\\
&g_3(z_5(t),t): z_5(t)+0.48\geq 0\\
&g_4(z_5(t),t): 0.48-z_5(t)\geq 0\\
&g_5(z_6(t),t): z_6(t)+4.2\geq 0\\
&g_6(z_6(t),t): 4.2-z_6(t)\geq 0.
\end{aligned}
\tag{6.17}
$$

The inequality constraints given in (6.17) are converted to equality constraints be defining a new variable $z_7(t)$ by

$$
\begin{aligned}
\dot{z}_7(t)=&\left[g_1(z_4(t),t)\right]^2 h(g_1)+\left[g_2(z_4(t),t)\right]^2 h(g_2)+\left[g_3(z_5(t),t)\right]^2 h(g_3)+\\
&\left[g_4(z_5(t),t)\right]^2 h(g_4)+\left[g_5(z_6(t),t)\right]^2 h(g_5)+\left[g_6(z_6(t),t)\right]^2 h(g_6),
\end{aligned}
\tag{6.18}
$$

where $h(g_i)$ is a unit Heaviside step function defined by

$$
h(g_i)=\begin{cases}0, & \text{if } \bar{g}_i(\bar{z}(t),t)\geq 0,\\ 1, & \text{if } \bar{g}_i(\bar{z}(t),t)<0,\end{cases}
\tag{6.19}
$$

for i = 1, 2, ..., 6. The boundary conditions for $z_7(t)$ are

$$
z_7(t_0)=0\text{, and } z_7(t_f)=0\text{.}
\tag{6.20}
$$

6.2.1.2 Solving the system

Choosing a minimum time performance index of

$$
J=\int_{t_0}^{t_f}1dt\text{,}
\tag{6.21}
$$

the Hamiltonian is defined as

$$
\mathrm{H}(\bar{z}(t),\bar{u}(t),\bar{\lambda}(t),\lambda_7(t),t)=1+\bar{\lambda}'(t)\bar{f}(\bar{z}(t),\bar{u}(t),t)+\lambda_7(t)z_7(t),
\tag{6.22}
$$

where $\overline{\lambda}(t)$ is the set of co-state equations.

Applying the necessary optimality conditions for the state as

$$\begin{aligned} \dot{\overline{z}}^*(t) &= \frac{\delta H}{\delta \overline{\lambda}} = \overline{f}(\overline{z}^*(t), \overline{u}^*(t), t) \\ \dot{z}_7^*(t) &= \frac{\delta H}{\delta \lambda_7} = f_7(\overline{z}^*(t), t), \end{aligned} \tag{6.23}$$

for the co-state as

$$\begin{aligned} \dot{\overline{\lambda}}^*(t) &= -\frac{\delta H}{\delta \overline{z}} \\ \dot{\lambda}_7^*(t) &= -\frac{\delta H}{\delta z_7}, \end{aligned} \tag{6.24}$$

and for the control as

$$\mathrm{H}(\overline{z}^*(t), \overline{u}^*(t), \overline{\lambda}^*(t), \lambda_7^*(t), t) \leq \mathrm{H}(\overline{z}^*(t), \overline{u}(t), \overline{\lambda}^*(t), \lambda_7^*(t), t)\,. \tag{6.25}$$

The necessary condition for the state, given in equation (6.11), becomes

$$
\begin{aligned}
\dot{z}_1^* &= z_6^* \cos(z_3^*) \\
\dot{z}_2^* &= z_6^* \sin(z_3^*) \\
\dot{z}_3^* &= \frac{-z_6^* \sin(-z_4^*) - l_2 z_5^*}{l_1 \cos(z_4^*) + l_2} \\
\dot{z}_4^* &= z_5^* \\
\dot{z}_5^* &= u_1^* \\
\dot{z}_6^* &= u_2^* \\
\dot{z}_7^* &= \left[z_4 + 0.7\right]^2 h(z_4 + 0.7) + \left[0.7 - z_4\right]^2 h(0.7 - z_4) + \\
&\quad \left[z_5 + 0.48\right]^2 h(z_5 + 0.48) + \left[0.48 - z_5\right]^2 h(0.48 - z_5) + \\
&\quad \left[z_6 + 4.2\right]^2 h(z_6 + 4.2) + \left[4.2 - z_6\right]^2 h(4.2 - z_6)
\end{aligned}
\quad , \qquad (6.26)
$$

where the time dependency has been omitted for simplicity. The necessary condition for the co-state, using equation (6.24), is

$$
\begin{aligned}
\dot{\lambda}_1^* &= 0 \\
\dot{\lambda}_2^* &= 0 \\
\dot{\lambda}_3^* &= \lambda_1^* z_6^* \sin(z_3^*) - \lambda_2^* z_6^* \cos(z_3^*) \\
\dot{\lambda}_4^* &= \lambda_3^* z_6^* \cos(z_4^*) / (l_1 \cos(z_4^*) + l_2) - \lambda_3^* (-z_6^* \sin(z_4^*) - l_2 z_5^*) / (l_1 \cos(z_4^*) + l_2)^2 l_1 \sin(z_4^*) - \\
&\quad \lambda_7^* (2(z_4 + 0.7) h(z_4 + 0.7) - 2 * (0.7 - z_4) h(0.7 - z_4)) \\
\dot{\lambda}_5^* &= \lambda_3^* l_2 / (l_1 \cos(z_4^*) + l_2) - \lambda_4^* - \lambda_7^* (2(z_5 + 0.48) h(z_5 + 0.48) - 2(0.48 - z_5) h(0.48 - z_5)) \\
\dot{\lambda}_6^* &= -\lambda_1^* \cos(z_3^*) - \lambda_2^* * \sin(z_3^*) + \lambda_3^* \sin(z_4^*) / (l_1 \cos(z_4^*) + l_2) - \\
&\quad \lambda_7^* (2(z_6 + 4.2) * h(z_6 + 4.2) - 2 * (4.2 - z_6) h(4.2 - z_6)) \\
\dot{\lambda}_7^* &= 0
\end{aligned}
\quad , \qquad (6.27)
$$

where, again, the time dependency has been omitted for simplicity.

The unconstrained inputs are given by

$$
\begin{aligned}
u_1^*(t) &= -\lambda_5^*(t) \\
u_2^*(t) &= -\lambda_6^*(t) \, .
\end{aligned}
\qquad (6.28)
$$

However, since u_2(t) is constrained, as given in (6.15), it is defined as follows:

$$u_2^*(t) = \begin{cases} -2, & \text{if} \quad \lambda_6^*(t) < -2 \\ 0.85, & \text{if} \quad \lambda_6^*(t) > 0.85 \\ -\lambda_6^*(t), & \text{if} \quad -2 \le \lambda_6^*(t) \le 0.85 \end{cases} . \tag{6.29}$$

6.2.1.3 Simulation

The track layout similar to the layout given in Figure 68 was simulated using the constrained optimal control law. The metric layout of the track was adopted from the field trial run given in Figure 38. The simulations were performed using a maximum speed of 3 m/s or 10.8 km/h. The problem is based on the minimum-time principle, as can be deduced from the performance index given in equation (6.21). Hence, the minimum time taken to reach the next node was firstly determined after which the optimal control was calculated. Simulations were performed without any integrated observer feedback.

Figure 70 shows the vehicle's path with the superimposed circuit layout, starting at (0;0) in a X-Y metric coordinate system.

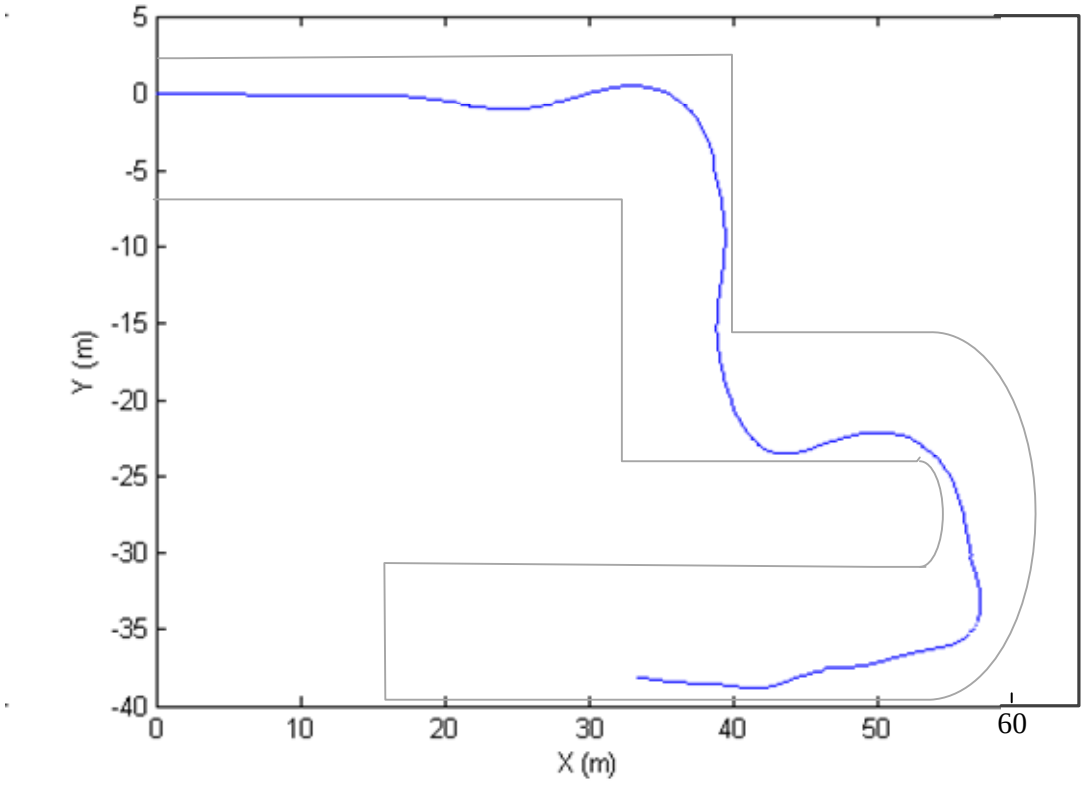

Figure 70. The simulated path using optimal control theory.

The nodes which define the track layout are added to Figure 70 to give Figure 71. The metric coordinate positions of each node were derived from the track trial run shown in Figure 38. The start and end positions of each of the states given in the system displayed in equation (6.26) were defined at each node. The minimization of the penalty function, which included the required final states and the minimum time requirement, was successfully met at almost all of the nodes. The trajectory between node Z2 and node E was the only section of the path which struggled to converge to a near-zero penalty function. The reason for this is the non-optimal starting value of the articulation angle at node Z2. Planning more weight on the importance of the optimal articulation angle at the end of trajectory D - Z2 should lead to better convergence. The X and the Y trajectories are given in Figure 72 and Figure 73, respectively.

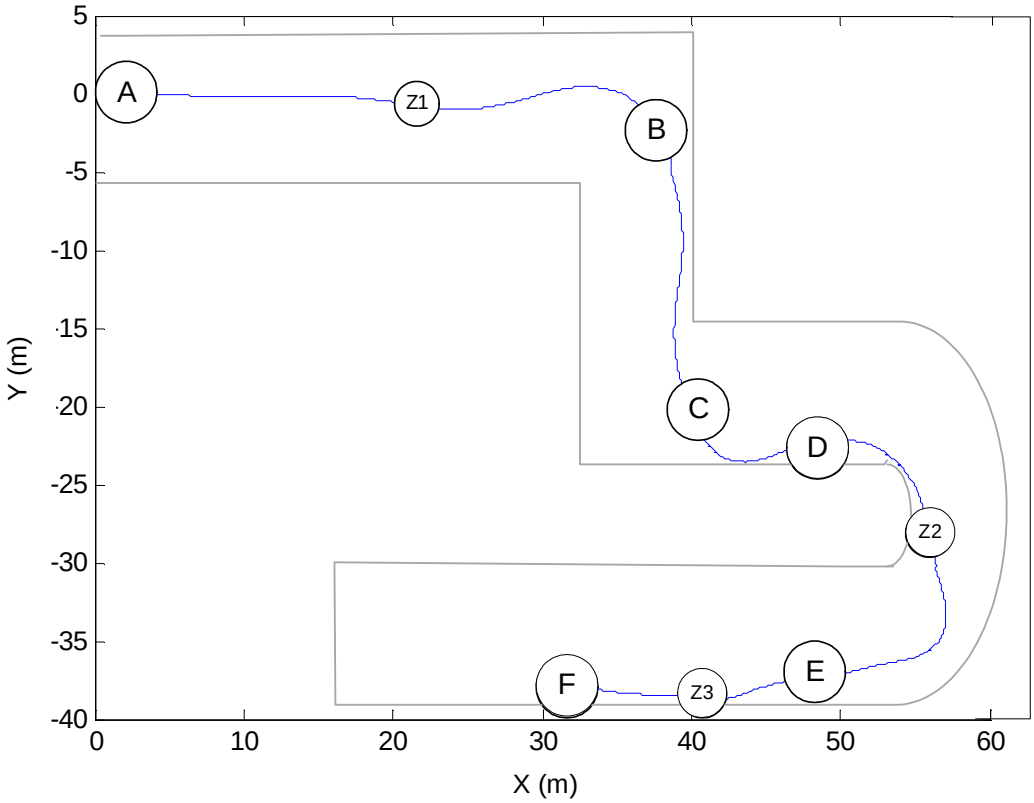

Figure 71. The simulated path with node positions.

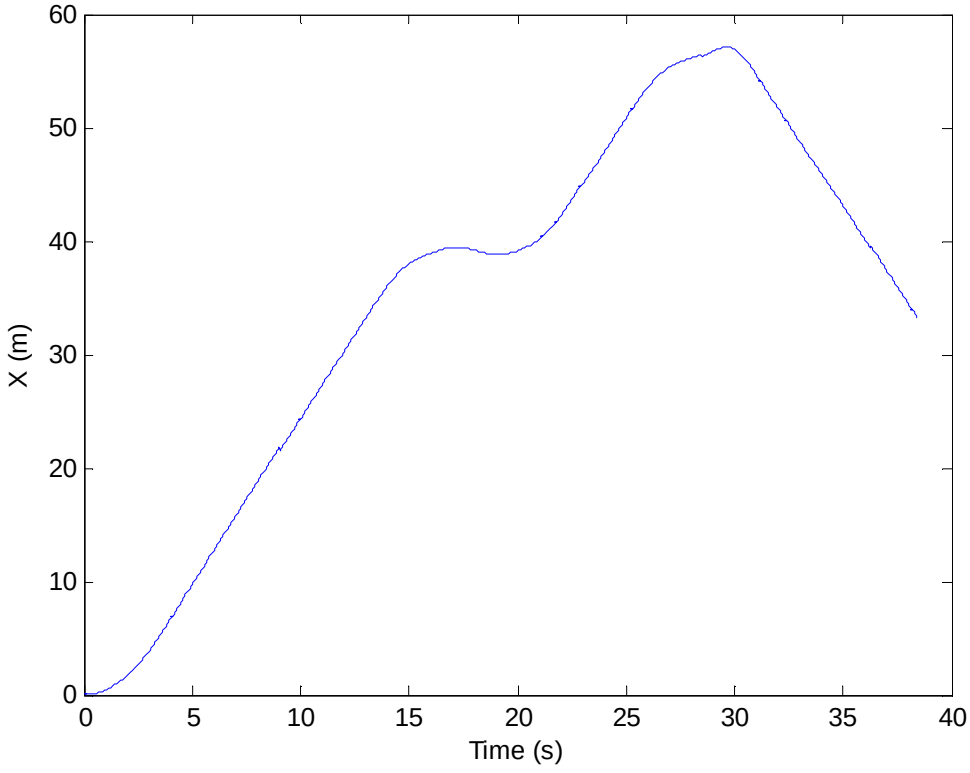

Figure 72. The X-coordinate trajectory.

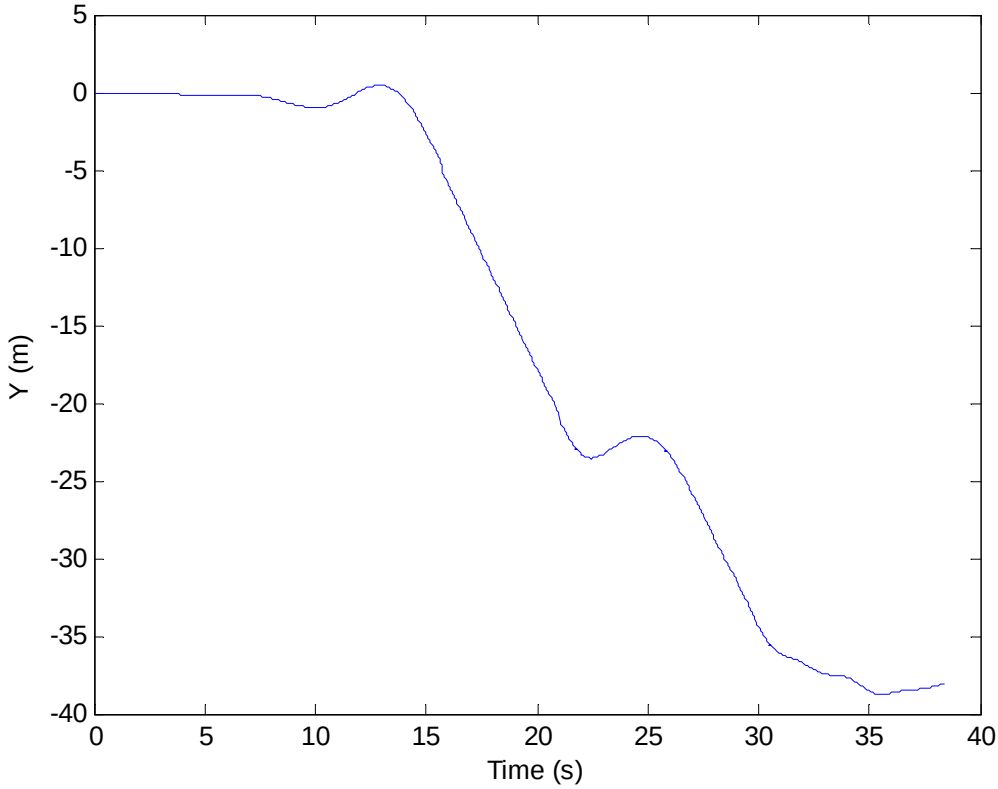

Figure 73. The Y-coordinate trajectory.

Figure 74 shows the heading of the simulated vehicle while Figure 75 shows the vehicle's predicted articulation angle. The articulation angle does not exceed its constraints which were stipulated in equation (6.12).

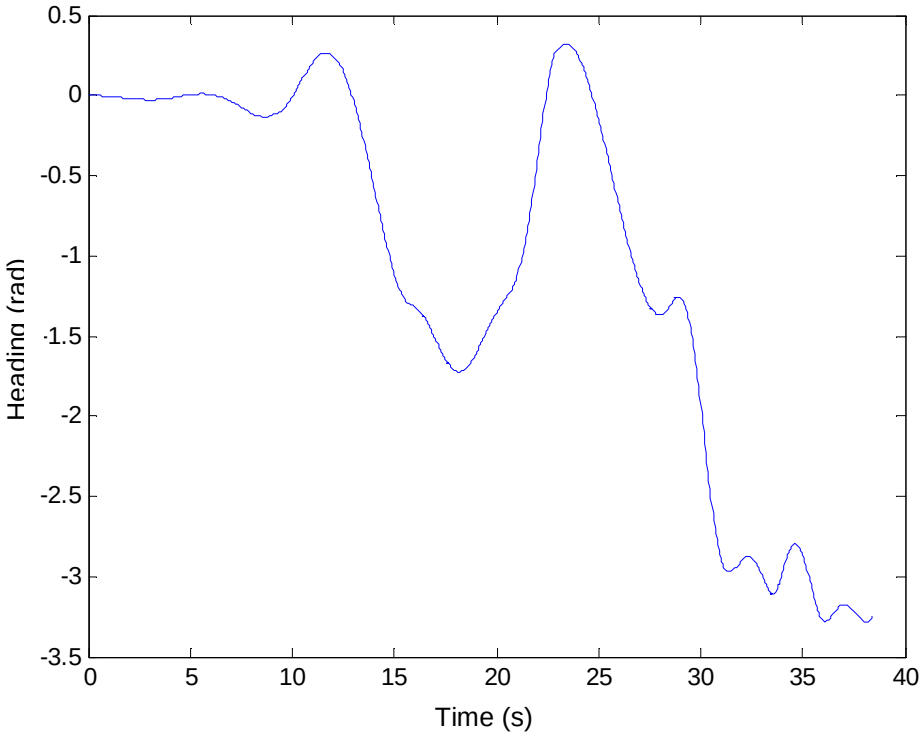

Figure 74. The simulated vehicle's heading.

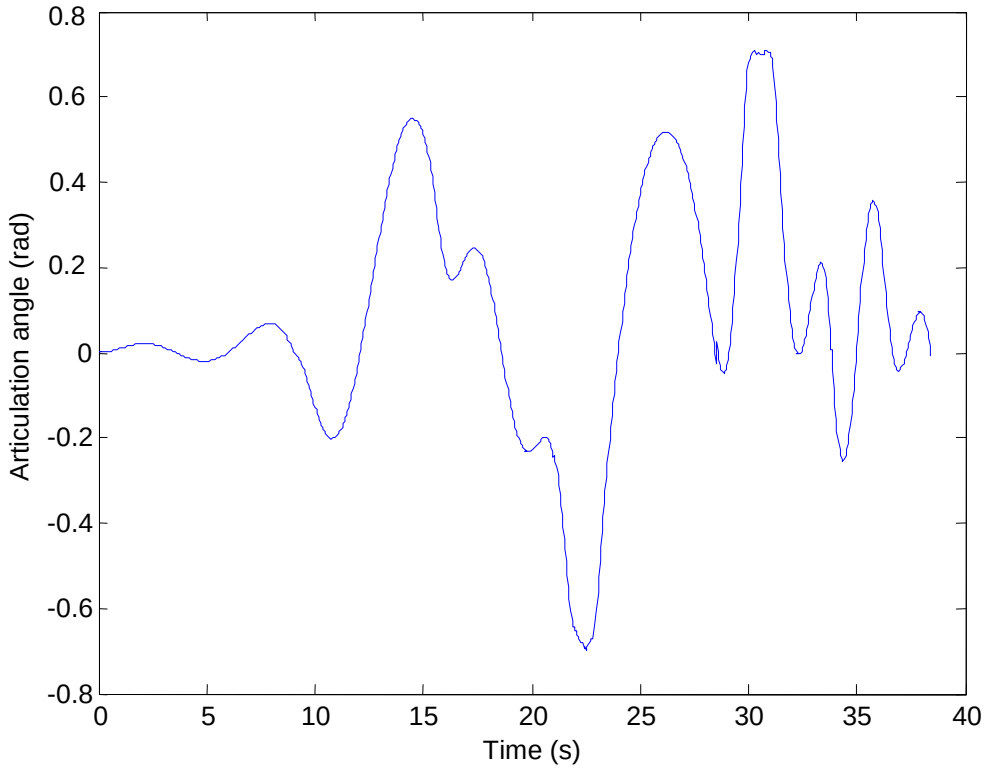

Figure 75. The simulated articulation angle.

The articulation angle rate, shown in Figure 76, does not exceed its constraints given in equation (6.14).

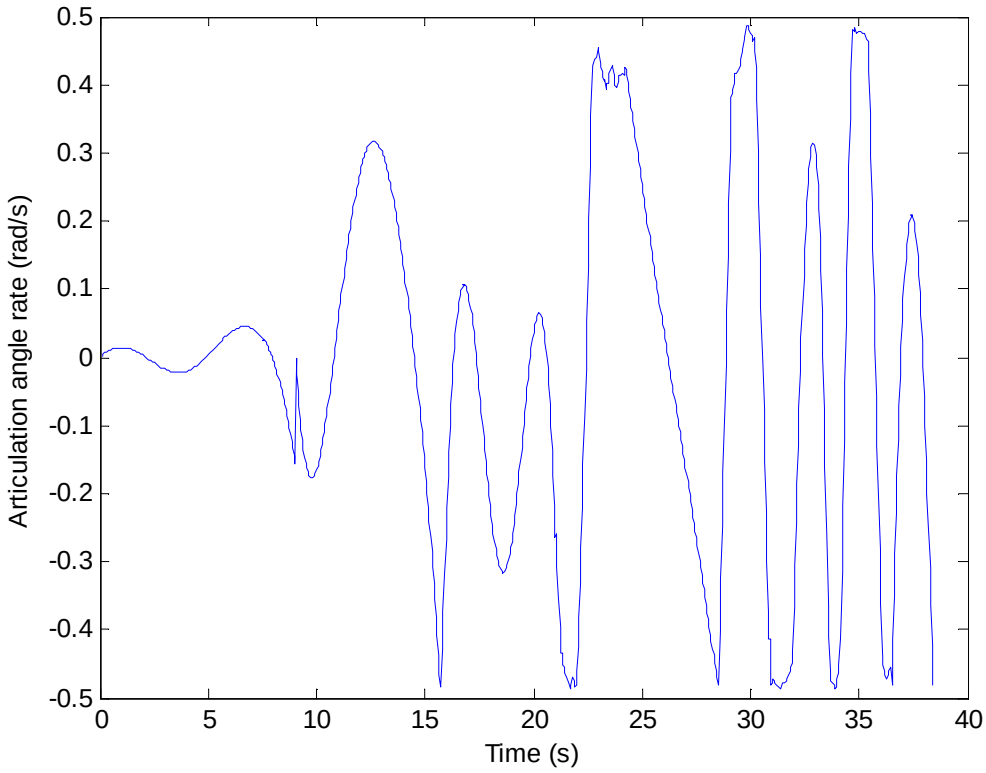

Figure 76. The simulated rate of articulation angle change.

The vehicle's acceleration was defined according to the 'bang-bang' control principle. Maximum acceleration (0.85 m/s^2) is employed to reach the maximum velocity of 3 m/s, as can be seen in Figure 77.

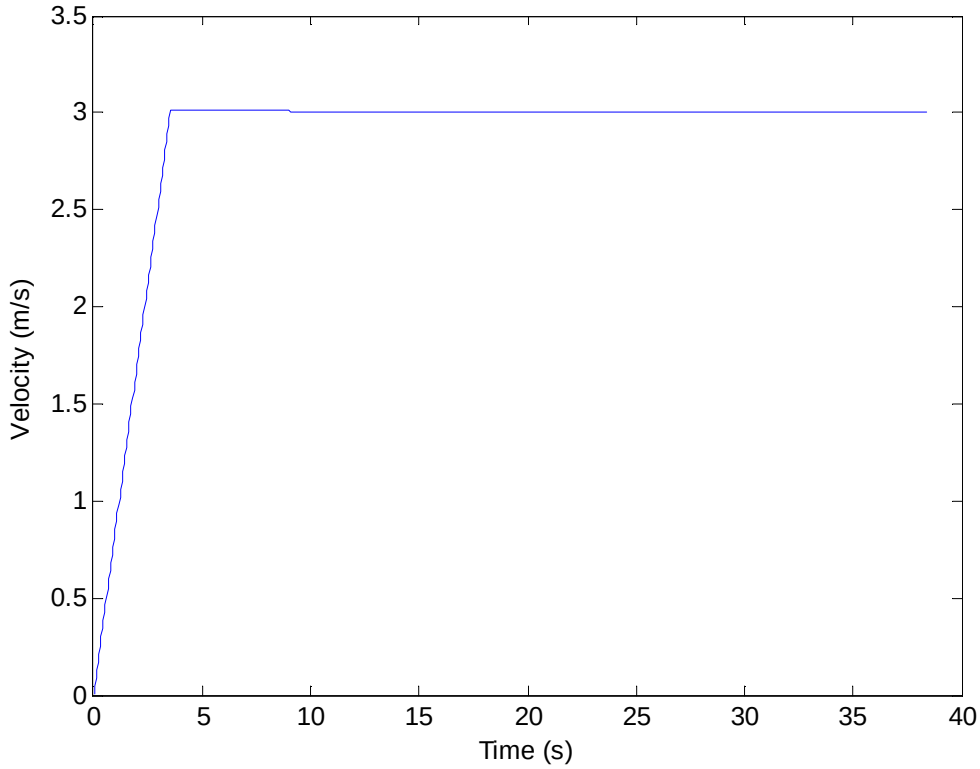

Figure 77. The simulated velocity.

6.2.2 Path tracking

As has been mentioned in Chapter 3, various methods have been attempted to implement an articulated vehicle path tracking controller. Disagreement exists on the form of which such a controller should take: [75] notes that the centre of the articulation joint should be tracked while [11] indicates that slip should explicitly be accounted for. [76] believes that tracking the front unit of the vehicle is sufficient and that accounting for slip is superfluous. A similar view is supported by [1]. As has been mentioned in Chapter 4, a controller which can effectively handle the unmodelled dynamics of the vehicle is required.

In this section, a path tracking controller based on the one given by [1] will be presented and simulated using the data obtained from field trials.

6.2.2.1 Path tracking controller

In order to compute or predict the vehicle's current pose, the discrete-time variation of the kinematic model given by equations (6.7) to (6.9) is required and is shown here:

$$s_{t+1} = s_t + h\begin{bmatrix} \cos\theta_t & 0 \\ \sin\theta_t & 0 \\ \dfrac{-\sin\gamma_t}{l_F\cos\gamma_t + l_R} & \dfrac{-l_R}{l_F\cos\gamma_t + l_R} \end{bmatrix}\begin{bmatrix} v_t \\ \omega_t \end{bmatrix}, \tag{6.30}$$

where t refers to the time. The parameters of the Bell L1706E wheeled loader were used (given in section 5.3, Table 10), where the length of the front unit, l_1, was given as 1.5 m and the length of the rear unit, l_2, 1.9 m. The predicted pose of the vehicle is denoted by $\bar{s}_t = (x_t, y_t, \theta_t)$ and the speed is represented by v_t and the steering rate by ω_t. The sample time is denoted by h.

Through practical experiments, [1] found that the lateral and heading error between the current and the desired pose contains sufficient information to lead the vehicle's front unit to the desired pose. With reference to Figure 78, the errors are defined as follows:

$$\varepsilon_L = -(x_t - x_d)\sin\theta_d + (y_t - y_d)\cos\theta_d, \tag{6.31}$$

$$\varepsilon_H = \theta_t - \theta_d, \tag{6.32}$$

where ε_L is the lateral error and ε_H represents the heading error. Now, a path-tracking controller needs to be designed to drive both errors to zero.

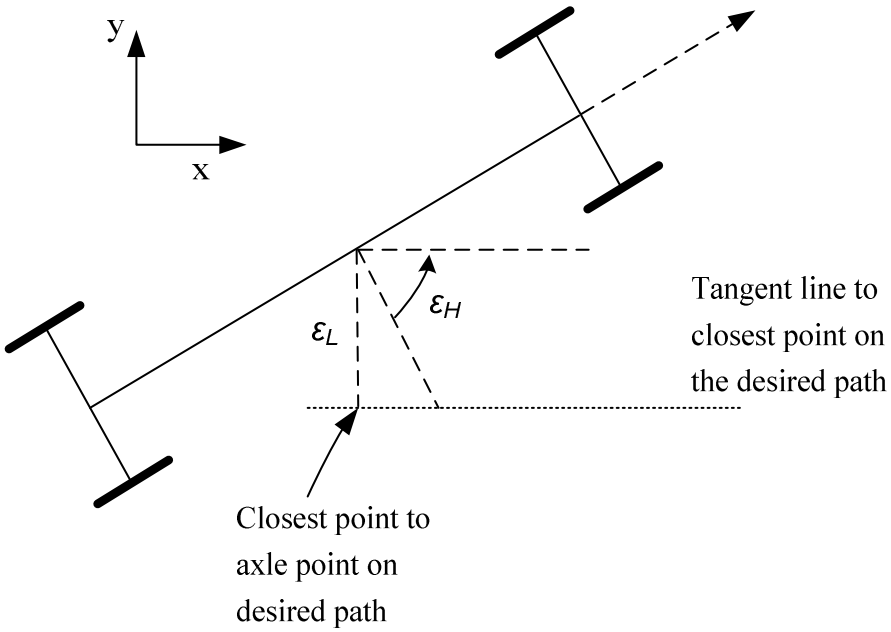

Figure 78. Definition of the lateral and heading error.

The path-tracking control system depicted in Figure 79 was used to regulate the vehicle's pose.

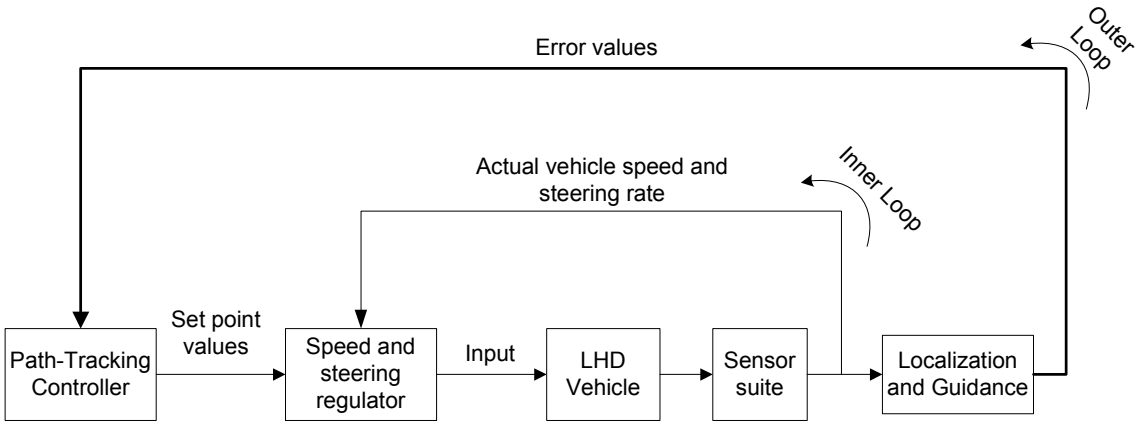

Figure 79. Path-tracking control system, derived from [1].

With reference to Figure 79, the controller consists of two types of feedback loops: an outer loop and an inner loop. The underlying justification for this two-timescale control system design is founded on the basic assumption that one can specify sufficient bandwidth separation between the inner and outer control loops. Hence, outer-loop

controllers/estimators are based on vehicle kinematics with the requirement that the inner-loop dynamic regulators can efficiently track reference signals provided by the outer loop at their delivery bandwidth. This bandwidth separation effectively handles the unmodelled steering dynamics. The focus of this chapter is on the outer loop.

6.2.2.1.1 Outer loop

The outer loop returns the error values of the vehicle's speed, lateral position and heading, defined by the expressions given in equations (6.31) and (6.32). The path tracking controller then attempts to drive the errors to zero. This is achieved by defining the approximate error dynamics as follows:

$$\dot{\varepsilon}_L = v \sin \varepsilon_H, \tag{6.33}$$

$$\dot{\varepsilon}_H = \frac{-v \sin \gamma - l_R \omega}{l_R + l_F \cos \gamma}, \tag{6.34}$$

where time-dependency has been left out, for simplicity. In order to apply linear regulator theory, a simple variable transformation is made $z_1 := \varepsilon_L$ and $z_2 := v \sin \varepsilon_H$ which results in the following second order system:

$$\dot{\bar{z}} = \begin{bmatrix} 0 & 1 \\ 0 & 0 \end{bmatrix} \bar{z} + \begin{bmatrix} 0 \\ 1 \end{bmatrix} \eta, \tag{6.35}$$

where $\bar{z} = (z_1, z_2)$ and η is the new input variable. The system is stabilizable by linear state feedback. The feedback controller is defined by

$$\eta = -k_1 z_1 - k_2 z_2 \tag{6.36}$$

and the closed loop system therefore becomes

$$\dot{\bar{z}} = \begin{bmatrix} 0 & 1 \\ -k_1 & -k_2 \end{bmatrix} \bar{z}\,. \tag{6.37}$$

Choosing the appropriate feedback gains, k_1 and k_2, depends on the required frequency response of the system. The bandwidth limitation is dependent on the vehicle and actuator dynamics which are controlled by the inner loop.

6.2.2.2 Simulation

For the purpose of simulating the path-tracking efficiency, it was assumed that the inner loop regulated the required steering rate and the vehicle speed accurately. The frequency bandwidth of the outer loop should be around a fifth of the inner loop [1], resulting in a required bandwidth of ± 0.5 rad/s. The values of k_1 and k_2 were chosen as 1 and 1.7321 respectively.

In order to illustrate the path tracking efficiency, the controller was set to track a constant circle. Initial errors of $\varepsilon_L = 1$ m and $\varepsilon_H = 0.17$ radians where arbitrarily, yet realistically, chosen. Figure 80 shows the trajectories of the state $z_1 = \varepsilon_L$, the state z_2, and the resulting heading error, ε_H. After about 7 seconds, the error regulator achieves the zero steady-state value.

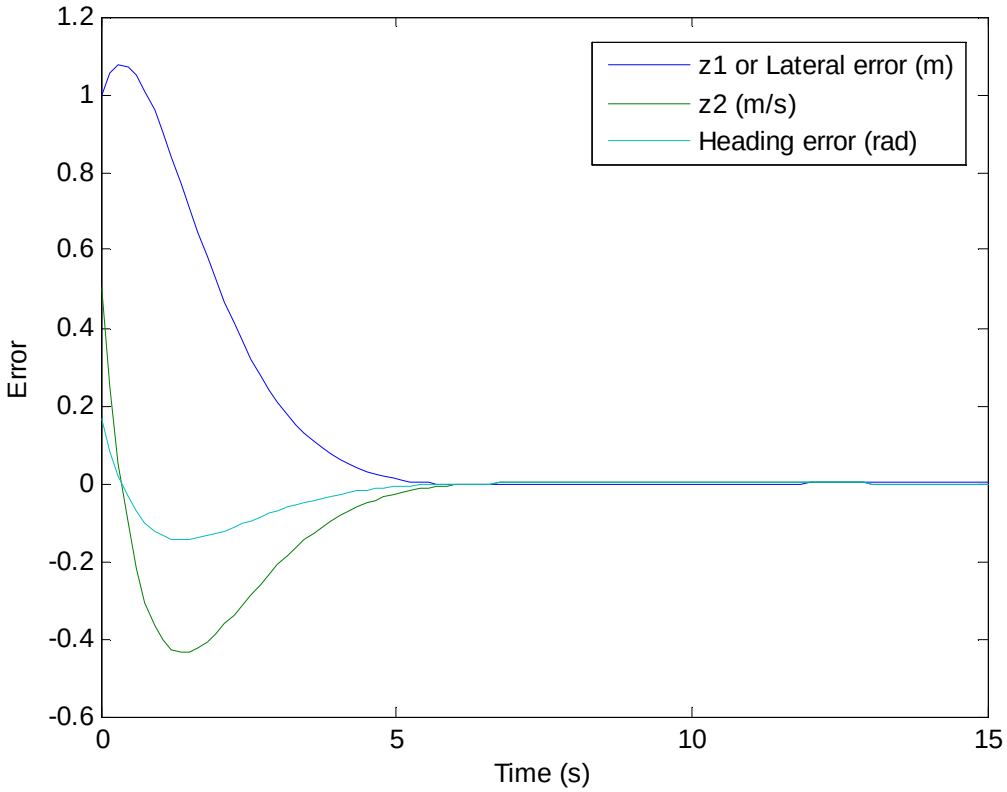

Figure 80. The state and the error trajectories.

Similar to Figure 80, Figure 81 shows the state and error trajectories and includes the required input trajectory, η, which is defined by equation (6.36).

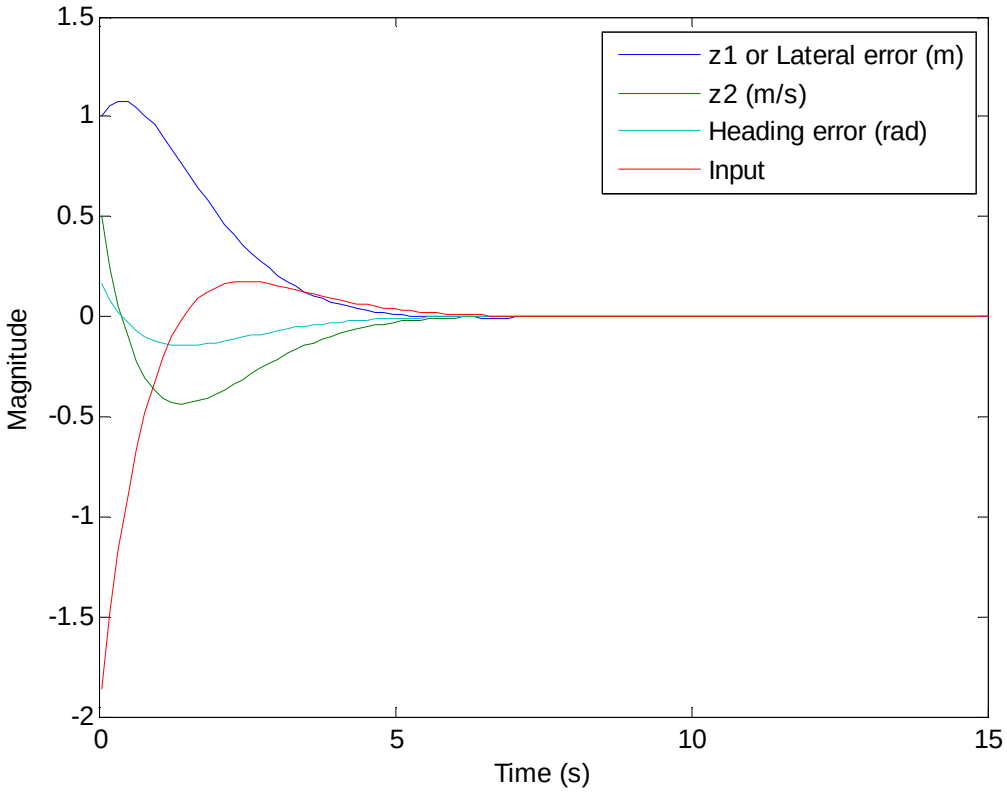

Figure 81. The state, error and input trajectories.

Figure 82 shows the tracking performance of the controller. The solid blue line represents the required path while the red, dashed line shows the path of the vehicle with an initial error of $\varepsilon_L = 1$ m and $\varepsilon_H = 0.17$ radians. The error is eliminated after about 7 s after which the red dashed line joins the trajectory of the required blue path.

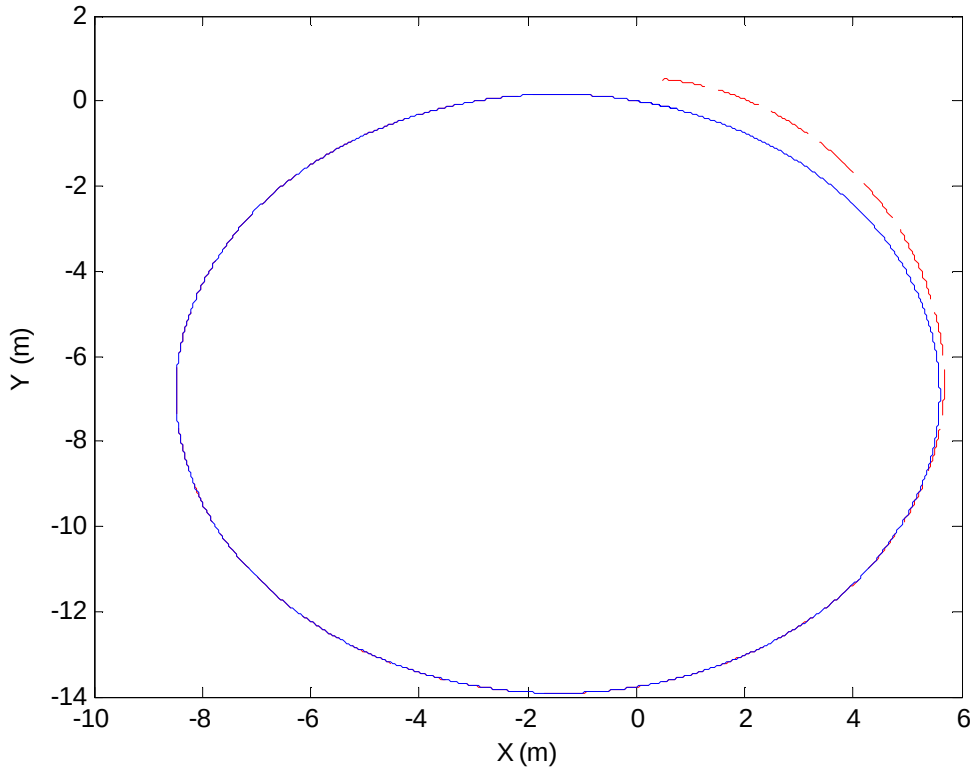

Figure 82. The tracking performance of the controller.

In order to illustrate the performance of the controller in a real-world application, the track-layout, also given in Figure 64, was tracked. Since no laser range data was available, the path points were defined by odometry and GPS data which were obtained by manually driving the vehicle along the desired path. The desired heading of the vehicle was derived from integrating the yaw data from the gyrometer which was placed on the front unit of the vehicle. Then the path was constructed with a path-point resolution of 0.5 m. The path-tracking controller continuously calculated the errors using equations (6.31) and (6.32). Initial errors were both defined as zero. Since the performance of the outer loop is of most importance, the inner loop regulators, i.e. tracking of the steering rate and speed of the vehicle, were assumed to be working accurately.

Figure 83 shows the tracking result.

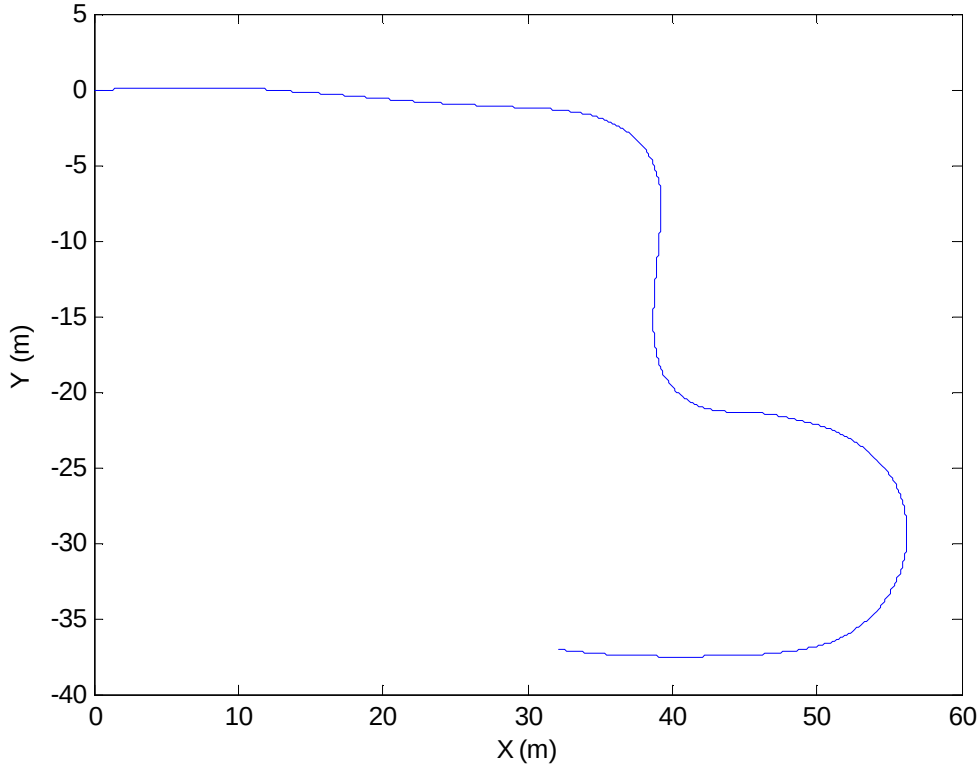

Figure 83. The trajectory of the path-tracker with path points from the real circuit.

6.3 DISCUSSION

As has been stated in the introduction to this chapter, the control and underground localisation of a mining vehicle is a notable challenge. Two methods, nonlinear optimal control and linear path-tracking control have been presented. The latter was based on the regulator system by [1]. The path-tracking solution is a very accurate and robust control solution but has the downside of requiring an a priori 'teaching' session to gather data in order to construct the path layout. This can be time-consuming and requires the mine to halt its operations until such a path-learning session has been completed.

The nonlinear optimal control solution does not require path learning but does not follow the desired path as effectively as the path-tracking controller. The purpose of the optimal control simulation was to show that this method is a possible solution to the navigation problem. However, the method requires a number of optimization steps in order to become practically viable. Adding more nodes on the map in order to reduce the distance for which

the optimal control vector has to be found will improve the convergence. Furthermore, the predicted trajectory often lies undesirably close to the walls, suggesting that an additional feature is required to ensure that a safe distance to the walls is always maintained. Information from the laser range finder could be used for this purpose by including the offset to the required distance to the walls or other obstacles in the optimal control cost function.

Both techniques offer the vehicle enough look-ahead to guide the vehicle at optimal speeds. Furthermore, both methods do not require any extra infrastructure.

6.4 CHAPTER SUMMARY

First of all, the opportunistic localization method was presented. The method was then adapted to the underground environment problem and a feature was designed to include look-ahead. Then, two control schemes, both relying partly on opportunistic localization, were presented, simulated and evaluated. The first was a nonlinear control method, based on optimal control theory. The second was a path-tracking, error minimization solution to the control problem. The performances of the control algorithms were discussed and conclusions were drawn.

CHAPTER 7

CONCLUSION

7.1 SUMMARY

The automation of the tramming or load, haul and dump procedure, performed by an LHD vehicle, holds the potential to improve productivity, efficiency and safety. Productivity is mainly increased by longer working hours; the efficiency is improved by repetitive, faultless and predictable work; and safety is improved by removing the human operator from the harsh environment. However, before the automation of the process can be addressed, a thorough understanding of the process and its duty in the overall mining method is required. Therefore, the current applicable mining methods and their areas of potential automation were given. Since the automation of the LHD vehicle is at the core of this project, its implementation in the tramming process was also justified. Also, the current underground navigation methods were given and their shortcomings were named. It was concluded that infrastructure-free navigation is the only viable solution in the ever-changing mining environment. With that in mind, the feasibility of various navigation sensors was discussed and conclusions were drawn.

Both kinematic and dynamic modelling of LHD vehicles was introduced. Various forms of kinematic models were given and their underlying modelling assumptions were named. The most prominent assumptions concern the vehicle's half-length and the inclusion of a wheel-slip factor. The dynamic modelling techniques, with a strong emphasis on tyre modelling, were also stated. In order to evaluate the modelling techniques, practical field tests were performed on articulated vehicles. The test on the commonly used Wright 365 LHD gave a good impression on the harsh ergonomics under which the operator has to work. A more thorough test was performed on a Bell 1706C articulated loader. The kinematic properties of the loader are very similar to that of the LHD. The test results were then compared to simulation results obtained from the kinematic models. Also, the above-named assumptions were tested, evaluated and discussed. A dynamic model was also simulated and discussed. Lastly, two localization and control methods were given and evaluated. The first method was an open-loop nonlinear optimal control strategy with periodic position resetting while the second method was a path-tracking controller.

7.2 DISCUSSION AND CONCLUSION

One of the main aims of this study was to investigate the current LHD modelling techniques and to evaluate their performances. When compared to the practical test data, it was found that the general kinematic model underestimates the turning behaviour of the vehicle. A few reasons may contribute to this error:

- Sensor drift and calibration errors of the rope displacement sensor and gyrometer.
- The kinematic model suffers under the assumptions that the dynamic forces may be ignored. Influential dynamics include the steering dynamics and the tyre slip angles.

The sensors were thoroughly tested and calibrated, minimizing the effect of calibration errors. Therefore, it was concluded that the unmodelled dynamics of the vehicle, especially the effect of the side slip angles have a notable effect on the vehicle's handling. The inclusion of a piecewise linear tyre model into the kinematic framework improved the overall model performance, especially during steady-state turning. However, when the turning angle was varied, the slip-inclusive model was not as accurate, mainly because of the nonlinear lateral forces acting on the tyres during such manoeuvres. A more adaptive, non-linear tyre model might improve the prediction of the slip angles. Overall, the conclusion may be drawn that the inclusion of a tyre model does improve the accuracy of the kinematic LHD model.

The rather trivial dilemma of assuming that the LHD is articulated at its half-length was also solved. Simulations revealed that if the lengths of the front and rear units differ, the off-tracking error needs to be accounted for. Distinctively including the unit lengths in the kinematic model does not complicate the model to a significant extent and should therefore be implemented.

Although a few dynamic LHD vehicle models have been developed, its role in the navigation of such a vehicle was not clear, since the model's computational complexity warrants it unwanted in navigation schemes. The purpose of the dynamic model, according

to [15], might therefore be similar to that of a Kalman filter. It would then be used to update and improve the estimate of the vehicle's position between samples of an external sensor in a navigation system. The relatively slow speeds at which the LHD travels in the underground environment has convinced most researchers to ignore the dynamics of the vehicle and account for its parasitic effects by designing robust control systems. This approach is also supported by this study.

Therefore, in this study, the development of the localization and control of the LHD was based on the kinematic model. Of the two methods given, the path tracking solution is currently the preferred solution. However, no field trials were performed and conclusion can only be drawn from the given simulation results. Importantly, the general requirements of a robust controller were also given. Both methods were based on the infrastructure-free navigation principle can be implemented with readily available sensor suits.

7.3 FUTURE WORK

In order to improve the accuracy of the kinematic LHD vehicle models, certain influential dynamics need to be included. This was attempted by including a piece-wise linear tyre model. However, the model's accuracy may further be improved by the inclusion of a more precise nonlinear tyre model. Also, a usable and validated dynamic model still has to be developed.

This study has laid a good platform for future LHD navigation development. The navigation schemes presented in chapter 6 show good promise but should be practically validated. The navigation schemes could further be enhanced by including obstacle avoidance and a collision detection algorithm. To incorporate the necessary human factor in the automation of these vehicles, especially human judgment and sentiment, an option to switch to manual tele-operation the automated LHD is recommended.

Also, future work may include the automation of the loading and dumping procedures.

REFERENCES

[1] J. Marshall, T. Barfoot, and J. Larsson, "Autonomous Underground Tramming for Center-Articulated Vehicles," *Journal of Field Robotics,* vol. 25, no. 6, pp. 400-421, March 2008.

[2] H. Mäkelä, "Overview of LHD navigation without artificial beacons," *Robotics and Autonomous Systems,* vol. 36, no. 1, pp. 21-35, July 2001.

[3] G. Brophey and D. Euler, "The Opti-Trak System, a system for automating today's LHDs and trucks," *CIM Bulletin,* vol. 87, no. 984, pp. 52-57, 1994.

[4] A. Grenier, G. Chevrette, and C. Coache, "Noranda automativ guidance system architecture overview," in *Proc. Canadian Symp. on Mine Automation*, 1994, pp. 116-119.

[5] G. Eriksson and A. Kitok, "Automatic loading and dumping using vehicle guidance in a Swedish mine," in *Proc. Int. Symp. on Mine Mechanisation and Automation*, 1991, pp. 1533-1540.

[6] E. S. Duff, J. M. Roberts, and P. I. Corke, "Automation of an underground mining vehicle using reactive navigation and opportunistic localization," in *Proc. Int. Conf. on Intelligent Robots and Systems*, 2003, pp. 3775-3780.

[7] A. Hemami and V. Polotski, "Path tracking control problem formulation of an LHD loader," *Int. Journal of Robotics Research,* vol. 17, no. 3, pp. 193-199, February 1998.

[8] J. Steele, C. Ganesh, and A. Kleve, "Control and scale model simulation of sensor-guided LHD mining machines," *IEEE Trans. on Industry Applications* vol. 29, no. 6, pp. 1232-1238, November 1993.

[9] P. I. Corke and J. M. Roberts, "Evaluation of a suite of navigation sensors for use on autonomous haul trucks and LHDs at Mount Isa mine," University of Sydney and Mount Isa Mines, August 1996.

[10] S. J. Julier and H. F. Durrant-Whyte, "On The Role of Process Models in Autonomous Land Vehicle Navigation Systems," *IEEE Trans. on Robotics and Automation*, vol. 19, no. 1, pp. 1-14, February 2003.

[11] S. Scheding, G. Dissanayake, E. Nebot, and H. Durrant-Whyte, "Slip Modeling and Aided Inertial Navigation of an LHD," in *Proc. Int. Conf. on Robotics and Automation*, Albuquerque, New Mexico, 1997, pp. 1904-1909.

[12] H. Ishimoto, T. T. Sarata, S. Sarata, and S. Yuta, "A practical trajectory following of an articulated steering type vehicle," in *Int. Conf. on Field and Service Robotics* Canberra, Australia, 1997, pp. 412-419.

[13] J. M. Roberts, E. S. Duff, P. I. Corke, P. Sikka, G. J. Winstanley, and J. Cunningham., "Autonomous control of underground mining vehicles using reactive navigation," in *Proc. Int. Conf. on Robotics and Automation*, San Francisco, USA, 2000, pp. 3790-3795.

[14] Y. Yavin, "Modelling the Motion of an Underground Mining Vehicle," *Mathematical and Computer Modelling*, vol. 42, no .1, pp. 1123-1130, 2005.

[15] B. Dragt, F. Camisani-Calzolari, and I. Craig, "Modelling the dynamics of a load-haul-dump vehicle," in *Proc. 16th IFAC World Congress*, Prague, Czech Republic, 2005.

[16] N. L. Azad, A. Khajepour, and J. Mcphee, "Robust state feedback stabilization of articulated steer vehicles," *Vehicle System Dynamics*, vol. 45, no. 3, pp. 249-275, 2007.

[17] C. Altafini, "A Path-Tracking Criterion for an LHD Articulated Vehicle," *Int. Journal on Robotics Research*, vol. 18, no. 5, pp. 435-441, 1999.

[18] W. A. Hustrulid and R. C. Bullock, *Underground mining methods: engineering fundamentals and international case studies*: Society for Mining, Metallurgy, and Exploration, 2001.

[19] B. J. Dragt, "Modelling and Control of an Underground Mine Vehicle," Master's thesis, University of Pretoria, 2006.

[20] Barloworld and Wright, "Wright HD356 B-series," in *LHD8283W01*: Barloworld, 2000.

[21] C. Altafini, "Why to use an Articulated Vehicle in Underground Mining Operations?" in *IEEE Int. Conf. on Robotics & Automation*, Detroit, Michigan, 1999, pp. 3020-3025.

[22] H. H. Mohle, "Factors Affecting LHD Productivity on Premier Diamond Mine," August 1995.

[23] P. Saayman, I. K. Craig, and F. R. Camisani-Calzolari, "Optimization of an Autonomous Vehicle Dispatch System in an Undergound Mine," *Journal of The South African Institute of Mining and Metallurgy*, vol. 106, pp. 77-106, February 2006.

[24] "Annual Report," Mine Health and Safety Council, 2007.

[25] A. Seccombe, "SA mine safety under fire," 2007, http://www.miningmx.com/gmbk2007/676219.htm. Last accessed on 3 August 2009.

[26] D. I. McBride, "Noise-induced hearing loss and hearing conservation in mining," *Occupational Medicine,* vol. 54, pp. 290-296, February 2004.

[27] M. K. Habib and S. Yuta, "Map Representation and Path Planning for Mobile Robots in a Building Environment," *IEEE Int. Conf. on Robotics and Automation,* pp. 173-178, Oct. 1988 1988.

[28] B. Kuipers and Y. T. Bruyn, "A Robot Exploration and MApping Strategy Based on a Semantic Hierarchy of Spacial Representations," *Robotics and Autonomous Systems,* vol. 8, pp. 47-63, 1991.

[29] M. K. Habib and S. Yuta, "Map Representation for Large In-door Environment, Path Planning and Navigation Techniques for an Autonomous mobile robot with its Implementation," *Int. J. of Automation in Construction,* vol. 1, pp. 155-179, 1993.

[30] A. Piche and P. Gaultire, "Mining automation technology - The first frontier," *CIM Bulletin,* vol. 89, pp. 51-54, 1993.

[31] N. Vagenas, M. Scoble, and G. Baiden, "A review of the first 25 years of mobile machine automation in underground hard rock mines " *CIM Bulletin,* vol. 90, no. 1006, pp. 57-62, 1997.

[32] U. Wiklund, U. Andersson, and K. Hyyppä, "AGV navigation by angle measurements," in *Proc. 6th Int. Conf. on Automated Guided Vehicle Systems,* 1988.

[33] O. Khatib, "Real-Time Obstacle Avoidance for Manipulators and Mobile Robots " *Int. Journal of Robotics Research,* vol. 5, no. 1, pp. 90-98, 1986.

[34] J. R. Asensio, J. M. M. Montiel, and L. Montano, "Goal directed reactive robot navigation with relocation using laserand vision," in *Proc. Int. Conf. on Robotics and Automation,* 1999, pp. 2905-2910.

[35] S. Scheding, E. Nebot, and D. Pagac, "Reactive Navigation and Local Deliberative Planning for Autonomous Mobile Vehicles," in *Proc. Nat. Conf. of the Australian Robotics Association,* Melbourne, Australia, 1995, pp. 264-271.

[36] D. A. Pomerleau, *Neural Network Perception for Mobile Robot Guidance*: Kluwer Academic Publisher, 1993.

[37] A. Dubrawski and J. L. Crowley, "Self-supervised neural system for reactive navigation," in *Proc. Int. Conf. on Robotics and Automation*, 1994, pp. 2076-2081.

[38] R. Smith and P. Cheesman, "On the representation of spatial uncertainty," *Int. Journal on Robotics Research*, vol. 5, no. 4, pp. 56-68, 1987.

[39] R. Smith, M. Self, and P. Cheeseman, "Estimating uncertainspatial relationships in robotics," *Autonomous Robot Vehicles*, vol. 6, pp. 167-193, Jan. 1990.

[40] J. J. Leonard and H. F. Durrant-Whyte, "Simultaneous map building and localisation for an autonomous mobile robot," in *Proc. IEEE Int. Workshop on Intelligent Robots and Systems*, 1991, pp. 1442-1447.

[41] J.-S. Gutmann and K. Konolige, "Incremental mapping of large cyclic environment," in *Proc. IEEE. Int. Symp. Computational Intelligence in Robotics and Automation*, 1999, pp. 318-325.

[42] M. Bosse, P. Newman, J. Leonard, M. Soika, W. Feiten, and S. Teller, "An Atlas framework for scalable mapping," in *Proc. IEEE Int. Conf. Robotics and Automation*, 2003, pp. 1899-1906.

[43] S. Thrun, W. Burgard, and D. Fox, "A real-time algorithm for mobile robot mapping with applications to multi-robot and 3D mapping," in *Proc. IEEE Int. Conf. on Robotics and Automation*, 2000, pp. 321-328.

[44] A. Doucet, N. d. Freitas, and N. Gordon, *Sequential Monte Carlo Methods in Practice*: Springer, 2001.

[45] M. Montemerlo, S. Thrun, D. Koller, and B.Wegbreit, "FastSLAM 2.0: An improved particle filtering algorithm for simultaneous localization and mapping that provably converges," in *Proc. of the Sixteenth International Joint Conference on Artificial Intelligence*, 2003, pp. 1283-1286.

[46] J. E. Guivant and E. M. Nebot, "Optimization of the simultaneous localization and map building algorithm for real time implementation," *IEEE Trans. on Robotic and Automation*, vol. 17, no. 2, pp. 242-257, September 2000.

[47] K. Murphy, "Bayesian map learning in dynamic environments," *Advances in Neural Information Processing Systems*, vol. 5, January 1999.

[48] R. Madhavan, G. Dissanayake, and H. Durrant-Whyte, "Map-building and map based localization in an underground-mine by statistical pattern matching," in *Proc. Int. Conf. on Pattern Recognition*, 1998, pp. 1744-1746.

[49] R. Madhavan, G. Dissanayake, and H. Durrant-Whyte, "Autonomous underground navigation of an LHD using a combined ICP-EKF approach," *Robotics and Automation*, vol. 4, no. 2, pp. 3703-3708, August 1998.

[50] D. Hahnel, W. Burgard, D. Fox, and S. Thrun, "An efficient fastSLAM algorithm for generating maps of large-scale cyclic environments from raw laser range measurements," in *Proc. IEEE Int. Conf. on Intelligent Robots and Systems*, 2003, pp. 206-211.

[51] L. Montesano, J. Minguez, and L. Montano, "Probabilistic scan matching for motion estimation in unstructured environments," in *Int. Conf. on Intelligent Robots and Systems*, 2005, pp. 3499-3504.

[52] S. Thrun, S. Thayer, W. Whittaker, C. Baker, W. Burgard, D. Fergusen, D. Hahnel, D. Montemerlo, A. Morris, Z. Omohundro, and C. Reverte, "Autonomous exploration and mapping of abandoned mines," *Robotics and Automation*, vol. 11, no. 11, pp. 79-91, December 2004.

[53] "Sandvik, AutoMine," 2008, http://www.sandvik.com/sandvik/9885/Internet/AU09003.nsf/GenerateTopFrameset?ReadForm&menu=&view=http%3A//www.sandvik.com/sandvik/9885/Internet/AU09005.NSF/NAUnique/E0C0340BF0A36274CA25768700005908%3FOpenDocument&banner=/sandvik/9885/Internet/AU09003.nsf/LookupAdm/BannerForm%3FOpenDocument. Last accessed on 2 Oktober 2011.

[54] "Caterpillar, MINEGEM," 2009, http://www.cat.com/cda/files/1873203/7/243PR09%20MINEGEM,%20Press%20Release.doc?m=167201&x=7. Last accessed on 2 Oktober 2011.

[55] "Atlas Copco, Sooptram automation," 2009, http://pol.atlascopco.com/SGSite/SGAdminImages/PrintedMatters/5585.pdf. Last accessed on 2 Oktober 2011.

[56] S. Scheding, G. Dissanayake, E. M. Nebot, and H. Durrant-Whyte, "An Experiment in Autonomous Navigation of an Underground Mining Vehicle," *IEEE Trans. on Robotics and Automation*, vol. 15, no. 1, pp. 85-95, February 1999.

[57] L. Alvarez and J. Yi, "Adaptive emergency braking control in automated highway systems," in *Proc. IEEE Conf. Decision and Control*, Phoenix, USA, 1999, pp. 3740-3745.

[58] P. Ridley and P. Corke, "Load haul dump vehicle kinematics and control," *Journal of Dynamic Systems, Measurement, and Control*, vol. 125, no. 1, pp. 54-59, 2003.

[59] J. Harned, L. Johnston, and G. Scharpf, "Measurement of tire brake force characteristics as related to wheel slip (anti-block) control system design," *SAE Trans.*, vol. 78, pp. 909-925, 1969.

[60] H. B. Pacejka and R. S. Sharp, "Shear force development by pneumatic tires in steady state conditions: A review of modeling aspects," *Vehicle System Dynamics*, vol. 20, no. 3, pp. 121-176, January 1991.

[61] P. W. A. Zegelaar and H. B. Pacejka, "The in-plane dynamics of tyres on uneven roads," *Vehicle System Dynamics*, vol. 25, pp. 714-730, Jan. 1996.

[62] E. Denti and D. Fanteria, "Models of wheel contact dynamics: An analytical study on the in-plane transient response of a brush model," *Vehicle System Dynamics*, vol. 34, pp. 199-225, Sep. 2000.

[63] F. Borelli, A. Bemporad, M. Fodor, and D. Hrovat, "A Hybrid Approach to Traction Control," *Lecture Notes in Computer Science*, vol. 2034, pp. 162-174, 2001.

[64] L. Li, F. Wang, and Q. Zhou, "Integrated Longitudinal and Lateral Tire/Road Friction Modeling and Monitoring for Vehicle Motion Control," *IEEE Trans. on Intelligent Transportation Systems*, vol. 7, no 1., March 2006.

[65] P. Falcone, M. Tufo, F. Borelli, J. Asgari, and H. E. Tseng, "A linear time varying model predictive control approach to the integrated vehicle dynamics control problem in autonomous systems," in *46th IEEE Conf. on Decision and Control* New Orleans, LA, 2007, pp. 2980 - 2985.

[66] M. Burckhardt, *Fahrwerktechnik: Radschlupfregelsysteme*. Würzburg, Germany: Vogel-Verlag, 1993.

[67] G. Rill, *Simulation von Kraftfahrzeugen*. Wiesbaden, Germany: Vieweg, 1994.

[68] H. B. Pacejka, *Tyre and Vehicle Dynamics*, 2nd ed. Oxford: Elsevier, 2006.

[69] P. Dahl, "A solid friction model," The Aerospace Corp., El Segundo,1976.

[70] L. Li, F.-Y. Wang, and G. Shan, "Design of tire fault observer based on estimation of tire/road friction conditions," *Automatica Sinica*, vol. 28, no. 5, pp. 689-694, October 2003.

[71] C. Chen and M. Tomizuka, "Modeling and Control of Articulated Vehicles," University of California, Berkeley, PATH Research Report, November 1997.

[72] R. M. DeSantis, "Modeling and Path-Tracking for a Load-Haul-Dump Mining Vehicle," *Journal of Dynamic Systems, Measurement and Control*, vol. 119, pp. 40-48, 1997.

[73] "Bell Equipment UK," 2010, http://www.bellequipment.co.uk/produkts/fel-L1706E.php. Last accessed on 10 November 2010.

[74] D. E. Kirk, *Optimal Control Theory*. New York: Dover Publications, 2004.

[75] V. Polotski, "New Reference Point for Guiding an Articulated Vehicle," in *Int. Conf. on Control Applications*, Anchorage, Alaska, USA, 2000, pp. 455-460.

[76] P. Ridley and P. Corke, "Autonomous Control of an Underground Mining Vehicle," in *Australian Conf. on Robotics and Automation*, Sidney, Australia, 2001, pp. 26-31.